

UNIVERSITÉ DE NANTES
FACULTÉ DES SCIENCES ET TECHNIQUES

ÉCOLE DOCTORALE
Matériaux Matière Molécule en Pays de Loire

Année : 2010

N° attribué par la bibliothèque

--	--	--	--	--	--	--	--	--	--

Développement d'approches hydrodynamique et hydrocinétique aux collisions noyau-noyau ultra-relativistes

THÈSE DE DOCTORAT

Discipline : Physique Nucléaire
Spécialité : Physique des Ions Lourds

Présentée et soutenue publiquement par

Iurii KARPENKO

Le 25 mai 2010, devant le jury ci-dessous

<i>Président</i>	M. Smilga A.,	<i>Pr. Université, Subatech, Nantes</i>
<i>Rapporteurs</i>	M. Lednicky R.,	<i>Directeur de recherche, Joint Institute for Nuclear Research, Dubna</i>
	M. Ollitrault J.-Y.,	<i>Directeur de recherche CNRS, CEA Saclay, Gif-Sur-Yvette</i>
<i>Examineurs</i>	M. Sinyukov Yu.,	<i>Directeur de recherche, Bogolyubov Institute for Theoretical Physics, Kiev</i>
	M. Werner K.,	<i>Pr. Université, Subatech, Nantes</i>

Co-directeurs de thèse : M. Sinyukov Yu., *Directeur de recherche,
Bogolyubov Institute for Theoretical Physics, Kiev*
M. Werner K., *Pr. Université, Subatech, Nantes*

N° ED _____



UNIVERSITÉ DE NANTES

**Development of hydrodynamic and
hydrokinetic approaches to
ultrarelativistic nucleus-nucleus
collisions**

PhD thesis

Iurii KARPENKO

SUBATECH (Nantes, France) and

BITP (Kiev, Ukraine), 2010

CONTENTS

1	Literature review	1
1.1	Introduction	1
1.2	Particle distributions	2
1.3	Correlation functions	4
1.4	Evolution picture	6
1.5	Dynamic models	7
1.6	Outline of the thesis	9
2	Hydrodynamic solutions	11
2.1	Introduction	11
2.2	General analysis	12
2.3	Gradient-like velocity ansatz	13
2.4	Relativistic ellipsoidal solutions	14
2.5	Generalization of the Hubble-like flows	17
2.6	Conclusions	20
3	Fast MC freeze-out generator	21
3.1	Introduction	21
3.2	Hadron multiplicities	22
3.3	Hadron momentum distributions	25
3.4	Generalization of the Cooper-Frye prescription	26
3.5	Freeze-out surface parameterizations	27
3.6	Hadron generation procedure	30
3.7	Validation of the MC procedure	32
3.8	Input parameters and results	33
3.9	Freeze-out for non-central collisions	43
3.10	Different chemical and thermal freeze-outs	48
3.11	Results for non-central collisions	49
3.12	Conclusions	62

4	Hybrid model	63
4.1	Introduction	63
4.2	Initial state model : EPOS	66
4.3	Hydrodynamic evolution, realistic equation-of-state	70
4.3.1	Hydrodynamic algorithm	73
4.3.2	Resonance gas	76
4.3.3	Ideal QGP	77
4.4	Freeze-out	78
4.5	UrQMD afterburner	80
4.6	Results: Elliptical flow	81
4.7	Transverse momentum spectra and yields	84
4.8	Femtoscopia	87
4.9	Summary and conclusions	92
5	Hydro-kinetic model	93
5.1	Introduction	93
5.2	General formalism	95
5.3	Cooper-Frye prescription	98
5.4	Initial conditions for hydro-evolution	105
5.4.1	Pre-thermal flows	105
5.4.2	Glauber-like initial transverse profile	106
5.4.3	Initial conditions motivated by Color Glass Condensate model	107
5.5	Equation of state	110
5.5.1	The EoS in the equilibrated space-time domain.	111
5.5.2	The EoS in the chemically non-equilibrated domain.	111
5.6	Kinetics in the non-equilibrium hadronic zone	114
5.6.1	Emission functions in hyperbolic coordinates and spectra formation	114
5.6.2	Resonance decays in multi-component gas	117
5.6.3	Collision rates	118
5.7	Hydrodynamics	120
5.8	Results: femtoscopy at RHIC	121
5.9	Space-time scales for SPS, RHIC, LHC	126
5.10	Conclusions	129
6	Conclusions	133
	Glossary	136
	Bibliography	136

LIST OF FIGURES

3.1	The validation of the MC procedure: the transverse momentum spectra and the corresponding MC results. Also shown are the MC results obtained with a constant residual weight.	33
3.2	The π^+ emission transverse x-coordinate and time generated in the Bjorken-like model: all π^+ 's, direct π^+ 's, decay π^+ 's from ρ , ω , $K^*(892)$ and Δ	35
3.3	The π^+ emission transverse x-coordinate and time generated in the Hubble-like model: all π^+ 's, direct π^+ 's, decay π^+ 's from ρ , ω , $K^*(892)$ and Δ	35
3.4	The pseudo-rapidity ($-\ln \tan(\theta/2)$, θ is the particle production angle) distributions of charged particles in central Au + Au collisions at $\sqrt{s_{NN}} = 200$ GeV from the PHOBOS experiment and the MC calculations within the Bjorken-like and Hubble-like models.	37
3.5	The π^+ , K^+ and proton transverse momentum spectra at mid-rapidity $y \approx 0$ in central Au + Au collisions at $\sqrt{s_{NN}} = 200$ GeV from PHENIX experiment and the MC calculations within the Bjorken-like and Hubble-like models. Model results obtained with the strangeness suppression parameter $\gamma_s = 0.8$	38
3.6	The contributions to the π^+ transverse momentum spectrum at mid-rapidity in central Au + Au collisions at $\sqrt{s_{NN}} = 200$ GeV calculated within the Bjorken-like model.	39
3.7	The $\pi^\pm \pi^\pm$ correlation radii and the suppression parameter λ at mid-rapidity in central Au + Au collisions at $\sqrt{s_{NN}} = 200$ GeV from the STAR experiment and the MC calculations within the Bjorken-like model in different intervals of the pair transverse momentum k_t	41
3.8	The typical hydrodynamic evolution scenario.	45

3.9	m_t -spectra (in c^4/GeV^2) measured by the STAR Collaboration for π^+ , K^+ and p at 0 – 5% centrality in comparison with FASTMC calculations.	52
3.10	m_t -spectra (in c^4/GeV^2) measured by the STAR Collaboration for π^+ , K^+ and p at different centralities in comparison with fast MC calculations.	54
3.11	The p_t -dependence of v_2 measured by the STAR Collaboration [98] for charged particles at different centralities in comparison with fast MC calculations.	56
3.12	The p_t -dependence of v_2 measured by the STAR Collaboration for charged particles at centrality 20–30% in comparison with fast MC calculations under assumption of the single freeze-out.	57
3.13	The π^+ correlation radii at mid-rapidity in central Au+Au collisions at $\sqrt{s_{NN}} = 200$ GeV from the STAR experiment and MC calculations within the Bjorken-like model in different intervals of the pair transverse momentum k_t	59
3.14	Squared correlation radii simulated with FASTMC versus the azimuthal angle Φ of the $\pi^+\pi^+$ pair with respect to the reaction plane, 20-30 % centrality events in different k_T (GeV/ c) intervals.	61
4.1	The energy density over T^4 as a function of the temperature T . . .	64
4.2	Particle ratios from hybrid model calculations as compared to the statistical model, and to data.	65
4.3	Elementary parton-parton scattering. The symbolic parton ladder is used.	67
4.4	The complete picture of initial conditions, including remnants. . . .	67
4.5	Inner contributions, from the parton ladder (full lines), and “outer” contributions, from the remnants, to the rapidity distribution of hadrons.	68
4.6	The two elements of the multiple scattering theory: open ladders, representing inelastic interactions, and closed ladders, representing elastic interactions.	69
4.7	Energy density versus temperature, for our equation-of-state X3F, compared to lattice data, and some other EoS choices.	72
4.8	Pressure versus temperature, for our equation-of-state X3F, compared to lattice data, and some other EoS choices.	73
4.9	Centrality dependence of the ratio of v_2 over eccentricity.	82
4.10	Centrality dependence of the ratio of v_2 over eccentricity, for different scenario.	83

4.11	Pseudorapidity distributions of the elliptical flow v_2 for minimum bias events and different centrality classes, in Au-Au collisions at 200 GeV.	84
4.12	Production of pions in Au-Au collisions at 200 GeV: transverse momentum spectra for central collisions at different rapidities.	85
4.13	Production of lambdas (left) and antilambdas (right) in Au-Au collisions at 200 GeV: transverse momentum distributions at rapidity zero for different centrality classes, the 0-5%, the 20-30%, and the 40-50% most central collisions.	86
4.14	Femtoscopic radii R_{out} , R_{side} , and R_{long} , as well as λ as a function of m_T for different centralities (0-5% most central, 5-10% most central, and so on).	88
4.15	The mean transverse momentum component p_x of π^+ as a function of the x coordinate of the emission point. Also shown is the number of produced π^+ as a function of x	89
4.16	Same as fig. 4.15, but for the calculation without hadronic cascade.	89
4.17	Same as fig. 4.15, but for the full thermal scenario (freeze-out at 130 MeV).	90
4.18	Same as fig. 4.14, but the calculations are done without hadronic cascade or with a hydrodynamic evolution through the hadronic phase with freeze-out at 130 MeV.	91
5.1	The pion emission function for different p_T in hydro-kinetic model (HKM).	103
5.2	Transverse momentum spectrum of π^- in HKM, compared with the sudden freeze-out ones at temperatures of 80 and 160 MeV with arbitrary normalization.	104
5.3	The emission function in HKM for particles with momentum directed along the radius vector at the emission points and for those ones in the opposite direction to the radius vector.	105
5.4	Equation of state $p(\epsilon)$ used in the HKM calculations.	122
5.5	The transverse momentum spectra of negative pions, negative kaons and interferometry radii and R_{out}/R_{side} ratio for $\pi^-\pi^-$ pairs and mixture of K^-K^- and K^+K^+ pairs, all calculated in the HKM model. The experimental data are taken from the STAR and PHENIX collaborations.	124
5.6	The ϕ_p -integrated emission functions of negative pions and negative kaons with different momenta at the Glauber IC.	125

- 5.7 The p_T -integrated emission functions of negative pions for the top SPS, RHIC and LHC energies (top); the interferometry radii (middle) R_{out}/R_{side} ratio and transverse momentum spectra (bottom) of negative pions at different energy densities, all calculated in HKM model. The experimental data are taken from CERES, NA-49 (SPS CERN), STAR, PHENIX (RHIC BNL) collaborations. 127

LIST OF TABLES

3.1	FASTMC model parameters for central Au + Au collisions at $\sqrt{s_{NN}} = 200$ GeV for different freeze-out parametrizations.	34
3.2	Particle number ratios near mid-rapidity in central Au + Au collisions at $\sqrt{s_{NN}} = 130$ GeV calculated in FASTMC.	36
3.3	Particle number ratios near mid-rapidity in central Au + Au collisions at $\sqrt{s_{NN}} = 200$ GeV calculated in FASTMC with different set of thermodynamic parameters.	36
3.4	FASTMC model parameters for central Au + Au collisions at $\sqrt{s_{NN}} = 200$ GeV with separate chemical and thermal freeze-outs.	51
3.5	FASTMC model parameters for Au + Au collisions at $\sqrt{s_{NN}} = 200$ GeV at different centralities.	51

1.1 Introduction

The idea of exploiting the laws of ideal hydrodynamics to describe the expansion of the strongly interacting matter that is formed in high energy hadronic collisions was first formulated by Landau [1] in 1953 as an improvement over the Fermi statistical model [2] for the multiple particle production phenomena in high-energy nuclear collisions. At that time, these phenomena were observed in cosmic rays. Although the Fermi model offered an ingenious insight into the mechanism of the high-energy nuclear collision processes and gave a prediction for the energy dependence of the multiplicity, which was verified by the data, it was known that it had troubles in reproducing particle spectra and relative abundance of K over π .

These problems were solved by letting the hot and dense matter to expand and equilibrate before particle emission takes place, reducing thus heavy-particle multiplicities, because of the Boltzmann factor, and giving at the same time elongated momentum spectra, due to a violent longitudinal expansion caused by a large pressure gradient in the beam direction. A nice feature of this model is that, since the entropy is conserved in the ideal case Landau studied, the energy dependence of the total particle multiplicity predicted by the Fermi model, and verified experimentally, is preserved.

When accelerator data on multiparticle production began to appear, first in pp collisions at CERN ISR, and later in $\bar{p}p$ collisions at $S\bar{p}pS$ collider, Carruthers [3] revived this *Heretical Model* in 1974, showing that several aspects of those phenomena may be well understood within Hydrodynamic Model. When laboratory study of high-energy heavy-nucleus collisions started, Hydrodynamic Model became one of the essential tools for these investigations.

The original motivation for heavy ion program was not just increase the number of secondary particles produced per event (up to several thousands at RHIC), but to reach a qualitatively different dynamical regime, characterized by a small microscopic scale l (e.g. mean free path) as compared to the macro scale L (the system's size): $l \ll L$. If this were achieved, the fireball produced in heavy ion collisions would be treated as a macroscopic body, with thermo and (viscous) hydrodynamics.

Statistical models do indeed work well for heavy ion collisions, in a wide range of collision energies. They also work for pp or e^+e^- collisions – analysis involving conservation laws treatment [5, 37] shows the presence of collective flow in pp or e^+e^- , however less strong than in A+A collisions, despite the fact that multi-body excited systems produced in the former cases are not macroscopically large.

Hydrodynamic models are successfully applied for analysis of high energy nuclear collisions at CERN SPS and especially at BNL RHIC (for reviews see, e.g., Refs. [13, 14, 15]), where the utilization of ideal hydrodynamics was supported by theoretical results: it was advocated [16] that deconfined matter behaves like a perfect liquid. In particular, hydrodynamic models are applied for soft-physics description, with typical particle momentum below 2 GeV/c, where the most ($\sim 99\%$) of particles are emitted.

1.2 Particle distributions

In this section we introduce the basic observables measured in the experiments and define the particular quantities which will be referred to in the next chapters.

Heavy ion collision at energies achieved in modern accelerators produce a variety of stable and unstable hadrons (π, K, p, n, \dots) which are detected then. The particle number ratios for dozen of lightest hadron states produced is well described using the simple thermal model, basically with only 2 free parameters: temperature T and baryon chemical potential μ_B [56]. Thermal model indeed describes particle number ratios well for a wide range of collision energies, centralities and collided nuclei, which is a most basic hint for the thermalized character of matter produced in heavy ion collisions.

Unfortunately, the small size and short lifetime prohibits direct observation of the space-time scales of the fireball in heavy-ion collisions. One measures instead the particle distribution three-momenta and energies. Spatial information must be extracted then indirectly using momentum correlations.

The particle momentum is convenient to represent in terms of transverse momentum \vec{p}_T and longitudinal rapidity $y = \frac{1}{2} \ln \frac{E+p_z}{E-p_z}$, which has a simple transfor-

mational properties under the Lorentz transformations (boosts) in z direction.

$$p^0 \frac{d^3 n_i}{d^3 \vec{p}_i} = \frac{d^3 n_i}{d^2 \vec{p}_T dy} \quad (1.1)$$

Transverse momentum distributions are obviously connected with the dynamics of the system in transverse direction, and are important for the study within collective models of matter evolution. The reason is that initially, just after the collision, there are no collective flows in transverse direction, and the transverse flow development is determined by the dynamical properties of matter at both early pre-thermal and subsequent thermal stages of evolution.

The transverse spectrum possess the exponential behavior as a function of transverse particle mass:

$$\frac{d^2 n}{2\pi p_T dp_T dy} \propto e^{-\sqrt{m^2 + p_T^2}/T_{eff}}$$

The inverse slope in log scale is called the effective temperature T_{eff} of particle spectra. In a model without transverse flow, particle spectra exhibit m_T -scaling, i.e. after appropriate rescaling of the yields all spectra collapse onto a single curve. Transverse flow breaks this picture, and actually mass dependence of T_{eff} for different sorts of hadrons is generally reproduced by hydrodynamic simulations for both SPS and RHIC heavy ion collisions and reflects the idea that all particle species are involved in common collective flow.

Due to nonzero impact parameter most of the collisions are asymmetric in transverse direction. Then, thermalization assumption and subsequent hydrodynamic evolution picture tell us that due to different values of gradients in x and y directions for initial distributions, anisotropic flow develops in transverse plane. Since the most probable velocity of particle emitted from fluid element coincides with the flow velocity, this results in anisotropic distribution of transverse momenta. For this analysis it is convenient to make a Fourier expansion of hadron spectrum in the azimuthal angle φ_p of three-momentum:

$$\frac{dN}{d^2 \vec{p}_T dy} = \frac{dN}{2\pi p_T dp_T dy} (1 + 2v_2 \cos(2\varphi_p) + \dots) \quad (1.2)$$

Due to reflection symmetry with respect to the reaction plane (see definition below), only cosine terms appear in the expansion. Here we also restrict the expansion to mid-rapidity region ($y = 0$), where all odd harmonics, in particular, directed flow coefficient v_1 vanish. The second coefficient divided by 2 is called elliptic flow coefficient. The coefficients can be determined by e.g. :

$$v_2 = \frac{\int_0^{2\pi} d\varphi \cos 2(\varphi - \psi_R) \frac{d^3 N}{dy d\varphi p_T dp_T}}{\int_0^{2\pi} d\varphi \frac{d^3 N}{dy d\varphi p_T dp_T}}, \quad (1.3)$$

where ψ_R is so-called reaction plane angle. Reaction plane is defined as the plane built by the vectors of impact parameter of collision and z axis (collision axis) basis vector.

The elliptic flow coefficients v_2 are measured for most abundant particle species : π^\pm , K^\pm , p , \bar{p} , etc, and by the definition reflect the anisotropy of the transverse momentum distribution. One of the most spectacular features of the RHIC data is 50% bigger elliptic flow [81] compared to the observations at CERN SPS [17]. The development of a strong flow is well described by the hydrodynamic models and is underestimated in transport models, which points to the essential property of strong interaction of matter created in RHIC collisions. It was argued that elliptic flow description requires small thermalization time τ_0 less than 1 fm/c, which defines the start of hydrodynamic expansion. Such fast thermalization is hard to prove theoretically. However, recent developments show that whereas the assumption of thermalization in relativistic A + A collisions is really crucial to explain soft physics observables in general (and particularly v_2), the hypotheses of early thermalization at times less than 1 fm/c is not necessary [6, 18].

1.3 Correlation functions

Another class of measurements in A+A collisions are two-particle correlations, measured primarily for pions, but also for kaons. The two-particle correlation function is defined as the ratio of Lorentz-invariant two-particle distribution to the product of the two single particle distributions :

$$C(\vec{p}_1, \vec{p}_2) = \frac{p_1^0 p_2^0 d^6 n / d^3 \vec{p}_1 d^3 \vec{p}_2}{(p_1^0 d^3 n / d^3 \vec{p}_1) (p_2^0 d^3 n / d^3 \vec{p}_2)} \quad (1.4)$$

First in $p\bar{p}$ collisions at Bevatron, an enhancement of pion pairs at small relative momenta (the 'GGLP-effect'), was found by G. Goldhaber, S. Goldhaber, W.Y. Lee and A. Pais [63] and explained in terms of the finite space-time extent of the decaying $p\bar{p}$ -system and Bose-Einstein statistics of the detected identical pions. Since the width of the correlation effect is related to the characteristic space-time separation of the pion emitters, the corresponding technique acquired the name Correlation femtoscopy. As noticed by G.I. Kopylov and M.I. Podgoretsky, a similar though orthogonal effect exists in astrophysics and is the base of intensity interferometry proposed by the radio astronomer Robert Hanbury Brown and Richard Twiss to measure the angular radii of distant stellar objects. They demonstrated [75] that photons in an apparently uncorrelated thermal beam tend to be detected in close-by pairs. This photon bunching or HBT-effect, first explained theoretically by Purcell [134]. Since the width of the space-time bunching (HBT) effect is

related to the characteristic spread of the photon wave vectors (three-momenta), the corresponding technique acquired the name Correlation spectroscopy.

Basically, identical particles which sit nearby in phase-space experience quantum statistical effects resulting from the (anti)symmetrization of the multiparticle wave function. For bosons, therefore, the two-particle probability shows an enhancement at small momentum difference between the particles.

The most direct connection between the measured two-particle correlations in momentum space and the source distribution in coordinate space can be established if the particles are emitted independently ('chaotic source') and propagate freely from source to detector. Basically, particles with particular value of velocity are emitted most probably from the region with the same value of collective flow velocity, which gives the connection of momentum and coordinate correlation.

The two-particle correlator yields rms widths of the effective source of particles with momentum p . In general, these width parameters do not characterize the total extension of the collision region. They rather measure the size of the system through a filter of wavelength p . In the language introduced by Sinyukov [9] this size is the local 'region of homogeneity', the region from which particle pairs with momentum K are most likely emitted. From the other hand, the local length of homogeneity is defined by the behavior of the Wigner function : it means the length within which the deviation of Wigner function is relatively small and is about the function value.

From the data of relativistic heavy-ion experiments, the two-particle correlator is usually constructed as a ratio of two-particle distribution in samples of so-called actual pairs and 'mixed' pairs or reference pairs. One starts by selecting events from the primary data set. Actual pairs are pairs of particles that belong to the same event. Reference pair partners are picked randomly from different events within the set of events that yielded the actual pairs. The correlation function is then constructed by taking the ratio, bin by bin, of the distribution D_A of these actual pairs with the distribution D_R of the reference pairs [8, 12]

$$D_A(\Delta q, \Delta K) = \frac{\text{number of actual pairs in bin } (\Delta q, \Delta K)}{\text{number of actual pairs in sample}}, \quad (1.5)$$

$$D_R(\Delta q, \Delta K) = \frac{\text{number of reference pairs in bin } (\Delta q, \Delta K)}{\text{number of reference pairs in sample}}, \quad (1.6)$$

$$C(\Delta q, \Delta K) = \frac{D_A(\Delta q, \Delta K)}{D_R(\Delta q, \Delta K)}. \quad (1.7)$$

Momentum correlations between identical particles can originate not only from quantum statistics but also from conservation laws and final state interactions. Energy-momentum conservation constrains the momentum distribution of produced particles near the kinematical boundaries. In high multiplicity heavy-ion

collisions its effects on two-particle correlations at low relative momenta are negligible. Similarly, constraints from the conservation of quantum numbers (e.g. charge or isospin) become less important with increasing event multiplicity. Strong correlations exist between the decay products of resonances, but since resonance decays rarely lead to the production of identical particle pairs, they do not matter in practice. This leaves final state interactions as the most important source of additional femtoscopic correlations. For the small relative momenta $q < 100$ MeV which are sampled in the two-particle correlator, effects of the strong interactions are negligible for identical charged pions. For protons, however, they dominate the two-particle correlations. On the other hand, for pions, the long-range Coulomb interactions distort significantly the observed momentum correlations, dominating over the Bose-Einstein effect for small relative momenta. The aim of Coulomb corrections is to modify the measured two-particle correlations in such a way that the resulting correlator contains only Bose-Einstein correlations, while the effects of final state interactions have been subtracted. For this, several simplified procedures have been used in the literature. The effective method of subtraction of effects from the long-lived resonances and Coulomb final state interaction is Bowler-Sinyukov procedure [10], now used by majority of experimental collaborations.

1.4 Evolution picture

From the dynamical point of view, a process of heavy ion collision at ultra-relativistic energies can be divided into several stages. The matter produced during the collision have different properties at different stages. So, one can distinguish:

- the initial conditions for the collision at $\tau < 0$ are two nuclei approaching each other with velocity $v > 0.99999c$ (at RHIC).
- There are several microscopic models of initial, pre-equilibrium stage of collision:
 - in *Color Glass Condensate* (CGC) approach, the initial state of colliding nuclei is described in terms of dense gluon walls, see Section 5.4.3;
 - *EPOS* is a flux-tube approach, compatible with accelerator data for proton-proton, proton-nucleus collisions, and cosmic-ray data for air shower simulations (for more details, see Section 4.2).

In this very early pre-equilibrium stage, the primary collisions between fast partons inside the colliding nuclei also generate “hard probes” with either large mass or large transverse momentum, such as heavy quark pairs ($c\bar{c}$ and $b\bar{b}$), pre-equilibrium real or virtual photons, and very energetic quarks and

gluons with large transverse momentum (from which jets are formed after hadronization).

As a result of initial stage, the matter is supposed to become locally thermalized, thus forming the initial conditions for the next stage of evolution. The conventional thermalization time for v_2 data reproduction is less than 1 fm/c (at RHIC), however, recent developments show that hypothesis of early thermalization at times less than 1 fm/c is not necessary [6, 18].

- The subsequent evolution of thermalized medium can be described using the equations of relativistic hydrodynamics. This approach allows one to account for the complicated evolution of the system at a preconfined stage and in the vicinity of the possible phase transitions by means of a corresponding equation of state (EoS). The question concerning the viscosity coefficients is still open.
- However, hydrodynamic picture implies the picture of continuous medium. Thus, hydrodynamic stage continues until the picture of the continuous medium is destroyed. Roughly, it happens when the mean free path of particles (connected with the rate of collisions) becomes comparable with the smallest characteristic dimension of the system: its geometrical size or hydrodynamic length. This condition determines the space-time region, where hydrodynamic picture is applicable.
- The further expansion makes the system to be more and more rarefied, however hadrons continue to interact, mostly via elastic scatterings. At this (kinetic) stage of evolution, the appropriate tools are cascade models. Cascade model studies show us that the tails of interactions (collisions) continue upto 50-100 fm/c. The decays of long-lived resonances happen much later. Finally, free particles propagate to detectors.

1.5 Dynamic models

To complete hydrodynamic model, particularly model based on ideal fluid approximation, one needs the initial conditions for hydrodynamic evolution, equation of state (which close the set of hydrodynamic equations), boundary conditions and the criterion to stop hydrodynamic evolution (final conditions). The most clear part is boundary conditions, which are usually taken to be non-reflective, which corresponds to the matter, expanding into vacuum. The rest of the conditions have to be obtained from, e.g. microscopic models, which are external to hydrodynamics.

Evidently, the simplest receipt of final conditions for hydrodynamic evolution is the Cooper-Frye prescription (CFp) [44] which ignores the post-hydrodynamic (kinetic) stage of matter evolution and assumes that perfect fluid hydrodynamics is valid till some 3D hypersurface, e.g., as was supposed by Landau [1], till the isotherm $T \simeq m_\pi$, where sudden transition from local thermal equilibrium to free streaming is assumed. This approach is extensively used in modern hydrodynamical models of evolution for A+A collisions.

Concerning final conditions and post-hydrodynamical stage treatment, different scenarios have been used so far.

The most simple scenario is “Blast-wave” model, first appeared in the attempt to interpret RHIC data [11]. In such models, a parametrization of freeze-out hypersurface and velocity distribution on it, instead of preceding hydrodynamic evolution calculation, is used. More sophisticated blast-wave-type models are used to fit experimental data. Successful attempts to describe simultaneously the momentum-space measurements and the freeze-out coordinate-space data were done in several models: “Kiev-Nantes” model [48], “Blast-Wave” parametrizations [37], “Buda-Lund” hydro-inspired approach [89]. Some parametrizations, e.g. [48] can be justified by the qualitative agreement with isotherms obtained in hydrodynamic calculations.

More sophisticated models treat the decays of resonances created at freeze-out hypersurface together with stable particles (e.g. THERMINATOR code in its initial form [87, 88], or FASTMC code [79, 80]). Freeze-out can be obtained from hydrodynamic calculations or parametrized.

However, sharp freeze-out at some 3D hypersurfaces is a rather rough approximation of the spectrum formation, because the process of particle emission from fireballs created in high energy heavy ion collisions is gradual in time. Results of many studies based on cascade models (see below) contradict the idea of sudden freeze-out and demonstrate that in fact particles are emitted from the 4D volume during the whole period of the system evolution, and deviations from local equilibrium conditioned by continuous emission should take place (see, e.g., [93]). Moreover, freeze-out hypersurfaces typically contain non-space-like parts that lead to a problem with energy-momentum conservation law in realistic dynamical models [47].

To overcome the difficulties of Landau/Cooper-Frye prescription, one can simulate matter dynamics at the late stages of system evolution by the means of kinetic codes which treat classical particle interactions with given cross-sections. The hydrodynamic evolution should be coupled then to kinetic code at e.g. isotherm of sufficiently low temperature, where hydrodynamic picture is destroyed (switching hypersurface). At this hypersurface the continuous medium converses into the set of particles according to the thermal distribution. Such “*hybrid*” scheme is imple-

mented in a number of calculations, see e.g. [13, 14, 15]. However, the remarks concerning non-space-like parts of switching hypersurface are applicable as well for hybrid models. Also in hybrid picture the initial conditions for hadronic cascade calculations, formulated also on *space-like* part of hypersurface where, however, hadronic distributions deviate from the local equilibrium, in particular, because of an opacity effect for hadrons which are created during a “mixed” stage of phase transition. These nonequilibrium effects can seriously influence the results of hybrid models in their modern form [201].

Generally, the realizations of hybrid scheme, despite of its physical superiority over the simple Cooper-Frye prescription, did not give a good description of two-particle correlation functions reflected in femtoscopic radii, being the measure of space-time scales of collision process.

Most existing calculations with hybrid models are still done using an unrealistic equation-of-state with a first order phase transition, based on ideal gases of quarks & gluons and hadrons. As shown later, it actually makes a big difference using a realistic equation-of-state, which is for $\mu_B = 0$ compatible with lattice results. In particular, HBT radii cannot be reproduced together with other observables using the EoS with first-order phase transition.

The calculations of [115, 116] manage to reproduce both particle yields and transverse momentum spectra of pions, kaons, and protons within 30%, for p_t values below 1.5 GeV/c. The net baryon yield cannot be reproduced, since the calculations are done for zero baryon chemical potential, another systematic problem is due to a relatively small hadron set. A bigger hadron set will produce essentially more pions and will thus reduce for example the pion / kaon ratio.

The calculations [7, 190] reproduce simultaneously the pion, kaon and proton transverse momentum spectra, v_2 and pion HBT radii. However, the value of chemical freeze-out temperature used is not compatible with the results from particle number ratios analysis. This also results in inability to describe the yields for massive hadrons (Λ, Ξ).

Some sophisticated hybrid models (e.g. AMPT [86]) reproduce the elliptic flow and the correlation radii but with different sets of model parameters. Only recently the results obtained from hydrodynamic model connected with THERMINATOR afterburner, qualitatively describe HBT radii together with momentum spectra and anisotropy coefficient v_2 , however the parameters used are not physical.

1.6 Outline of the thesis

Thus, the aim of the present work is to construct dynamic model for A+A collisions, compatible with HBT measurements.

In the thesis, the results of this research are presented in a following order. In

Chapter 2, new class of analytic solutions of the equations of relativistic hydrodynamics is presented, its possible applications to the dynamics of A+A collisions are discussed. In Chapter 3, event generator, based on freeze-out hypersurface parametrization is constructed. As a continuation of research towards construction of realistic dynamical model for A+A collisions, a hybrid dynamical model (initial state + hydrodynamics + cascade) is presented in Chapter 4. Finally, in Chapter 5 the hydro-kinetic model is presented, as a combination of hydrodynamic and kinetic approaches.

Hydrodynamic solutions

In this chapter, the new family of solutions of relativistic hydrodynamic equations for ideal fluid case is presented. In particular, solutions corresponding to ellipsoidally symmetric expansion of finite systems into vacuum are analyzed. The properties of the solution obtained, as well as possible applications to A+A collisions dynamics, are discussed.

2.1 Introduction

The equations of the relativistic hydrodynamics have highly nonlinear nature and, therefore, only a few analytical solutions are known until now. For the first time one-dimensional, or (1+1), analytical solution for Landau initial conditions - hot pion gas in Lorentz contracted thin disk [1], has been obtained by Khalatnikov [19]. The equation of state (EoS) was chosen as ultrarelativistic one: $p = c_0^2 \varepsilon$, $c_0^2 = 1/3$. It is noteworthy that according to that solution the longitudinal flows developed to the end of hydrodynamic expansion, at freeze-out, are quasi-inertial: $v \approx x_L/t$. Much later, in the papers [20] the infinite (1+1) boost-invariant solution have been found for the same EoS. For finite systems the similar approach was developed in Ref.[21]. The property of quasi-inertia preserves in these solutions during the *whole* stage of the evolution. Bjorken [22] utilized these solutions as the basis of the hydrodynamic model for ultra-relativistic A+A collisions.

The spherically symmetric variant of such a kind of flows with the Hubble velocity distribution, $v = r/t$, has been considered in Ref. [23]. Some generalization of these results was proposed in a case of the Hubble flow for EoS of massive gas with conserved particle number in Ref.[24] and for the cylindrically symmetric boost-invariant expansion with a constant pressure in [25].

All these solutions were used for an analysis of ultra-relativistic heavy ion col-

lisions. Since the longitudinal boost-invariance in a fairly wide rapidity region is not observed even at RHIC, as it was expected, the Hubble-like models are also used now for a description of the experimental data [26]. It is natural, however, that unlike to the Hubble type flows, the velocity gradients should be different in different directions since there is an initial asymmetry between longitudinal and transverse directions in central A+A collisions and, in addition, between in-plane and off-plane transverse ones in non-central collisions. In this letter we make a general analysis of the hydrodynamic equations for the quasi-inertial flows aiming to find a new class of analytical solutions with 3D asymmetric relativistic flows.

2.2 General analysis

Let us start from the equations of relativistic hydrodynamics:

$$\partial_\nu T^{\mu\nu} = 0, \quad (2.1)$$

where the energy-momentum tensor corresponds to a perfect fluid:

$$T^{\mu\nu} = (\varepsilon + p)u^\mu u^\nu - p \cdot g^{\mu\nu} \quad (2.2)$$

We can attempt to find a particular class of solutions and therefore have to make some simplifications of (2.1). We do not fix EoS at this stage.

- Let us put the condition of quasi-inertiality

$$u^\nu \partial_\nu u^\mu = 0 \quad (2.3)$$

which means that flow is accelerationless in the rest systems of each fluid element; this property holds for the known Bjorken (boost-invariant) and Hubble flows.

Then, we find that $u^\mu[(\varepsilon + p)\partial_\nu u^\nu + u^\nu \partial_\nu \varepsilon] + [u^\mu u^\nu \partial_\nu p - \partial^\mu p] = 0$. Contracting this equation with u_μ we get

$$(\varepsilon + p)\partial_\nu u^\nu + u^\nu \partial_\nu \varepsilon = 0. \quad (2.4)$$

Obviously, the remaining equation to satisfy is:

$$u^\mu u^\nu \partial_\nu p - \partial^\mu p = 0 \quad (2.5)$$

The task is to find solution of the system (2.3),(2.4) and (2.5). As one can see, the number of equations exceeds the number of independent variables. So, the equations must be self-consistent in order to have nontrivial solutions.

We see that Eq.(2.4) can be rewritten in the form:

$$u^\mu \partial_\mu \varepsilon = -F(\varepsilon)(\partial_\nu u^\nu) \quad (2.6)$$

where $F(\varepsilon) = \varepsilon + p$, and Eq.(2.5) as the following:

$$p'(\varepsilon)(u^\mu u^\nu \partial_\nu \varepsilon - \partial^\mu \varepsilon) = 0, \quad (2.7)$$

supposing EoS in the form $p = p(\varepsilon)$. If $p'(\varepsilon) \neq 0$

$$u^\mu F(\varepsilon)(\partial_\nu u^\nu) + \partial^\mu \varepsilon = 0. \quad (2.8)$$

Normally $F(\varepsilon) \neq 0$, and we can divide the last equation by $F(\varepsilon)$ and introduce the function $\Phi(\varepsilon)$ by the definition $\frac{1}{\varepsilon+p(\varepsilon)} = \Phi'(\varepsilon)$, so that

$$\partial^\mu \Phi(\varepsilon) = -u^\mu (\partial_\nu u^\nu) \quad (2.9)$$

Then, the conditions of consistency of equations (2.4) and (2.5) can be written as:

$$\partial^\lambda (u^\mu \partial_\nu u^\nu) = \partial^\mu (u^\lambda \partial_\nu u^\nu) \quad (2.10)$$

In general case, there are 6 independent equations.

Finally, the relativistic hydrodynamics of quasi-inertial flows is described by the equations (2.3) and (2.10) for the hydrodynamic velocities u^μ , and the equations (2.9) for the energy density: one should use derivative $\frac{1}{\varepsilon+p(\varepsilon)} = \Phi'(\varepsilon)$ at any EoS $p = p(\varepsilon)$ to find function $\varepsilon(x)$. A serious problem is, however, to find non-trivial solutions for the field $u^\mu(x)$ of hydrodynamic 4-velocities.

2.3 Gradient-like velocity ansatz

One can try to satisfy to Eqs. (2.3),(2.10) for velocity profile by a use of gradient-like representation for it, namely,

$$u^\mu = \partial^\mu \phi. \quad (2.11)$$

with condition of normalization, $u^\mu u_\mu = 1$:

$$\partial_\mu \phi \partial^\mu \phi = 1 \quad (2.12)$$

Then one can check that (2.3) is satisfied automatically, and (2.10) leads to:

$$\partial^\lambda (\partial^\mu \phi \cdot \square \phi) = \partial^\mu (\partial^\lambda \phi \cdot \square \phi) \quad (2.13)$$

Thus, gradient-like velocity ansatz (2.11) reduce the problem to equations (2.12),(2.13).

One can see that the above equation can be, in particular, reduced to:

$$\square\phi = F(\phi) \quad (2.14)$$

with any real function F that have to be solved together with (2.12). Note that if $F(\phi) = a + b\phi$ then (2.14) is the linear inhomogeneous partial differential equation (PDE) and its any solution is a partial solution ϕ_{ih} of inhomogeneous PDE, plus general solution ϕ_h of correspondent homogenous PDE (if $b \neq 0$):

$$\begin{aligned} \phi_{ih} &\sim (t^2 - \mathbf{x}^2), b = 0 \\ \phi_{ih} &\sim -\frac{a}{b}, b \neq 0 \end{aligned} \quad (2.15)$$

and

$$\phi_h = \int d^4p \delta(p^2 - b) f(p) e^{ipx} \quad (2.16)$$

where $f(p)$ is arbitrary function with properties $f^*(k) = f(-k)$. Then the problem is reduced to a solution of the nonlinear integral equation (2.12) for $f(p)$. If $a = b = 0$, the only potential $\phi = c + c_0 t + \sum c_i x_i$ ($i = 1, 2, 3$) with the constrain on the constants $c_\nu : c_0^2 - \sum c_i^2 = 1$ satisfies these equations. It describes a relativistic motion of a medium as a whole. It is an open problem whether there are analytical solutions at $a \neq 0$ and/or $b \neq 0$.

The known quasi-inertial solutions correspond to $F(\phi) = n/\phi$ in Eq.(2.14). The value $n = 1$ generates gradient ansatz $\phi = \sqrt{t^2 - z^2}$ that gives the (1+1) boost-invariant Bjorken expansion along axis z , $v = z/t$; $n = 2$ leads to $\phi = \sqrt{t^2 - x^2 - y^2}$, and, correspondingly, to the two-dimensional (1+2) Hubble-like flow with cylindrical symmetry; at $n = 3$ one can get solution of (2.14) for ϕ in the form $\phi = \tau \doteq \sqrt{t^2 - x^2 - y^2 - z^2}$ describing spherically symmetric Hubble flow $u^\mu = x^\mu/\tau$. The equation (2.9) has the form $\partial^\mu \Phi(\varepsilon) = n x^\mu/\tau^2$ where number of space coordinates is equal to n . Then the energy density is described by the following expression

$$\int_{\varepsilon(\tau_0)}^{\varepsilon(\tau)} \frac{d\varepsilon}{\varepsilon + p(\varepsilon)} = \ln\left(\frac{\tau_0}{\tau}\right)^n. \quad (2.17)$$

2.4 Relativistic ellipsoidal solutions

One more possibility to satisfy to Eqs. (2.5) or (2.7) besides of the gradient-like flows is to suppose a constant pressure in the EoS: $p'(\varepsilon) = const$. This possibility was first used in [25] as physically corresponding to a thermodynamic state of the system in the softest point with the velocity of sound $c_s^2 = 0$. Such a state could be associated with the first order phase transition. In A+A collisions it corresponds,

probably, to transition between hadron and quark-gluon matter at SPS energies. The solution proposed in [25] has the cylindrical symmetry in the transverse plane and the longitudinal boost invariance:

$$u_\mu = \gamma\left(\frac{t}{\tau}, v\frac{x}{r}, v\frac{y}{r}, \frac{z}{\tau}\right), \quad (2.18)$$

where $\tau = \sqrt{t^2 - z^2}$, $\gamma = (1 - v^2)^{-1/2}$ and r is transverse radius, $r = \sqrt{x^2 + y^2}$,

$$v = \frac{\alpha}{1 + \alpha\tau}r \quad (2.19)$$

describes axially symmetric transverse flow.

The above solution has, however, a limited region of applicability since the boost invariance is not expected at SPS energies and can be used only in a small mid-rapidity interval [27], it is not reached even at RHIC energies [28]. Most important, however, is that in non-central collisions there is no axial symmetry and, therefore, one needs transversely asymmetric solutions to describe the elliptic flows in these collisions, e.g., v_2 coefficients. Now we propose a new class of analytic solutions of the relativistic hydrodynamics for 3D asymmetric flows.

First we construct the ansatz for normalized 4-velocity:

$$u^\mu = \left\{ \frac{t}{\sqrt{t^2 - \sum a_i^2(t)x_i^2}}, \frac{a_k(t)x_k}{\sqrt{t^2 - \sum a_i^2(t)x_i^2}} \right\} \quad (2.20)$$

where the Latin indexes denote spatial coordinates and a_i are functions of time only. In this case a set of nonequal a_i induces 3D elliptic flow with velocities $v_i = a_i(t)x_i/t$: at any time t the absolute value of velocity is constant, $\mathbf{v}^2 = const$, at an ellipsoidal surface $\sum a_i^2 x_i^2 = const$. Note that this solution is not gradient-like, so we follow in a specific way the analysis starting from (2.3).

The condition (2.3) of accelerationless in this case is reduced to the ordinary differential equation (ODE) for the functions $a_i(t)$:

$$\frac{da_i}{dt} = \frac{a_i - a_i^2}{t}, \quad (2.21)$$

the general solution of which is:

$$a_i(t) = \frac{t}{t + T_i}, \quad (2.22)$$

where T_i is some set of 3 parameters (integration constants) having the dimension of time. The different values T_1 , T_2 and T_3 result in anisotropic 3D expansion with the ellipsoidal flows.

The equation (2.5) is satisfied since we assume the constant pressure profile: $p = p_0 = \text{const}$. The next step is to find solution of Eq. (2.4) for energy density ε . Taking into account that $\partial_\mu u^\mu = \sum a_i/\tilde{\tau}$, where

$$\tilde{\tau} = \sqrt{t^2 - \sum a_i^2 x_i^2}, \quad (2.23)$$

one can get

$$(\varepsilon + p_0) \sum_i a_i(t) + t \partial_t \varepsilon + \sum_i a_i(t) x^i \partial_i \varepsilon = 0. \quad (2.24)$$

General solution of the equation is

$$\varepsilon + p_0 = \frac{F_\varepsilon\left(\frac{x_1}{t+T_1}, \frac{x_2}{t+T_2}, \frac{x_3}{t+T_3}\right)}{(t+T_1)(t+T_2)(t+T_3)} \quad (2.25)$$

where F_ε is an arbitrary function of its variables. If one fixes the parameters T_i that define the velocity profile, then the function F_ε is completely determined by the initial conditions for the enthalpy profile, say, at the initial time $t = 0$: $\varepsilon(t = 0, \mathbf{x}) + p_0 = F_\varepsilon\left(\frac{x_1}{T_1}, \frac{x_2}{T_2}, \frac{x_3}{T_3}\right)/T_1 T_2 T_3$.

If some value, associated with a quantum number or with particle number in a case of chemically frozen evolution is conserved [27] then one should add the corresponding equation to the basic ones. Such an equation has the standard form [29]:

$$n \partial_\nu u^\nu + u^\mu \partial_\mu n = 0 \quad (2.26)$$

where n is associated with density of the correspondent conserved value, e.g., with the baryon or particle densities. A general structure of this equation is similar to what Eq. (2.24) has and, therefore, the solution looks like as (2.25):

$$n = \frac{F_n\left(\frac{x_1}{t+T_1}, \frac{x_2}{t+T_2}, \frac{x_3}{t+T_3}\right)}{(t+T_1)(t+T_2)(t+T_3)} \quad (2.27)$$

where the function F_n is an arbitrary function of its arguments and can be fixed by the initial conditions for (particle) density n : $n(t = 0, \mathbf{x}) T_1 T_2 T_3 = F_n\left(\frac{x_1}{T_1}, \frac{x_2}{T_2}, \frac{x_3}{T_3}\right)$.

To establish a behavior of other thermodynamic values we use link between different thermodynamic potentials $\varepsilon = Ts - p + \mu n$ and utilize the thermodynamic equations based on the free energy density $f(n, T) = \varepsilon - Ts = \mu n - p$. Since the volume is fixed (it is unit) the free energy depends on T and n only, $df = -sdT + \mu dn$, and the chemical potential $\mu = f_{,n|T=\text{const}}$ and the entropy density $s = -f_{,T|n=\text{const}}$.

In a case of chemically equilibrated expansion of the ultrarelativistic gas when the particle number is uncertain and is defined by the conditions and parameters of the thermodynamic equilibrium, e.g., by the temperature T , the chemical potential

$\mu \equiv 0$ (we suppose here that there are no other conserved values associated with charges, or the corresponding chemical potentials are zero or close to zero). Then $f = -p_0 = \text{const}$, $df = -sdT = 0$ that means the temperature $T = \text{const}$ for such a system and the entropy $s = (\varepsilon(t, \mathbf{x}) + p_0)/T$ where $\varepsilon(t, x)$ is defined by (2.25).

If chemically frozen evolution takes place, the chemical potential associated with conserved particle number is not zero and describes the deviation from chemical equilibrium in relativistic systems. The solution of differential equation $nf_{,n}|_{T=\text{const}} - p_0 = f(n, T)$ is $f(n, T) = nc(T) - p_0$, where $c(T)$ is some function of the temperature. Then it follows directly from the thermodynamic identities that

$$\varepsilon(t, \mathbf{x}) + p_0 = n(t, \mathbf{x})(c(T) - Tc'(T)) \quad (2.28)$$

Since the structures of general solutions for n and ε are found as (2.25) and (2.27), the temperature profile has the form

$$T(t, \mathbf{x}) = F_T\left(\frac{x_1}{t + T_1}, \frac{x_2}{t + T_2}, \frac{x_3}{t + T_3}\right) \quad (2.29)$$

where F_T is some function of its arguments that is defined by the initial conditions for ε and n and also by EoS $\varepsilon = \varepsilon(n, T)$. The latter can be fixed by a choice of the function $c(T)$ in Eq. (2.28). If the initial enthalpy density profile is proportional to the particle density profile, $F_n(\frac{x_1}{T_1}, \frac{x_2}{T_2}, \frac{x_3}{T_3}) \sim F_\varepsilon(\frac{x_1}{T_1}, \frac{x_2}{T_2}, \frac{x_3}{T_3})$, then $T = \text{const}$ (and so $\mu = c(T) = \text{const}$) during the system's evolution for any function $c(T)$ except the linear one: $c(T) = a - bT$ when T is not defined by the equation (2.28). In the last case $n = (\varepsilon + p_0)/a$, $s = bn$. In another particular case which corresponds to EoS $\varepsilon + p_0 = anT$ with $c(T) = -aT \ln(bT)$ one can get:

$$T(t, \mathbf{x}) = (\varepsilon + p_0)/(an), \quad s(t, \mathbf{x}) = an(\ln(bT) + 1) \quad (2.30)$$

2.5 Generalization of the Hubble-like flows

Let us describe some important particular solutions of the equations for relativistic ellipsoidal flows. If one defines the initial conditions on the hypersurface of constant time, say $t = 0$, then t is a natural parameter of the evolution. Such a representation of the solutions similar to the Bjorken and Hubble ones with velocity field $v_i = a_i x_i/t$ has property of an infinite velocity increase at $x \rightarrow \infty$. A real fluid, therefore, can occupy only the space-time region where $|\mathbf{v}| < 1$, or $\tilde{\tau}^2 > 0$. To guarantee the energy-momentum conservation of the system during the evolution, all thermodynamic densities have to be zero at the boundary of the physical region, otherwise one should consider the boundary as the massive shell [21]. Hence in the standard hydrodynamic approach the enthalpy and particle density must be zero at the surface defined by $|\mathbf{v}(t, \mathbf{x})| = 1$ at any time t . A

simple form of such a solution (for the case of particle number conservation) can be obtained from (2.25),(2.27) choosing $F_{\epsilon,n} \sim \exp\left(-b_\epsilon^2 \frac{t^2}{\tilde{\tau}^2}\right)$:

$$\varepsilon(t) + p_0 = \frac{C_\epsilon}{\prod_i (t + T_i)} \exp\left(-b_\epsilon^2 \frac{t^2}{\tilde{\tau}^2}\right), \quad (2.31)$$

$$n = \frac{C_n}{\prod_i (t + T_i)} \exp\left(-b_n^2 \frac{t^2}{\tilde{\tau}^2}\right) \quad (2.32)$$

where $\tilde{\tau}$ is defined by (2.23), and the constants C_ϵ , C_n , b_ϵ and b_n are determined by the initial conditions as described in the previous section. As one can see, the enthalpy density tends to zero when $|\mathbf{x}|$ becomes fairly large approaching the boundary surface defined by $|\mathbf{v}(t, \mathbf{x})| = 1$, in other words, when $\tilde{\tau} \rightarrow 0$. Thus the physically inconsistent situation when massive fluid elements move with the velocity of light at the surface $\tilde{\tau} = 0$ is avoided. Of course, in such a solution the constant pressure should vanish, $p_0 = 0$.

As it follows from the analysis of a behavior of the thermodynamic values in the previous section, the temperature is constant if $b_\epsilon = b_n$, otherwise one can choose the temperature approaching zero at the system's boundary, e.g., for EoS which is linear in temperature, the latter has the form

$$T = \text{const} \qquad b_\epsilon = b_n \quad (2.33)$$

$$T \sim e^{-(b_\epsilon^2 - b_n^2) \frac{t^2}{\tilde{\tau}^2}} \rightarrow 0, \quad |v(x)| \rightarrow 1 \quad b_\epsilon > b_n$$

according to (2.30).

Note that in the region of non-relativistic velocities, $v^2 = \sum \frac{a_i^2 x_i^2}{t^2} \ll 1$ the space distributions of the thermodynamical quantities (2.31),(2.32) have the Gaussian profile:

$$\begin{aligned} \varepsilon + p_0 &\simeq \frac{C_\epsilon}{\prod_i (t+T_i)} e^{-b_\epsilon^2 \sum a_i^2 \frac{x_i^2}{t^2}}, \\ n &\simeq \frac{C_n}{\prod_i (t+T_i)} e^{-b_n^2 \sum a_i^2 \frac{x_i^2}{t^2}} \end{aligned} \quad (2.34)$$

The forms of solutions (2.34) are similar to what was found in Ref. [30] as the elliptic solutions of the non-relativistic hydrodynamics equations. In this sense the solution proposed could be considered as the generalization (at vanishing pressure) of the corresponding non-relativistic solutions allowing one to describe relativistic expansion of the finite system into vacuum.

One can note that the case of *equal* flow parameters $T_i = 0$ and $b_\epsilon = b_n = 0$ induces formally Hubble-like velocity profile with the behavior of the density and enthalpy similar to (2.17) at $n=3$, $p = p_0$, and with the substitution $\tau \rightarrow t$.

The direct physical generalization of the Hubble solution for asymmetric case should be associated with the hypersurfaces of the pseudo-proper time $\tilde{\tau}$ rather than with time t , that eliminates the problem of infinite velocities: $v^2 = \sum \frac{a_i^2 x_i^2}{\tilde{t}^2} < 1$ at any hypersurface $\tilde{\tau}^2 = \text{const} > 0$. It can be reached if one chooses the functions F_ε and F_n in (2.25), (2.27) in the form

$$F \sim \left(\frac{t}{\tilde{\tau}} \right)^3. \quad (2.35)$$

Then the generalized Hubble solution is

$$\begin{aligned} u^\mu &= \left\{ \frac{t}{\tilde{\tau}}, \frac{a_1 x^1}{\tilde{\tau}}, \frac{a_2 x^2}{\tilde{\tau}}, \frac{a_3 x^3}{\tilde{\tau}} \right\}, \\ \varepsilon + p_0 &= C_\varepsilon \frac{a_1 a_2 a_3}{\tilde{\tau}^3}, \\ n &= C_n \frac{a_1 a_2 a_3}{\tilde{\tau}^3} \end{aligned} \quad (2.36)$$

where $\tilde{\tau} = \sqrt{t^2 - \sum a_i^2 x_i^2}$, $a_i \equiv a_i(t) = t/(t + T_i)$ and constants are: $C_\varepsilon = T_1 T_2 T_3 (\varepsilon(0, \mathbf{0}) + p_0)$, $C_n = T_1 T_2 T_3 n(0, \mathbf{0})$. Again, the proportionality between ε and n results in the temperature to be a constant during the evolution. If all parameters T_i are equal to each other, then a_i are also equal and solution (2.36) just corresponds to spherically symmetric Hubble flow (at constant pressure) and $\tilde{\tau}$ is the proper time of fluid element, $\tilde{\tau} = \tau$. Note that comparing to the standard representation of the Hubble solution the origin of a time scale is shifted, $t \rightarrow t + T_i$, and therefore the singularity at $t = 0$ is absent. Thus, if this solution is applied to a description of heavy ion collision, T_i should be interpreted as the initial proper time of thermalization and hydrodynamic expansion to which the origin of a time scale is shifted, typically $\tau_0 = T_i \simeq 1 \text{ fm}/c$. As to a general case of an asymmetric expansion, the *minimal* parameter T_i can be considered as the initial time t (at $\mathbf{x} = 0$) of the beginning of the hydrodynamic evolution. In analogy with the Hubble flow the initial conditions in asymmetric case (2.36) can be ascribed to the hypersurface $\sigma : \tilde{\tau} = \text{const}$ so that $t_\sigma(\mathbf{x} = 0) = 0$. Note, that such a hypersurface at $|\mathbf{x}| \rightarrow \infty$ tends to the hyperbolic hypersurface $\tau = \text{const}$ since $t_\sigma(\mathbf{x}) \rightarrow \infty$ in this limit and so all $a_i \rightarrow 1$.

The boost-invariant (1+1) solutions are also contained in general ellipsoidal solutions (2.25),(2.27) for quasi-inertial flow. To get it one has to choose functions F_ε and F_n in the form (2.35) with another power: $3 \rightarrow 1$; it leads to the same form of solution as (2.36) with replacement $\tilde{\tau}^3 \rightarrow \tilde{\tau}^1$. The next step is to suppress the transverse flow by setting $T_1 \rightarrow \infty, T_2 \rightarrow \infty$ (as usual, x_1 and x_2 denote coordinates in the transverse plane and x_3 is the longitudinal one), while the parameter T_3 is finite. This limit approach gives us $a_1 = a_2 = 0$ and $\tilde{\tau} \rightarrow \tau = \sqrt{(t + T_3)^2 - x_3^2}$

and results directly in the Bjorken solution at $T_3 = 0$. Since T_i is a shift of a time scale to the beginning of hydrodynamic expansion, it is natural to consider $T_3 \neq 0$ as this was discussed above for the Hubble-like solution. This value transforms as $T_3 \rightarrow T'_3 = T_3/\gamma$ at Lorentz boosts along axis x_3 .

Note, that if one does not change the power $3 \rightarrow 1$ in (2.35) and proceeds to the limit directly in the equation (2.36), the particle density (and enthalpy) behavior will differ from the boost-invariant one as the following:

$$n \sim \tau^{-1} \rightarrow n \sim \tau^{-1} \left(1 - \frac{x_3^2}{(t + T_3)^2} \right)^{-1} \quad (2.37)$$

It is also the solution of (1+1) relativistic hydrodynamics at $p = \text{const}$ but it obviously violates the boost-invariance: the particle and energy densities are not constant at any hypersurface and their analytic forms are changed in new coordinates after Lorentz boosts.

It is worthily to emphasize that the physical solutions with non-zero constant pressure have a limited region of applicability in time-like direction: if one wants to continue the solutions to asymptotically large times, then $(\epsilon + p_0)_{t \rightarrow \infty} \approx \frac{C}{t^3} \rightarrow 0$, and this results in non-physical asymptotical behavior $\epsilon \rightarrow -p_0$, unless we set $p_0 = 0$. Therefore, it is natural to utilize such kind of solutions in a region of the first order phase transition, characterized by the constant temperature and soft EoS, $c_s^2 = \partial p / \partial \epsilon \approx 0$, or at the final stage of the evolution that always corresponds to the quasi-inertial flows.

2.6 Conclusions

In this chapter, a general analysis of quasi-inertial flows in the relativistic hydrodynamics is done. The known analytical solutions, like the Hubble and Bjorken ones, are reproduced based on the developed approach. A new class of analytic solutions for 3D relativistic expansion with anisotropic flows is found. The ellipsoidal generalization of the spherically symmetric Hubble flow is considered within this class. These solutions can also describe the relativistic expansion of the finite systems into vacuum.

Specific equation of state makes the application to the whole hydrodynamic stage of evolution in heavy ion collisions to be problematic. However, the solutions can still be applicable during deconfinement phase transition and the final stage of evolution of hadron systems. Also, the solutions can serve as a test for numerical codes describing 3D asymmetric flows in the relativistic hydrodynamics.

Fast MC freeze-out generator

In this chapter the Monte-Carlo event generator, which simulates the final (freeze-out) stage of heavy ion collision, is presented. For comparison with other models and experimental data the results based on the standard parameterizations of the hadron freeze-out hypersurface and flow velocity profile are shown. Also, the hadron generation procedure is extended for the case of noncentral A+A collisions, and includes different chemical and thermal freeze-outs. In this event generator, we reach simultaneous description of single-particle p_T spectra for pions, kaons and protons and pion interferometry radii. The analysis of parameters, leading to such description, is important for building true dynamical models, like presented in the next chapters.

3.1 Introduction

Ongoing and planned experimental studies of relativistic heavy ion collisions in a wide range of beam energies require a development of new event generators and improvement of the existing ones [31]. Especially for Large Hadron Collider (LHC) experiments, because of very high hadron multiplicities, one needs fairly fast Monte-Carlo (MC) generators for event simulation.

A successful but oversimplified attempt of creating a fast hadron generator motivated by hydrodynamics was done in Ref. [32, 33, 34, 35]. The present work is an extension of this approach. We formulate a fast MC procedure to generate hadron multiplicities, four-momenta and four-coordinates for any kind of freeze-out hypersurface. Decays of hadronic resonances are taken into account. We consider hadrons consisting of light u, d and s quarks only, but the extension to heavier quarks is possible. The generator code is written in the object-oriented C++ language under the ROOT framework [36].

In this chapter we discuss both central and non-central collisions of nuclei using the Bjorken-like and Hubble-like freeze-out parameterizations used in so-called "blast wave" [37] and "Cracow" models [38], respectively. The same parameterizations have been used in the hadron generator referred as THERMINATOR [87] that appears however less efficient than our generator (see sections 3.2, 3.6).

This section is now organized as follows. Subsections 3.2-3.5 are devoted to the description of the physical framework of the model. In Subsection 3.6, the Monte Carlo simulation procedure is formulated. The validation of this procedure is presented in Subsection 3.7. In Subsection 3.8, the example calculations are compared with the Relativistic Heavy Ion Collider (RHIC) experimental data. The model extensions to non-central collisions and to different chemical and thermal freeze-outs are presented in Subsections 3.9, 3.10, with the results presented in 3.11. We summarize and conclude in Subsection 3.12.

3.2 Hadron multiplicities

We give here the basic formulae for the calculation of particle multiplicities. We consider the hadronic matter created in heavy-ion collisions as a hydrodynamically expanding fireball with the equation of state of an ideal hadron gas.

The mean number \bar{N}_i of particles species i crossing the *space-like* freeze-out hypersurface $\sigma(x)$ in Minkowski space can be computed as [39]

$$\bar{N}_i = \int_{\sigma(x)} d^3\sigma_\mu(x) j_i^\mu(x). \quad (3.1)$$

Here the four-vector $d^3\sigma_\mu(x) = n_\mu(x)d^3\sigma(x)$ is the element of the freeze-out hypersurface directed along the hypersurface normal unit four-vector $n^\mu(x)$ with a positively defined zero component ($n^0(x) > 0$) and $d^3\sigma(x) = |d^3\sigma_\mu d^3\sigma^\mu|^{1/2}$ is the invariant measure of this element. The normal to the space-like hypersurface is time-like, i.e. $n^\mu n_\mu = 1$; generally, for hypersurfaces including non-space-like sectors, the normal can also be a space-like so then $n^\mu n_\mu = -1$. The four-vector $j_i^\mu(x)$ is the current of particle species i determined as:

$$j_i^\mu(x) = \int \frac{d^3\vec{p}}{p^0} p^\mu f_i(x, p), \quad (3.2)$$

where $f_i(x, p)$ is the Lorentz invariant distribution function of particle freeze-out four-coordinate $x = \{x^0, \vec{x}\}$ and four-momentum $p = \{p^0, \vec{p}\}$. In the case of local equilibrium

$$f_i(x, p) = f_i^{\text{eq}}(p \cdot u(x); T(x), \mu(x)) = \frac{1}{(2\pi)^3} \frac{g_i}{\exp([p \cdot u(x) - \mu_i(x)]/T(x)) \pm 1}, \quad (3.3)$$

where $p \cdot u \equiv p^\mu u_\mu$, $g_i = 2J_i + 1$ is the spin degeneracy factor, $T(x)$ and $\mu_i(x)$ are the local temperature and chemical potential respectively, $u(x) = \gamma\{1, \vec{v}\}$ is the local collective four-velocity, $\gamma = (1 - v^2)^{-1/2}$, $u^\mu u_\mu = 1$. The signs \pm in the denominator account for the proper quantum statistics of a fermion or a boson, respectively.

The Lorentz scalar local particle density is defined as:

$$\rho_i(x) = u_\mu(x) j_i^\mu(x) = \int \frac{d^3 \vec{p}}{p^0} p_\mu u^\mu(x) f_i(x, p). \quad (3.4)$$

For a system in local thermal equilibrium, the particle density in the fluid element rest frame, where $u^{*\mu} = \{1, 0, 0, 0\}$, is solely determined by the local temperature $T(x^*)$ and chemical potential $\mu_i(x^*)$ for each particle species i :

$$\rho_i^{\text{eq}}(T(x^*), \mu_i(x^*)) = u_\mu^* j_i^{\text{eq}\mu}(x^*) = \int d^3 \vec{p}^* f_i^{\text{eq}}(p^{*0}; T(x^*), \mu_i(x^*)); \quad (3.5)$$

the four-vectors in fluid element rest frames are denoted by star.

In the case of local equilibrium, the particle current is proportional to the fluid element four-velocity: $j_i^{\text{eq}\mu}(x) = \rho_i^{\text{eq}}(T(x), \mu_i(x)) u^\mu(x)$. So the mean number of particles of species i is expressed directly through the equilibrated density:

$$\bar{N}_i = \int_{\sigma(x)} d^3 \sigma_\mu(x) u^\mu(x) \rho_i^{\text{eq}}(T(x), \mu_i(x)). \quad (3.6)$$

In the case of constant temperature and chemical potential, $T(x) = T$ and $\mu_i(x) = \mu_i$, one has

$$\bar{N}_i = \rho_i^{\text{eq}}(T, \mu_i) \int_{\sigma(x)} d^3 \sigma_\mu(x) u^\mu(x) = \rho_i^{\text{eq}}(T, \mu_i) V_{\text{eff}}, \quad (3.7)$$

i.e. the total yield of particle species i is determined by the freeze-out temperature T , chemical potential μ_i and by the total co-moving volume V_{eff} , so called *effective volume* of particle production which is a functional of the field of collective velocities $u^\mu(x)$ on the hypersurface $\sigma(x)$. The effective volume absorbs the collective velocity profile and the form of hypersurface and cancels out in all particle number ratios. Therefore, the particle number ratios do not depend on the freeze-out details as long as the local thermodynamic parameters are independent of x . The concept of the effective volume and factorization property similar to Eq. (3.7) has been considered first in Ref. [40], repeatedly used for the analysis of particle number ratios (see, e.g., Ref. [27]) and recently generalized for a study of the averaged phase space densities [41] and entropy [42]. One can apply this concept also in a limited rapidity window [40, 41, 42].

The concept of the effective volume can be applied to calculate the hadronic composition at both chemical and thermal freeze-outs [27]. At the former one, which happens soon after hadronization, the chemically equilibrated hadronic composition is assumed to be established and frozen in further evolution. The chemical potential μ_i for any particle species i at the chemical freeze-out is entirely determined by chemical potentials $\tilde{\mu}_q$ per a unit charge, i.e. per unit baryon number B , strangeness S , electric charge Q , charm C , etc. It can be expressed as a scalar product:

$$\mu_i = \vec{q}_i \vec{\mu}, \quad (3.8)$$

where $\vec{q}_i = \{B_i, S_i, Q_i, C_i, \dots\}$ and $\vec{\mu} = \{\tilde{\mu}_B, \tilde{\mu}_S, \tilde{\mu}_Q, \tilde{\mu}_C, \dots\}$. Assuming constant temperature and chemical potentials on the chemical freeze-out hypersurface, the total quantum numbers $\vec{q} = \{B, S, Q, C, \dots\}$ of the selected thermal part of produced hadronic system (e.g., in a rapidity interval near $y = 0$) with corresponding V_{eff} can be calculated as $\vec{q} = V_{\text{eff}} \sum_i \rho_i^{\text{eq}} \vec{q}_i$. For example:

$$B = V_{\text{eff}} \sum_{i=1}^n \rho_i^{\text{eq}}(T, \mu_i) B_i, \quad (3.9)$$

$$S = V_{\text{eff}} \sum_{i=1}^n \rho_i^{\text{eq}}(T, \mu_i) S_i, \quad (3.10)$$

$$Q = V_{\text{eff}} \sum_{i=1}^n \rho_i^{\text{eq}}(T, \mu_i) Q_i. \quad (3.11)$$

The potentials $\tilde{\mu}_q$ are not independent. Thus, taking into account baryon, strangeness and electrical charges only and fixing the total strangeness S and the total electric charge Q , $\tilde{\mu}_S$ and $\tilde{\mu}_Q$ can be expressed through baryonic potential $\tilde{\mu}_B$ using Eqs. (3.10) and (3.11). Therefore the mean numbers of each particle and resonance species at chemical freeze-out are determined solely by the temperature T and baryonic chemical potential $\tilde{\mu}_B$.

In practical calculations, we use the phenomenological observation [43] that particle yields in central Au+Au or Pb+Pb collisions in a wide center-of-mass energy range $\sqrt{s_{NN}} = 2.2 - 200$ GeV can be described within the thermal statistical approach using the following parametrizations of the temperature and baryon chemical potential [43]:

$$T(\tilde{\mu}_B) = a - b\tilde{\mu}_B^2 - c\tilde{\mu}_B^4, \quad (3.12)$$

$$\tilde{\mu}_B(\sqrt{s_{NN}}) = \frac{d}{1 + e\sqrt{s_{NN}}}, \quad (3.13)$$

$a = 0.166 \pm 0.002$ GeV, $b = 0.139 \pm 0.016$ GeV⁻¹, $c = 0.053 \pm 0.021$ GeV⁻³ and $d = 1.308 \pm 0.028$ GeV, $e = 0.273 \pm 0.008$ GeV⁻¹.

In practical calculations we determine all macroscopic characteristics of a particle system with the temperature T and chemical potentials μ_i via a set of equilibrium distribution functions in the fluid element rest frame:

$$f_i^{\text{eq}}(p^{*0}; T, \mu_i) = \frac{1}{(2\pi)^3} \frac{g_i}{\exp([p^{*0} - \mu_i]/T) \pm 1}. \quad (3.14)$$

Eq. (3.5) for the particle number density then reduces to

$$\rho_i^{\text{eq}}(T, \mu_i) = 4\pi \int_0^\infty dp^* p^{*2} f_i^{\text{eq}}(p^{*0}; T, \mu_i). \quad (3.15)$$

Using the expansion

$$f_i^{\text{eq}}(p^{*0}; T, \mu_i) = \frac{g_i}{(2\pi)^3} \sum_{k=1}^{\infty} (\mp)^{k+1} \exp\left(k \frac{\mu_i - p_i^{*0}}{T}\right), \quad (3.16)$$

the density can be represented in a form of a fast converging series:

$$\rho_i^{\text{eq}}(T, \mu_i) = \frac{g_i}{2\pi^2} m_i^2 T \sum_{k=1}^{\infty} \frac{(\mp)^{k+1}}{k} \exp\left(\frac{k\mu_i}{T}\right) K_2\left(\frac{km_i}{T}\right), \quad (3.17)$$

where K_2 is the modified Bessel function of the second order.

We assume that the calculated mean particle numbers $\bar{N}_i = \rho_i^{\text{eq}} V_{\text{eff}}$ correspond to a grand canonical ensemble. The probability that the ensemble consists of N_i particles is thus given by Poisson distribution:

$$P(N_i) = \exp(-\bar{N}_i) \frac{(\bar{N}_i)^{N_i}}{N_i!}. \quad (3.18)$$

3.3 Hadron momentum distributions

We suppose that a hydrodynamic expansion of the fireball ends by a sudden system breakup at given temperature and chemical potentials. In this case the momentum distribution of the produced hadrons keeps the thermal character of the equilibrium distribution (3.3). Similar to Eqs. (3.1), (3.2), this distribution is then calculated according to the Cooper-Frye formula [44]:

$$p^0 \frac{d^3 \bar{N}_i}{d^3 p} = \int_{\sigma(x)} d^3 \sigma_\mu(x) p^\mu f_i^{\text{eq}}(p \cdot u(x); T, \mu_i). \quad (3.19)$$

The integral in Eq. (3.19) can be calculated with the help of the invariant weight

$$W_{\sigma,i}(x,p) \equiv p^0 \frac{d^6 \bar{N}_i}{d^3 \sigma d^3 \vec{p}} = n_\mu(x) p^\mu f_i^{\text{eq}}(p \cdot u(x); T, \mu_i). \quad (3.20)$$

It is convenient to transform the four-vectors into the fluid element rest frame, e.g.,

$$\begin{aligned} n^{*0} &= n^\mu u_\mu = \gamma(n^0 - \vec{v}\vec{n}), \\ \vec{n}^* &= \vec{n} - \gamma(1 + \gamma)^{-1}(n^{*0} + n^0)\vec{v} \end{aligned} \quad (3.21)$$

and calculate the weight in this frame:

$$W_{\sigma,i}(x,p) = W_{\sigma,i}^*(x^*, p^*) = n_\mu^*(x) p^{*\mu} f_i^{\text{eq}}(p^{*0}; T, \mu_i). \quad (3.22)$$

Particularly, in the case when the normal four-vector $n^\mu(x)$ coincides with the fluid element flow velocity $u^\mu(x)$, i.e. $n^{*\mu} = u^{*\mu} = \{1, 0, 0, 0\}$, the weight $W_{\sigma,i}^*(x^*, p^*) = p^{*0} f_i^{\text{eq}}(p^{*0}; T, \mu)$ is independent of x and isotropic in the three-momentum \vec{p}^* . A simple and 100% efficient simulation procedure can then be realized in this frame and the four-momenta of the generated particles transformed back to the fireball rest frame using the velocity field $\vec{v}(x)$:

$$\begin{aligned} p^0 &= \gamma(p^{*0} + \vec{v}\vec{p}^*), \\ \vec{p} &= \vec{p}^* + \gamma(1 + \gamma)^{-1}(p^{*0} + p^0)\vec{v}. \end{aligned} \quad (3.23)$$

There are two well-known examples of the models giving $n^\mu(x) = u^\mu(x)$: the Bjorken model with hypersurface $\tau_B = (t^2 - z^2)^{1/2} = \text{const}$ and absent transverse flow and the model with hypersurface $\tau_H = (t^2 - x^2 - y^2 - z^2)^{1/2} = \text{const}$ and spherically symmetric Hubble flow. In general case $n_\mu(x)$ may differ from $u_\mu(x)$ and one should account for the $x-p$ correlation and the corresponding anisotropy due to the factor $n_\mu p^\mu$ even in the fluid element rest frame [45].

3.4 Generalization of the Cooper-Frye prescription

It is well known that the Cooper-Frye freeze-out prescription in Eq. (3.19) is not valid for the part of the freeze-out hypersurface characterized by a space-like normal four-vector n^μ . In this case $|n^0| < |\vec{n}|$ and so $p^\mu n_\mu < 0$ for some particle momenta thus leading to negative contributions to particle numbers. Usually, the negative contributions are simply rejected [46, 47]. This procedure however violates the continuity condition of the flow $\rho_i u^\mu n_\mu$ through the freeze-out hypersurface. Taking into account the continuity of the particle flow, the generalization

of Eq. (3.19) has the form [46]:

$$p^0 \frac{d^3 \bar{N}_i}{d^3 p} = \int_{\sigma(x)} d^3 \sigma_\mu(x) \pi^\mu(x, p) f_i^{\text{eq}}(T(x), \mu_i(x)), \quad (3.24)$$

where

$$\begin{aligned} \pi^\mu(x, p) &= p^\mu \theta(1 - |\tilde{\lambda}(x, p)|) + u^\mu(x) p \cdot u(x) \theta(|\tilde{\lambda}(x, p)| - 1), \\ \tilde{\lambda}(x, p) &= 1 - p \cdot n(x) [p \cdot u(x) n(x) \cdot u(x)]^{-1}, \end{aligned} \quad (3.25)$$

$\theta(x) = 1$ for $x \geq 0$, $\theta(x) = 0$ for $x < 0$.

Passing to the fluid element rest frames at each point x and using Lorentz transformation properties of the quantities in Eq. (3.24), one arrives at the same form of the four-vector of particle flow as in the case of the freeze-out hypersurface with the time-like normal $n^\mu(x)$:

$$j^\mu(x) = \int \frac{d^3 \vec{p}}{p_0} \pi^\mu(x, p) f_i^{\text{eq}}(T(x), \mu_i(x)) = \rho_i^{\text{eq}}(T(x), \mu_i(x)) u^\mu(x). \quad (3.26)$$

Therefore the factorization of the freeze-out details in the effective volume in the case of constant temperature and chemical potentials, i.e. Eq. (3.7), is valid for any type of hypersurface [41]. It follows from Eqs. (3.24), (3.25) that the invariant weight in the fluid element rest frame has then the form:

$$\begin{aligned} W_{\sigma, i}^*(x^*, p^*) &= \left[p^{*\mu} n_\mu^* \theta \left(1 - \left| \frac{\vec{p}^* \vec{n}^*}{p^{*0} n^{*0}} \right| \right) + p^{*0} n^{*0} \theta \left(\left| \frac{\vec{p}^* \vec{n}^*}{p^{*0} n^{*0}} \right| - 1 \right) \right] \times \\ &\times f_i^{\text{eq}}(p^{*0}; T, \mu_i). \end{aligned} \quad (3.27)$$

For the time-like normal $n^\mu(x)$, Eq. (3.27) reduces to Eq. (3.22).

It is worth noting that though the bulk of particles is likely associated with the volume decay, the particle emission from the surface of expanding system, or formally, from a non-space-like part of the freeze-out hypersurface enclosed in Minkowski space, is essential for a description of hadronic spectra and like pion correlations at relatively large p_T [48].

3.5 Freeze-out surface parameterizations

In principle, one can specify the fireball initial conditions (e.g., Landau- or Bjorken-like) and equation of state to follow the fireball dynamic evolution until the freeze-out stage with the help of relativistic hydrodynamics. The corresponding freeze-out four-coordinates x^μ , the hypersurface normal four-vectors $n^\mu(x)$ and the collective flow four-velocities $u^\mu(x)$ can then be used to calculate particle spectra according

to generalized Cooper-Frye prescription. This possibility is foreseen as an option in our MC generator. In this work, we however do not consider the fireball evolution, we demonstrate our fast MC procedure utilizing the simple and frequently used parametrizations of the freeze-out.

At relativistic energies, due to dominant longitudinal motion, it is convenient to substitute the Cartesian coordinates t, z by the Bjorken ones

$$\tau = (t^2 - z^2)^{1/2}, \quad \eta = \frac{1}{2} \ln \frac{t+z}{t-z} \quad (3.28)$$

and introduce the the radial vector $\vec{r} \equiv \{x, y\} = \{r \cos \phi, r \sin \phi\}$, i.e.:

$$x^\mu = \{\tau \cosh \eta, \vec{r}, \tau \sinh \eta\} = \{\tau \cosh \eta, r \cos \phi, r \sin \phi, \tau \sinh \eta\}. \quad (3.29)$$

Similarly, it is convenient to parameterize the fluid flow four-velocity $u^\mu(x) = \gamma(x)\{1, \vec{v}(x)\} \equiv \gamma(x)\{1, \vec{v}_r(x), v_z(x)\}$ at a point x in terms of the longitudinal (z) and transverse (r) fluid flow rapidities

$$\eta_u(x) = \frac{1}{2} \ln \frac{1 + v_z(x)}{1 - v_z(x)}, \quad \rho_u(x) = \frac{1}{2} \ln \frac{1 + v_r(x) \cosh \eta_u(x)}{1 - v_r(x) \cosh \eta_u(x)}, \quad (3.30)$$

where $v_r = |\vec{v}_r|$ is the magnitude of the transverse component of the flow three-velocity $\vec{v} = \{v_r \cos \phi_u, v_r \sin \phi_u, v_z\}$, i.e.

$$u^\mu(x) = \{\cosh \rho_u \cosh \eta_u, \sinh \rho_u \cos \phi_u, \sinh \rho_u \sin \phi_u, \cosh \rho_u \sinh \eta_u\} \\ = \{(1 + u_r^2)^{1/2} \cosh \eta_u, \vec{u}_r, (1 + u_r^2)^{1/2} \sinh \eta_u\}, \quad (3.31)$$

$\vec{u}_r = \gamma \vec{v}_r = \gamma_r \cosh \eta_u \vec{v}_r$, $\gamma_r = \cosh \rho_u$. For the considered central collisions of symmetric nuclei, $\phi_u = \phi$. Representing the freeze-out hypersurface by the equation $\tau = \tau(\eta, r, \phi)$, the hypersurface element in terms of the coordinates η, r, ϕ becomes

$$d^3 \sigma_\mu = \epsilon_{\mu\alpha\beta\gamma} \frac{dx^\alpha dx^\beta dx^\gamma}{d\eta dr d\phi} d\eta dr d\phi, \quad (3.32)$$

where $\epsilon_{\mu\alpha\beta\gamma}$ is the completely antisymmetric Levy-Civita tensor in four dimensions with $\epsilon^{0123} = -\epsilon_{0123} = 1$. Particularly, for azimuthally symmetric hypersurface $\tau = \tau(\eta, r)$, Eq. (3.51) yields [27]:

$$d^3 \sigma_\mu = \tau(\vec{r}, \eta) d^2 \vec{r} d\eta \times \\ \times \left\{ \frac{1}{\tau} \frac{d\tau}{d\eta} \sinh \eta + \cosh \eta, -\frac{d\tau}{dr} \cos \phi, -\frac{d\tau}{dr} \sin \phi, -\frac{1}{\tau} \frac{d\tau}{d\eta} \cosh \eta - \sinh \eta \right\}. \quad (3.33)$$

Generally, the freeze-out hypersurface is represented by a set of equations $\tau = \tau_j(\eta, r, \phi)$ and Eq. (3.51) should be substituted by the sum of the corresponding hypersurface elements.

To simplify the situation, besides the azimuthal symmetry, we further assume the longitudinal boost invariance [49]. The local quantities (such as particle density) are then functions of τ and r only. The hypersurface then takes the form $\tau = \tau(r)$, the flow rapidities $\eta_u = \eta$ (i.e. $v_z = z/t$), $\rho_u = \rho_u(r)$ and Eq. (3.33) yields

$$\begin{aligned} d^3\sigma_\mu &= \tau(r)d^2\vec{r}d\eta\{\cosh\eta, -\frac{d\tau}{dr}\cos\phi, -\frac{d\tau}{dr}\sin\phi, -\sinh\eta\}, \\ d^3\sigma &= |1 - (\frac{d\tau}{dr})^2|^{1/2}\tau(r)d^2\vec{r}d\eta, \\ n^\mu(x) &= |1 - (\frac{d\tau}{dr})^2|^{-1/2}\{\cosh\eta, \frac{d\tau}{dr}\cos\phi, \frac{d\tau}{dr}\sin\phi, \sinh\eta\}. \end{aligned} \quad (3.34)$$

Note that the normal four-vector n^μ becomes space-like ($n^\mu n_\mu = -1$) for $|d\tau/dr| > 1$.

For the simplest freeze-out hypersurface $\tau = \text{const}$ one has

$$\begin{aligned} d^3\sigma &= \tau d^2\vec{r}d\eta, \\ n^\mu(x) &= \{\cosh\eta, 0, 0, \sinh\eta\}. \end{aligned} \quad (3.35)$$

In this case the normal $n^\mu(x)$ is time-like ($n^\mu n_\mu = 1$) but generally different from the flow four-velocity $u^\mu(x)$ except for the case of absent transverse flow (i.e. $\rho_u = 0$). Assuming $\phi_u = \phi$ and the linear transverse flow rapidity profile (effectively taking into account a positive flow - radius correlation up to the radii close to the fireball boundary as indicated by numerical solutions of (3+1)-dimensional relativistic hydrodynamics, see, e.g., [50]):

$$\rho_u = \frac{r}{R}\rho_u^{\max}, \quad (3.36)$$

where R is the fireball transverse radius, the total effective volume for particle production at $\tau = \text{const}$ is

$$\begin{aligned} V_{\text{eff}} &= \int_{\sigma(x)} d^3\sigma_\mu(x)u^\mu(x) = \tau \int_0^R \gamma_r r dr \int_0^{2\pi} d\phi \int_{\eta_{\min}}^{\eta_{\max}} d\eta = \\ &= 2\pi\tau\Delta\eta \left(\frac{R}{\rho_u^{\max}}\right)^2 (\rho_u^{\max}\sinh\rho_u^{\max} - \cosh\rho_u^{\max} + 1), \end{aligned} \quad (3.37)$$

where $\Delta\eta = \eta_{\max} - \eta_{\min}$. For small values of the maximal transverse flow rapidity ρ_u^{\max} , Eq. (3.37) reduces to $V_{\text{eff}} = \pi\tau R^2\Delta\eta$ [27].

We shall refer the above choice of the freeze-out hyper-surface and the flow four-velocity profile as the Bjorken-like parametrization or Bjorken model scenario for particle freeze-out with transverse flows [49].

We also consider so called Cracow model scenario [38] corresponding to the Hubble-like freeze-out hypersurface $\tau_H = (t^2 - x^2 - y^2 - z^2)^{1/2} = \text{const}$ and flow four-velocity

$$u^\mu(x) = x^\mu/\tau_H. \quad (3.38)$$

Introducing the longitudinal space-time rapidity η according to Eq. (3.49) and the transverse space-time rapidity $\rho = \sinh^{-1}(r/\tau_H)$, one has [51]

$$x^\mu = \tau_H \{ \cosh \eta \cosh \rho, \sinh \rho \cos \phi, \sinh \rho \sin \phi, \sinh \eta \cosh \rho \}, \quad (3.39)$$

$\tau_H = \tau_B / \cosh \rho$. Representing the freeze-out hypersurface by the equation $\tau_H = \tau_H(\eta, \rho, \phi) = \text{const}$, one finds from Eq. (3.51):

$$d^3 \sigma = \tau_H^3 \sinh \rho \cosh \rho d\eta d\rho d\phi = \tau_H d\eta d^2 \vec{r}, \quad (3.40)$$

$$n^\mu(x) = u^\mu(x).$$

The effective volume corresponding to $r = \tau_H \sinh \rho < R$ and $\eta_{\min} \leq \eta \leq \eta_{\max}$ is

$$V_{\text{eff}} = \int_{\sigma(x)} d^3 \sigma_\mu(x) u^\mu(x) = \tau_H \int_0^R r dr \int_0^{2\pi} d\phi \int_{\eta_{\min}}^{\eta_{\max}} d\eta = \pi \tau_H R^2 \Delta\eta. \quad (3.41)$$

3.6 Hadron generation procedure

Our MC procedure to generate the freeze-out hadron multiplicities, four-momenta and four-coordinates is the following:

1. First, the parameters of the chosen freeze-out model are initialized. Particularly, for the models with constant freeze-out temperature T and chemical potentials μ_i , the phenomenological formulae (3.12), (3.13) are implemented as an option allowing to calculate T and μ_i at the chemical freeze-out in central $Au + Au$ or $Pb + Pb$ collisions specifying only the center-of-mass energy $\sqrt{s_{NN}}$. In the scenario with the thermal freeze-out occurring at a temperature $T^{\text{th}} < T^{\text{ch}}$, the chemical potentials μ_i^{th} are no more given by Eq. (3.8). At given thermal freeze-out temperature T^{th} and effective volume $V_{\text{eff}}^{\text{th}}$, they are set according to the procedure described in section 3.2. So far, only the stable particles and resonances consisting of u , d , s quarks are incorporated in the model. They are taken from the ROOT particle data table [36, 52].
2. Next, the effective volume corresponding to a given freeze-out model is determined, e.g., according to Eq. (3.68) or (3.73) and particle number densities are calculated with the help of Eq. (3.75). The mean multiplicity of each particle species is then calculated according to Eq. (3.7). A more general option to calculate the mean multiplicities, e.g., in the case of the freeze-out hypersurface obtained from relativistic hydrodynamics, is the direct integration of Eq. (3.24). The multiplicity corresponding to the mean one is simulated according to Poisson distribution in Eq. (3.76).

3. The particle freeze-out four-coordinates $x^\mu = \{\tau \cosh \eta, r \cos \phi, r \sin \phi, \tau \sinh \eta\}$ in the fireball rest frame are then simulated on each hypersurface segment $\tau = \tau_j(r)$ according to the element $d^3\sigma_\mu u^\mu = d^3\sigma_0^* = n_0^*(r)|1-(d\tau/dr)^2|^{1/2}\tau(r)d^2\vec{r}d\eta$, assuming n_0^* and τ functions of r (i.e. independent of η, ϕ), by sampling uniformly distributed η in the interval $[\eta_{\min}, \eta_{\max}]$, ϕ in the interval $[0, 2\pi]$ and generating r in the interval $[0, R]$ using a 100% efficient procedure similar to ROOT routine *GetRandom()*. In the Bjorken- and Hubble-like models: $\tau(r) = \tau_B = \text{const}$, $n_0^* = \cosh \rho_u = \gamma_r$ and $|1-(d\tau/dr)^2|^{1/2}\tau(r) = \tau_H = \text{const}$, $n_0^* = 1$, respectively. Note that if n_0^* and τ were depending on two or three variables, a generalization of the routine *GetRandom()* to more dimensions is possible. A less efficient possibility is to simulate \vec{r}, η according to the element $d^2\vec{r}d\eta$ and include the factor $d^3\sigma n_0^*/d^2\vec{r}d\eta$ in the residual weight in the step 6. Also note that the particle freeze-out coordinates calculated from relativistic hydrodynamics are distributed according to the element $d^3\sigma_\mu u^\mu$.
4. The corresponding collective flow four-velocities $u^\mu(x)$ are calculated using, e.g., Eqs. (3.59), (3.36) or Eq. (3.38).
5. The particle three-momenta $p^*\{\sin \theta \cos \phi, \sin \theta \sin \phi, \cos \theta\}$ are then generated in the fluid element rest frames according to the probability $f_i^{\text{eq}}(p^{0*}; T, \mu_i)p^{*2}dp^*d\cos\theta_p^*d\phi_p^*$ by sampling uniformly distributed $\cos\theta_p^*$ in the interval $[-1, 1]$, ϕ_p^* in the interval $[0, 2\pi]$ and generating p^* using a 100% efficient procedure similar to ROOT routine *GetRandom()*.
6. Next, the standard von Neumann rejection/acceptance procedure is used to account for the difference between the true probability $W_{\sigma,i}^*d^3\sigma d^3\vec{p}^*/p^{0*}$ (see Eqs. (3.20), (3.22), (3.27)) and the probability $f_i^{\text{eq}}(p^{0*}; T, \mu_i)d^3\sigma_\mu u^\mu d^3\vec{p}^* = f_i^{\text{eq}}(p^{0*}; T, \mu_i)n^{0*}d^3\sigma d^3\vec{p}^*$ corresponding to the simulation steps 3-5. Thus the residual weight

$$W_i^{\text{res}} = \frac{W_{\sigma,i}^*d^3\sigma d^3\vec{p}^*}{n^{0*}p^{0*}f_i^{\text{eq}}d^3\sigma d^3\vec{p}^*} \quad (3.42)$$

is calculated and the simulated particle four-coordinate and four-momentum are accepted provided that this weight is larger than a test variable randomly simulated in the interval $[0, \max(W_i^{\text{res}})]$. Otherwise, the simulation returns to step 3. Note that for the freeze-out parametrizations considered in this work,

$$W_i^{\text{res}} = \left(1 - \frac{\vec{n}^* \vec{p}^*}{n^{0*}p^{0*}}\right) \quad (3.43)$$

and the maximal weight $\max(W_i^{\text{res}})$ can be calculated analytically. Particularly, in the Bjorken-like model and $\eta^{\text{max}} \gg 1$, W_i^{res} is distributed in the interval $[1 - \tanh \rho_u^{\text{max}}, 1 + \tanh \rho_u^{\text{max}}]$. The step 6 can be omitted for the

Hubble-like model or for the Bjorken model without transverse flow ($\rho_u = 0$) when $W_i^{\text{res}} = 1$. Generally, in the residual weight one should take into account the contribution of non-space-like sectors of the freeze-out hypersurface:

$$W_i^{\text{res}} = \left[\left(1 - \frac{\vec{n}^* \vec{p}^*}{n^{0*} p^{0*}} \right) \theta \left(1 - \left| \frac{\vec{p}^* \vec{n}^*}{p^{*0} n^{*0}} \right| \right) + \theta \left(\left| \frac{\vec{p}^* \vec{n}^*}{p^{*0} n^{*0}} \right| - 1 \right) \right] \quad (3.44)$$

7. Next, the hadron four-momentum $p^{*\mu}$ is boosted to the fireball rest frame according to Eqs. (3.23).
8. The two-body, three-body and many-body decays are simulated with the branching ratios calculated via ROOT utilities [36]. A more correct kinetic evolution, taking into account not only resonance decays but also hadron elastic scattering, may be included with the help of the Boltzmann equation solver C++ code which was developed earlier [53].

It should be stressed that a high generation speed is achieved due to 100% generation efficiency of the freeze-out four-coordinates and four-momenta in steps 3-5 as well as due to a weak non-uniformity of the residual weight W_i^{res} in the cases of practical interest. For example, in the Bjorken-like model, the increase of the maximal transverse flow rapidity from zero ($W_i^{\text{res}} = \text{const}$) to $\rho_u^{\text{max}} = 0.65$ leads only to a few percent decrease of the generation speed. Compared, e.g., to THERMINATOR [87], our generator appears more than one order of magnitude faster.

3.7 Validation of the MC procedure

In the Boltzmann approximation for the equilibrium distribution function (3.14), i.e. retaining only the first term in the expansion (3.16), the transverse momentum (p_t) spectrum in the Bjorken-like model takes the form [32, 11]:

$$\frac{d\bar{N}_i}{p_t dp_t} = \frac{1}{\pi} g_i \tau m_t e^{\mu_i/T} \Delta\eta \int_0^R r dr K_1 \left(\frac{m_t \cosh \rho_u}{T} \right) I_0 \left(\frac{p_t \sinh \rho_u}{T} \right) \quad (3.45)$$

where $I_0(z)$ and $K_1(z)$ are the modified Bessel functions and $m_t = (m_i^2 + p_t^2)^{1/2}$ is the particle transverse mass.

To test our MC procedure, we compare in Fig. 3.1 the transverse momentum spectrum calculated according to Eq. (3.45) with the corresponding MC result for $T = 0.165$ GeV, $R = 8$ fm, $m_i = 0.14$ GeV, $\Delta\eta = 10$, $\mu = 0.0$ GeV, $\tau = 12$ fm/c, $\rho_u^{\text{max}} = 0.65$ and 2.0. One may see that the analytical and the MC calculations practically coincide.

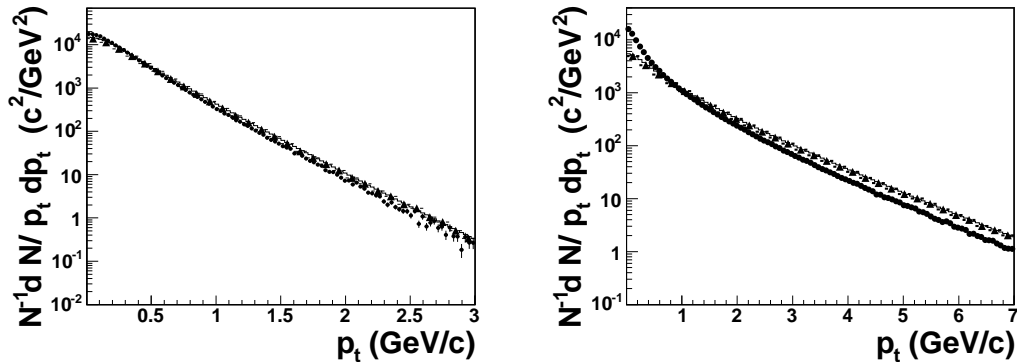


Figure 3.1: The validation of the MC procedure for $\rho_u^{\max} = 0.65$ (left panel) and 2.0 (right panel): the transverse momentum spectra (solid lines) calculated according to Eq. (3.45) and the corresponding MC results (black triangles). Also shown are the MC results obtained with a constant residual weight (black points).

To demonstrate the increasing influence of the residual weight with the increasing ρ_u^{\max} , we also present in Fig. 3.1 the MC results obtained without this weight.

3.8 Input parameters and results

We present here the results of example MC calculations performed on the assumption of a common chemical and thermal freeze-out and compare them with the experimental data on central Au + Au collisions at RHIC.

Model input parameters

First, we summarize the input parameters which control the execution of our MC hadron generator in the case of Bjorken-like and Hubble-like parametrizations with a common thermal and chemical freeze-out:

1. Number of events to generate.
2. Thermodynamic parameters at chemical freeze-out: temperature (T) and chemical potentials per a unit charge ($\tilde{\mu}_B, \tilde{\mu}_S, \tilde{\mu}_Q$). As an option, there is an additional parameter $\gamma_s \leq 1$ taking into account the strangeness suppression

Table 3.1: The model parameters for central Au + Au collisions at $\sqrt{s_{NN}} = 200$ GeV.

parameter	Bjorken-like	Hubble-like
T , GeV	0.165	0.165
$\tilde{\mu}_B$, GeV	0.028	0.028
$\tilde{\mu}_S$, GeV	0.007	0.007
$\tilde{\mu}_Q$, GeV	-0.001	-0.001
γ_s	1 (0.8)	1 (0.8)
τ , fm/c	6.1	9.65
R , fm	10.0	8.2
η_{\max}	2 (3,5)	2 (3,5)
ρ_u^{\max}	0.65	-

according to partially equilibrated distribution [54, 55]:

$$f_i(p^{*0}; T, \mu_i, \gamma_s) = \frac{g_i}{\gamma_s^{-n_i^s} \exp([p^{*0} - \mu_i]/T) \pm 1}, \quad (3.46)$$

where n_i^s is the number of strange quarks and anti-quarks in a hadron i . Optionally, the parameter γ_s can be fixed using its phenomenological dependence on the temperature and baryon chemical potential [56].

3. Volume parameters: the freeze-out proper time (τ) and fireball transverse radius (R).
4. Maximal transverse flow rapidity (ρ_u^{\max}) for Bjorken-like parametrization [32, 33].
5. Maximal space-time longitudinal rapidity (η_{\max}) which determines the rapidity interval $[-\eta_{\max}, \eta_{\max}]$ in the collision center-of-mass system. To account for the violation of the boost invariance, we have included in the code an option corresponding to the substitution of the uniform distribution of the space-time longitudinal rapidity η in the interval $[-\eta_{\max}, \eta_{\max}]$ by a Gaussian distribution $\exp(-\eta^2/2\Delta\eta^2)$ with a width parameter $\Delta\eta$ (see, e.g., [57]).

The parameters used to model central Au+Au collisions at $\sqrt{s_{NN}} = 200$ GeV are given in Table 3.1.

Space-time distributions of the hadron emission points

In figures 3.2 and 3.3, we show the distributions of the π^+ emission transverse x-coordinate and time generated in the Bjorken-like and Hubble-like models with

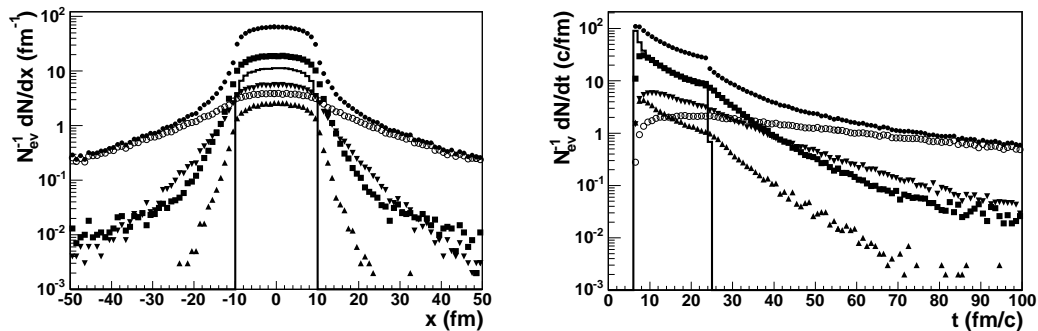


Figure 3.2: The π^+ emission transverse x -coordinate (left) and time (right) generated in the Bjorken-like model with the parameters given in Table 3.1, $\eta_{\max} = 2$: all π^+ 's (solid circles), direct π^+ 's (solid line), decay π^+ 's from ρ (squares), ω (open circles), $K^*(892)$ (up-triangles) and Δ (down-triangles).

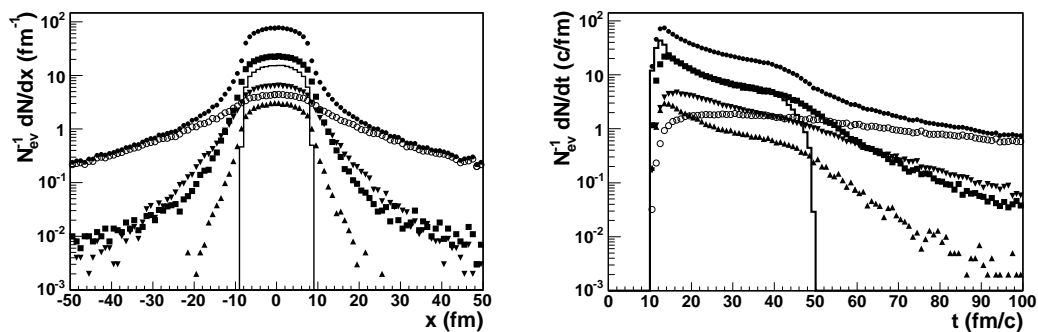


Figure 3.3: The same as in Fig. 3.2 for the Hubble-like parametrization.

the parameters given in Table 3.1, $\eta_{\max} = 2$. Also shown are the contributions from the primary π^+ 's emitted directly from the freeze-out hypersurface and the contributions from π^+ 's from the decays of the most abundant resonances ρ , ω , $K^*(892)$ and Δ . For primary pions, $x < R$ and $\tau < t < \tau \cosh \eta_{\max}$. The tails at $|x| > R$ and $t > \tau \cosh \eta_{\max}$ reflect the exponential law of the resonance decays. The longest tails in figures 3.2 and 3.3 are due to pions from ω decays.

Ratios of hadron abundances

It is well known that the particle abundances in heavy-ion collisions in a large energy range can be reasonably well described within statistical models (see, e.g.,

Table 3.2: Particle number ratios near mid-rapidity in central Au + Au collisions at $\sqrt{s_{NN}} = 130$ GeV calculated with the thermodynamic parameters: $T = 0.168$ GeV, $\tilde{\mu}_B = 0.041$ GeV, $\tilde{\mu}_S = 0.010$ GeV and $\tilde{\mu}_Q = -0.001$ GeV.

ratios	our MC	statistical model [60]	experiment
π^-/π^+	0.98	1.02	1.00 ± 0.02 [61], 0.99 ± 0.02 [62]
\bar{p}/π^-	0.06	0.09	0.08 ± 0.01 [63]
K^-/K^+	0.90	0.92	0.91 ± 0.09 [61], 0.93 ± 0.07 [64]
K^-/π^-	0.22	0.16	0.15 ± 0.02 [65]
\bar{p}/p	0.61	0.65	0.60 ± 0.07 [61], 0.64 ± 0.08 [64]
Λ/Λ	0.69	0.69	0.71 ± 0.04 [66]
Ξ/Ξ	0.79	0.77	0.83 ± 0.06 [66]
ϕ/K^-	0.17	0.15	0.13 ± 0.03 [67]
Λ/p	0.48	0.47	0.49 ± 0.03 [68], [69]
Ξ^-/π^-	0.0086	0.0072	0.0088 ± 0.0020 [70]

Table 3.3: Particle number ratios near mid-rapidity in central Au + Au collisions at $\sqrt{s_{NN}} = 200$ GeV calculated with the thermodynamic parameters: $T = 0.165$ GeV, $\tilde{\mu}_B = 0.028$ GeV, $\tilde{\mu}_S = 0.07$ GeV, and $\tilde{\mu}_Q = -0.001$ GeV.

particle number ratios	our MC	experiment [72]
π^-/π^+	0.98	0.984 ± 0.004
K^-/K^+	0.94	0.933 ± 0.008
K^-/π^-	0.21	0.162 ± 0.001
\bar{p}/p	0.71	0.731 ± 0.011

[59, 54, 58]) based on the assumption that the produced hadronic matter reaches thermal and chemical equilibrium. This is demonstrated in tables 3.2 and 3.3 for the particle number ratios near mid-rapidity in central Au + Au collisions at $\sqrt{s_{NN}} = 130$ and 200 GeV calculated in our MC model and the statistical model of Ref. [60] and compared with the RHIC experimental data. Being independent of volume and flow parameters, the particle number ratio allow one to fix the thermodynamic parameters. We have not tuned the latter here and simply used the same thermodynamic parameters as in Ref. [60] despite there are noticeable differences in some particle number ratios calculated in the two models. These differences may be related to the different numbers of resonance states taken into account and uncertainties in the decay modes of high excited resonances.

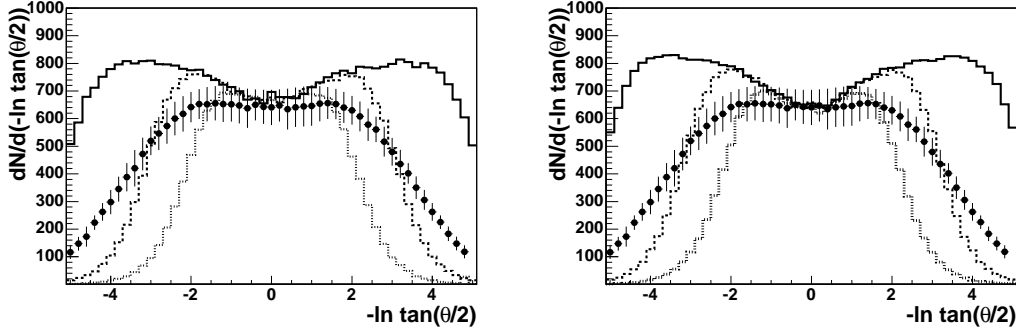


Figure 3.4: The pseudo-rapidity ($-\ln \tan(\theta/2)$, θ is the particle production angle) distributions of charged particles in central Au + Au collisions at $\sqrt{s_{NN}} = 200$ GeV from the PHOBOS experiment [71] (solid circles) and the MC calculations within the Bjorken-like (left panel) and Hubble-like (right panel) models. The model results corresponding to the space-time rapidity range parameter $\eta_{\max} = 5, 3$ and 2 are shown by solid, dashed and dotted lines respectively.

Pseudo-rapidity distributions

In Fig. 3.4, we compare the PHOBOS data [71] on pseudo-rapidity spectrum of charged hadrons in central Au+Au collisions at $\sqrt{s_{NN}} = 200$ GeV with our MC results obtained within the Bjorken-like and Hubble-like models for different values of η_{\max} . One may see that the data are compatible with the longitudinal boost invariance only in the mid-rapidity region in which the model is practically insensitive to η_{\max} . In the single freeze-out scenario, the data on particle numbers at mid-rapidity thus allows one to fix the effective volume $V_{\text{eff}} \propto \tau R^2$.

Transverse momentum spectra

In Fig. 3.5, we compare the mid-rapidity PHENIX data [72] on π^+ , K^+ and proton p_t spectra in Au+Au collisions at $\sqrt{s_{NN}} = 200$ GeV with our MC results obtained within the Bjorken-like and Hubble-like models. A good agreement between the models and the data may be seen for pions while for kaons and protons the models overestimate the spectra at $p_t < 1$ GeV/c. For kaons, this discrepancy can be diminished with the help of the strangeness suppression parameter γ_s of 0.8 (see the right panel in Fig. 3.5). The overestimated slope of the kaon and proton p_t spectra can also be related with the oversimplified assumption of a common thermal and chemical freeze-out or insufficient number of the accounted heavy resonance states.

The contribution of different resonances to the pion p_t spectrum calculated in

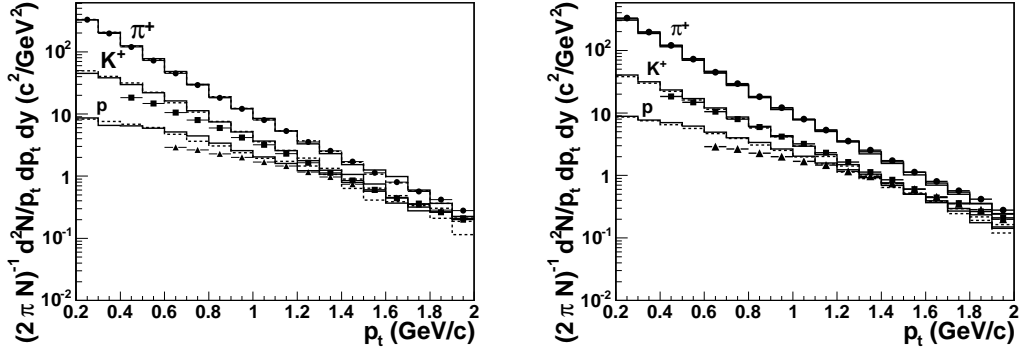


Figure 3.5: The π^+ , K^+ and proton transverse momentum spectra at mid-rapidity $y \approx 0$ in central Au + Au collisions at $\sqrt{s_{NN}} = 200$ GeV from PHENIX experiment [72] (solid symbols) and the MC calculations within the Bjorken-like (dashed lines) and Hubble-like (solid lines) models. The right panel shows the model results obtained with the strangeness suppression parameter $\gamma_s = 0.8$.

the Bjorken-like model is shown in Fig. 3.6.

Note that in Hubble-like model, the transverse flow is determined by the volume parameters R, τ and so, at fixed thermodynamic parameters and the effective volume $V_{\text{eff}} \propto \tau R^2$, the transverse momentum spectra allow one to fix both R and τ . In the Bjorken-like model, there is more freedom since the transverse flow is also regulated by the parameter ρ_u^{max} . The choice of these parameters in Table 3.1 has been done to minimize the discrepancy of the simulated and measured correlation radii of identical pions (see below).

Correlation functions

It is well known that, due to the effects of quantum statistics (QS) and final state interaction (FSI), the momentum correlations of two or more particles at small relative momenta in their center-of-mass system are sensitive to the space-time characteristics of the production process on a level of $\text{fm} = 10^{-15}$ m so serving as a correlation femtoscopy tool (see, for example, [73]-[77]).

The momentum correlations are usually studied with the help of correlation functions of two or more particles. Particularly, the two-particle correlation function $CF(p_1, p_2)$ is defined as a ratio of the measured two-particle distribution to the reference one which is usually constructed by mixing the particles from different events of a given class, normalizing the correlation function to unity at sufficiently large relative momenta.

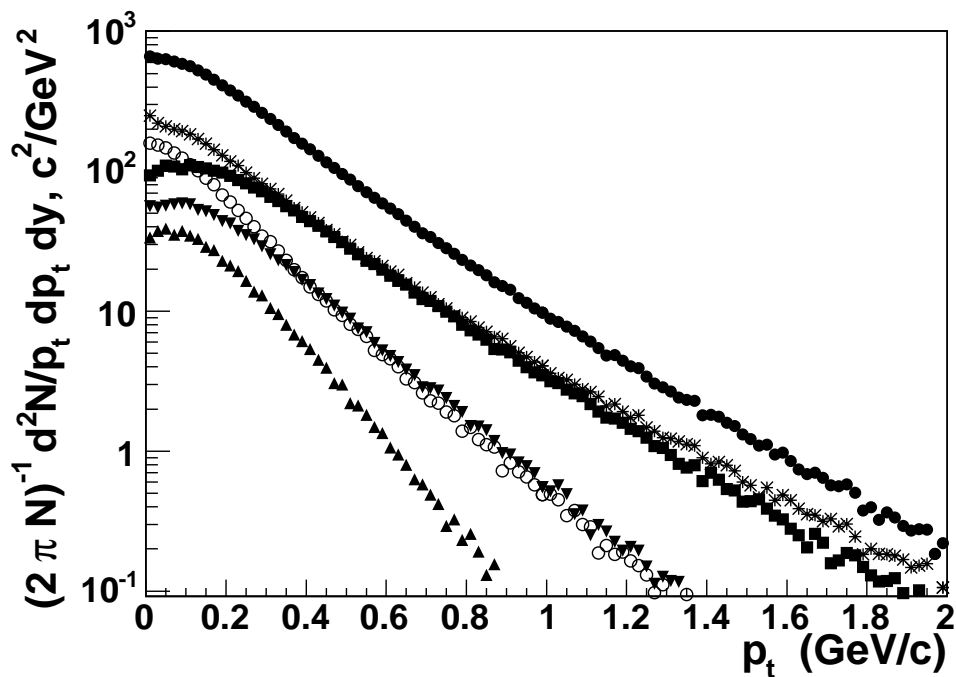


Figure 3.6: The contributions to the π^+ transverse momentum spectrum at mid-rapidity in central Au + Au collisions at $\sqrt{s_{NN}} = 200$ GeV calculated within the Bjorken-like model: all π^+ 's (solid circles), direct π^+ 's (stars), decay π^+ 's from ρ (squares), ω (open circles), $K^*(892)$ (up-triangles) and Δ (down-triangles).

Since our MC generator provides the information on particle four-momenta p_i and four-coordinates x_i of the emission points, it can be used to calculate the correlation function with the help of the weight procedure, assigning a weight to a given particle combination accounting for the effects of QS and FSI. Here we will consider the correlation function of two identical pions neglecting their FSI, so the weight

$$w = 1 + \cos(q \cdot \Delta x), \quad (3.47)$$

where $q = p_1 - p_2$ and $\Delta x = x_1 - x_2$. The CF is defined as a ratio of the weighted histogram of the pair kinematic variables to the unweighted one.

Generally, the pair is characterized by six kinematic variables. In case of the azimuthal symmetry, there are five variables that are usually chosen as the three "out-side-long" components of the relative three-momentum vector [74, 75] $\mathbf{q} = (q_{\text{out}}, q_{\text{side}}, q_{\text{long}})$, half the pair transverse momentum k_t and the pair rapidity or pseudo-rapidity. The out and side denote the transverse, with respect to the reaction axis, components of the vector \mathbf{q} ; the out direction is parallel to the transverse component of the pair three-momentum.

The corresponding correlation widths are usually parameterized in terms of the Gaussian correlation radii R_i ,

$$\begin{aligned} CF(p_1, p_2) = \\ = 1 + \lambda \exp(-R_{\text{out}}^2 q_{\text{out}}^2 - R_{\text{side}}^2 q_{\text{side}}^2 - R_{\text{long}}^2 q_{\text{long}}^2 - 2R_{\text{out, long}}^2 q_{\text{out}} q_{\text{long}}) \end{aligned} \quad (3.48)$$

and their dependence on pair rapidity and transverse momentum is studied. The form of Eq. (3.81) assumes azimuthal symmetry of the production process [74]. Generally, e.g., in case of the correlation analysis with respect to the reaction plane, all three cross terms $q_i q_j$ contribute [57]. We choose as the reference frame the longitudinal co-moving system (LCMS) [76]. In LCMS each pair is emitted transverse to the reaction axis so that the pair rapidity vanishes. The parameter λ measures the correlation strength. For fully chaotic Gaussian source $\lambda = 1$. Experimentally observed values of $\lambda < 1$ are mainly due to contribution of very long-lived sources ($\eta, \eta', K_s^0, \Lambda, \dots$), the non-Gaussian shape of the correlation functions and particle misidentification.

The correlation functions of two identical charged pions have been calculated within the Bjorken-like and Hubble-like models with the parameters given in Table 3.1, $\eta_{\text{max}} = 2$, reasonably well describing single particle spectra in the mid-rapidity region. The three-dimensional correlation functions were fitted according to Eq. (3.81) in two k_t intervals $0.1 < k_t < 0.3$ GeV/ c and $0.3 < k_t < 0.6$ GeV/ c . In Fig. 3.7, the fitted correlation radii and strength parameter are compared with those measured by STAR collaboration [77]. One may see that the Bjorken-like model, adjusted to describe single particle spectra, describes also the decrease of

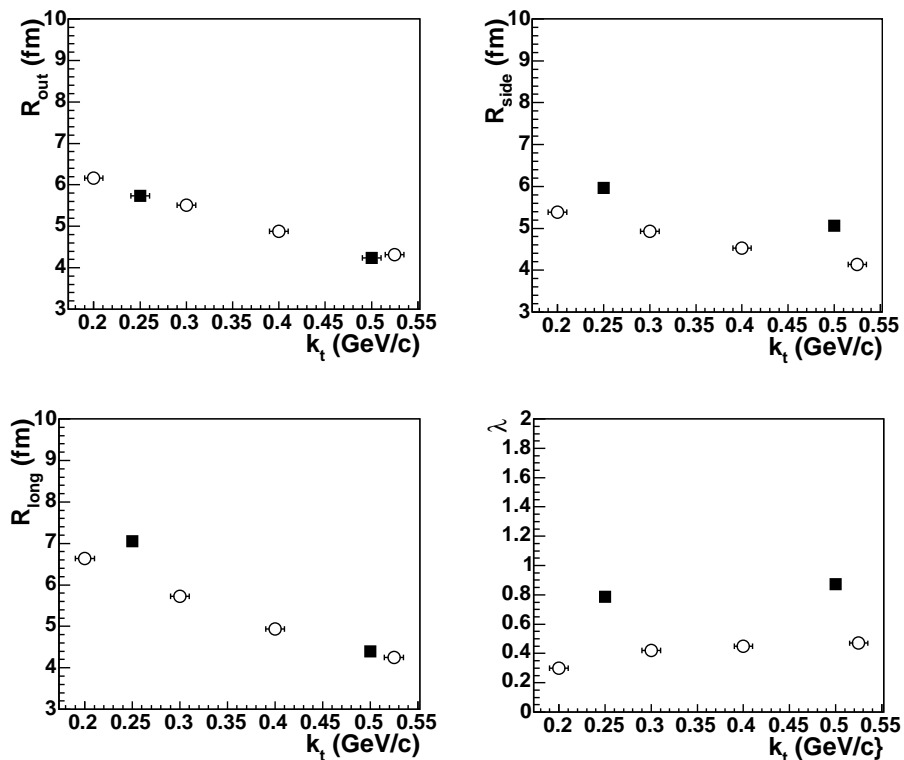


Figure 3.7: The $\pi^\pm\pi^\pm$ correlation radii and the suppression parameter λ at mid-rapidity in central $Au + Au$ collisions at $\sqrt{s_{NN}} = 200$ GeV from the STAR experiment [77] (open circles) and the MC calculations within the Bjorken-like model (up-triangles) in different intervals of the pair transverse momentum k_t .

the correlation radii with increasing k_t but overestimates their values. The situation is even worse with the Hubble-like model which is more constrained than the Bjorken-like one and yields the longitudinal radius by a factor two larger.

As for the overestimation of the correlation strength parameter λ , it is likely related to the neglected contribution of misidentified particles and pions from weak decays. Indeed, the new preliminary analysis of the STAR data with the improved particle identification [78] yields the λ parameter closer to the model results.

We would like to emphasize that the high freeze-out temperature of 165 MeV and a fixed effective volume $V_{\text{eff}} \propto \tau R^2$ make it quite difficult to describe the correlation radii within the single freeze-out model. Thus a tuning of the longitudinal radius $R_{\text{long}} \approx \tau(T/m_t)^{1/2}$ requires a small proper time τ , leading to too large values of R and $R_{\text{side}} \propto R$. The concept of a later thermal freeze-out occurring at a smaller temperature $T^{\text{th}} < T^{\text{ch}}$ and with no multiplicity constraint on the

thermal effective volume (see section 3.2) can help to resolve this problem (see, e.g., [37]).

To get a valuable information from the correlation data, one should consider more realistic models as compared with the simple Bjorken-like and Hubble-like ones (particularly, consider a more complex form of the freeze-out hypersurface taking into account particle emission from the surface of expanding system [48]) and study the problem of particle rescattering and resonance excitation after the chemical and/or thermal freeze-out (only minor effect of elastic rescatterings on particle spectra and correlations is expected [53]). For the latter, our earlier developed C++ kinetic code [53] can be coupled to the MC freeze-out generator.

3.9 Freeze-out surface parametrizations for non-central collisions

The extension of our MC generator to noncentral collisions demands mainly the modifications of freeze-out hypersurface parametrizations (Sec. V of Ref. [79]) and does not practically influence the generation procedure itself (Sec. VI of Ref. [79]). Therefore we focus on these modifications only considering the popular Bjorken-like and Hubble-like freeze-out parametrizations respectively used in so-called blast wave [37] and Cracow [38] models as the example options in our MC generator. Similar parametrizations have been used in the hadron generator THERMINATOR [87].

As usual, in the Bjorken-like parametrization, we substitute the Cartesian coordinates t, z by the Bjorken ones [49]

$$\tau = (t^2 - z^2)^{1/2}, \quad \eta = \frac{1}{2} \ln \frac{t+z}{t-z}, \quad (3.49)$$

and introduce the the radial vector $\vec{r} \equiv \{x, y\} = \{r \cos \phi, r \sin \phi\}$, i.e.,

$$x^\mu = \{\tau \cosh \eta, \vec{r}, \tau \sinh \eta\} = \{\tau \cosh \eta, r \cos \phi, r \sin \phi, \tau \sinh \eta\}. \quad (3.50)$$

For a freeze-out hypersurface represented by the equation $\tau = \tau(\eta, r, \phi)$, the hypersurface element in terms of the coordinates η, r, ϕ becomes

$$d^3\sigma_\mu = \epsilon_{\mu\alpha\beta\gamma} \frac{dx^\alpha dx^\beta dx^\gamma}{d\eta dr d\phi} d\eta dr d\phi, \quad (3.51)$$

where $\epsilon_{\mu\alpha\beta\gamma}$ is the completely antisymmetric Levy-Civita tensor in four dimensions with $\epsilon^{0123} = -\epsilon_{0123} = 1$. Generally, the freeze-out hypersurface is represented by a set of equations $\tau = \tau_j(\eta, r, \phi)$ and Eq. (3.51) should be substituted by the sum of the corresponding hypersurface elements. For the simplest and frequently used freeze-out hypersurface $\tau = \text{const}$, one has

$$\begin{aligned} d^3\sigma_\mu &= n_\mu d^3\sigma = \tau d^2\vec{r} d\eta \{\cosh \eta, 0, 0, -\sinh \eta\}, \\ d^3\sigma &= \tau d^2\vec{r} d\eta, \\ n^\mu &= \{\cosh \eta, 0, 0, \sinh \eta\}. \end{aligned} \quad (3.52)$$

In noncentral collisions the shape of the emission region in the transverse (x - y) plane can be approximated by an ellipse (as usual, the z - x plane coincides with the reaction plane). The ellipse radii $R_x(b)$ and $R_y(b)$ at a given impact parameter b are usually parametrized [37, 90, 91, 60] in terms of the spatial anisotropy $\epsilon(b) = (R_y^2 - R_x^2)/(R_x^2 + R_y^2)$ and the scale factor $R_s(b) = [(R_x^2 + R_y^2)/2]^{1/2}$,

$$R_x(b) = R_s(b) \sqrt{1 - \epsilon(b)}, \quad R_y(b) = R_s(b) \sqrt{1 + \epsilon(b)}. \quad (3.53)$$

Then from the ellipse equation,

$$\frac{x^2}{R_x^2} + \frac{y^2}{R_y^2} = 1, \quad (3.54)$$

follows the explicit dependence of the fireball transverse radius $R(b, \phi)$ on the azimuthal angle ϕ :

$$R(b, \phi) = R_s(b) \frac{\sqrt{1 - \epsilon^2(b)}}{\sqrt{1 + \epsilon(b) \cos 2\phi}}; \quad (3.55)$$

particularly, $R(b, 0) = R_x(b)$ and $R(b, \pi/2) = R_y(b)$. To reduce the number of free parameters, we assume here a simple scaling option [35]

$$R_s(b) = R_s(b=0) \sqrt{1 - \epsilon_s(b)}, \quad (3.56)$$

where $R_s(b=0) \equiv R$ is the fireball freeze-out transverse radius in central collisions. It means that the dimensionless ratio $R_s(b)/R_s(0)$ at the freeze-out moment depends on the collision energy, the radius R_A of the colliding (identical) nuclei and the impact parameter b through a dimensionless $\epsilon_s(b)$ only. It should be noted that both $\epsilon_s(b)$ and the fireball freeze-out eccentricity $\epsilon(b)$ are determined by the eccentricity $\epsilon_0(b) = b/(2R_A)$ of the elliptical overlap of the colliding nuclei at the initial moment, when

$$\left. \frac{R_s(b)}{R_s(b=0)} \right|_{\epsilon(b)=\epsilon_0(b)} \equiv \frac{R_s(b)_{\text{initial}}}{R_A} = \sqrt{1 - \epsilon_0(b)}. \quad (3.57)$$

Since $\epsilon_s(0) = \epsilon(0) = \epsilon_0(0) = 0$, one can assume that $\epsilon_s(b) \simeq \epsilon(b)$ at sufficiently small values of the impact parameter b . It appears that the use of the simple ansatz $\epsilon_s(b) = \epsilon(b)$ allows one to achieve the absolute normalization of particle spectra correct within $\sim 10\%$ up to $b \simeq R_A$ (see section 3.11).

If the system evolution were driven by the pressure gradients, the expansion would be stronger in the direction of the short ellipse x -axis (in the reaction plane), where the pressure gradient is larger than in the direction of the long ellipse y -axis (see, e.g., [82]). The typical hydrodynamic evolution scenario is shown in Fig. 3.8. During the evolution, the initial system coordinate anisotropy $\epsilon_0(b)$ is transformed into the momentum anisotropy $\delta(b)$. According to the hydrodynamical calculations, the spatial eccentricity almost disappears and the momentum anisotropy saturates at rather early evolution stage before freeze-out. As we do not trace the evolution here, we will consider the spatial and momentum anisotropies $\epsilon(b)$ and $\delta(b)$ as free parameters.

For central collisions the fluid flow four-velocity $u^\mu(t, \vec{x}) = \gamma(t, \vec{x})\{1, \vec{v}(t, \vec{x})\} \equiv \gamma(t, \vec{x})\{1, \vec{v}_\perp(t, \vec{x}), v_z(t, \vec{x})\}$ at a point \vec{x} and time t was parametrized [79] in terms

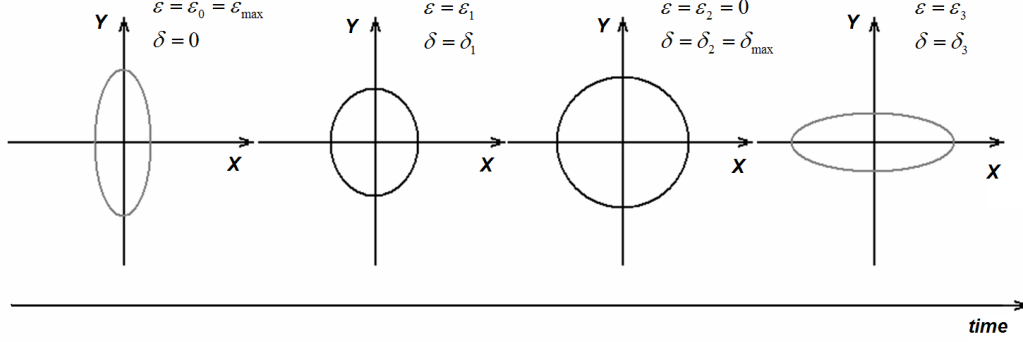


Figure 3.8: The typical hydrodynamic evolution scenario.

of the longitudinal (z) and transverse (\perp) fluid flow rapidities

$$\eta_u(t, \vec{x}) = \frac{1}{2} \ln \frac{1 + v_z(t, \vec{x})}{1 - v_z(t, \vec{x})}, \quad \rho_u(t, \vec{x}) = \frac{1}{2} \ln \frac{1 + v_\perp(t, \vec{x}) \cosh \eta_u(t, \vec{x})}{1 - v_\perp(t, \vec{x}) \cosh \eta_u(t, \vec{x})}, \quad (3.58)$$

where $v_\perp = |\vec{v}_\perp|$ is the magnitude of the transverse component of the flow three-velocity $\vec{v} = \{v_\perp \cos \phi_u, v_\perp \sin \phi_u, v_z\}$, i.e.,

$$u^\mu(t, \vec{x}) = \{\cosh \rho_u \cosh \eta_u, \sinh \rho_u \cos \phi_u, \sinh \rho_u \sin \phi_u, \cosh \rho_u \sinh \eta_u\} \\ = \{(1 + u_\perp^2)^{1/2} \cosh \eta_u, \vec{u}_\perp, (1 + u_\perp^2)^{1/2} \sinh \eta_u\}, \quad (3.59)$$

$\vec{u}_\perp = \gamma \vec{v}_\perp = \gamma_\perp \cosh \eta_u \vec{v}_\perp$, $\gamma_\perp = \cosh \rho_u$. However, unlike the transverse isotropic parametrization ($\phi_u = \phi$), now the azimuthal angle ϕ_u of the fluid velocity vector is not necessarily identical to the spatial azimuthal angle ϕ , because of the nonzero flow anisotropy parameter $\delta(b)$ [91, 60] :

$$u^\mu(t, \vec{x}) = \{\gamma_\phi \cosh \tilde{\rho}_u \cosh \eta_u, \sqrt{1 + \delta(b)} \sinh \tilde{\rho}_u \cos \phi, \\ \sqrt{1 - \delta(b)} \sinh \tilde{\rho}_u \sin \phi, \gamma_\phi \cosh \tilde{\rho}_u \sinh \eta_u\}, \quad (3.60)$$

where

$$\gamma_\phi = \sqrt{1 + \delta(b) \tanh^2 \tilde{\rho}_u \cos 2\phi}, \quad (3.61)$$

$$\tan \phi_u = \sqrt{\frac{1 - \delta(b)}{1 + \delta(b)}} \tan \phi. \quad (3.62)$$

The transverse flow rapidity ρ_u is related to $\tilde{\rho}_u$ by:

$$u_\perp = \sinh \rho_u = \sqrt{1 + \delta(b) \cos 2\phi} \sinh \tilde{\rho}_u. \quad (3.63)$$

Note, that for $\delta(b) = 0$ (i.e. $\phi_u = \phi$), Eq. (3.60) reduces to Eq. (3.59) which was applied in Refs. [35, 92]. In Ref. [60], $\delta(b)$ is obtained by fitting the model prediction to the measured elliptic flow coefficient v_2 .

Further we assume the longitudinal boost invariance [49] $\eta_u = \eta$, which is a good approximation for the highest RHIC energies at the midrapidity region. To account for the violation of the boost invariance, we have also included in the code an option corresponding to the substitution of the uniform distribution of the space-time longitudinal rapidity η in the interval $[-\eta_{\max}, \eta_{\max}]$ by a Gaussian distribution $\exp(-\eta^2/2\Delta\eta^2)$ with a width parameter $\Delta\eta = \eta_{\max}$. The presence of the “oscillation term” $\sqrt{1 + \delta(b)} \cos 2\phi$ in the transverse component u_\perp of the flow velocity in Eq. (3.63) allows us to use the simple linear profile for $\tilde{\rho}_u$ without introduction of the additional parameters for each centrality (b) unlike other models, namely:

$$\tilde{\rho}_u = \frac{r}{R_s(b)} \rho_u^{\max}(b=0), \quad (3.64)$$

where $\rho_u^{\max}(b=0)$ is the maximal transverse flow rapidity for central collisions. At such normalization and $\delta(b) > \epsilon(b)$ the maximal transverse flow (u_\perp, ρ_u) is achieved at $\phi = 0$, i.e. along x -axis as it should be according to the hydrodynamic scenario described above (Fig. 3.8). (although $\tilde{\rho}_u$ has a maximum at $\phi = \pi/2$!)

Here one should note that the “popular parametrization” of transverse flow rapidity used in Ref. [37] (and implemented as an option in our MC generator also):

$$\rho_u = \tilde{r}[\rho_0(b) + \rho_2(b) \cos 2\phi_u], \quad (3.65)$$

where

$$\tilde{r} \equiv \sqrt{\left(\frac{r \cos \phi}{R_x}\right)^2 + \left(\frac{r \sin \phi}{R_y}\right)^2} = \frac{r}{R(b, \phi)} \quad (3.66)$$

is the “normalized elliptical radius”, $\rho_0(b)$ and $\rho_2(b)$ are the two fitting parameters, is close to our parametrization and gives the similar results for observables under consideration. In parametrization of Ref. [37] the boost is perpendicular to the elliptical subshell on which the source element is found: $\tan \phi_u = (R_x^2/R_y^2) \tan \phi = (1 - \epsilon)/(1 + \epsilon) \tan \phi$ and $\delta(b) = 2\epsilon(b)/(1 + \epsilon^2(b))$. It is interesting to note that for sufficiently weak transverse flows, $\rho_u \leq 1$, considered here, one can put $\sinh \rho_u \simeq \rho_u$ and obtain our parametrization from that of Ref. [37] by substitutions

$$\frac{\rho_0(b)}{R(b, \phi)} \rightarrow \frac{\rho_u^{\max}(b=0)}{R_s(b)} \quad 1 + \frac{\rho_2(b)}{\rho_0(b)} \cos 2\phi_u \rightarrow \sqrt{1 + \delta(b)} \cos 2\phi. \quad (3.67)$$

Thus, in the case of moderate transverse flows, one can obtain the same result either by fixing the direction of the flow velocity vector but allowing for the azimuthal dependence of the flow rapidity or by allowing for arbitrary direction of the flow velocity vector but assuming azimuthally independent flow rapidity.

At $\tau = \text{const}$, the total effective volume for particle production in the case of noncentral collisions becomes

$$V_{\text{eff}} = \int_{\sigma(t, \vec{x})} d^3\sigma_{\mu}(t, \vec{x}) u^{\mu}(t, \vec{x}) = \tau \int_0^{2\pi} d\phi \int_0^{R(b, \phi)} (n_{\mu} u^{\mu}) r dr \int_{\eta_{\min}}^{\eta_{\max}} d\eta \quad (3.68)$$

where $(n_{\mu} u^{\mu}) = \cosh \tilde{\rho}_u \sqrt{1 + \delta(b) \tanh^2 \tilde{\rho}_u \cos 2\phi}$.

We also consider the Cracow model scenario [38] corresponding to the Hubble-like freeze-out hypersurface $\tau_H = (t^2 - x^2 - y^2 - z^2)^{1/2} = \text{const}$. Introducing the longitudinal space-time rapidity η according to Eq. (3.49) and the transverse space-time rapidity $\rho = \sinh^{-1}(r/\tau_H)$, one has [51]

$$x^{\mu} = \tau_H \{ \cosh \eta \cosh \rho, \sinh \rho \cos \phi, \sinh \rho \sin \phi, \sinh \eta \cosh \rho \}, \quad (3.69)$$

$\tau_H = \tau_B / \cosh \rho$. Representing the freeze-out hypersurface by the equation $\tau_H = \tau_H(\eta, \rho, \phi) = \text{const}$, one finds from Eq. (3.51):

$$\begin{aligned} d^3\sigma &= \tau_H^3 \sinh \rho \cosh \rho d\eta d\rho d\phi = \tau_H d\eta d^2\vec{r}, \\ n^{\mu}(t, \vec{x}) &= x^{\mu}(t, \vec{x}) / \tau_H. \end{aligned} \quad (3.70)$$

With the additional flow anisotropy parameter $\delta(b)$ the flow four-velocity is parametrized as [60]:

$$u^{\mu}(t, \vec{x}) = \{ \gamma_{\phi}^H \cosh \rho \cosh \eta, \sqrt{1 + \delta(b)} \sinh \rho \cos \phi, \sqrt{1 - \delta(b)} \sinh \rho \sin \phi, \gamma_{\phi}^H \cosh \rho \sinh \eta \}, \quad (3.71)$$

where

$$\gamma_{\phi}^H = \sqrt{1 + \delta(b) \tanh^2 \rho \cos 2\phi}. \quad (3.72)$$

The effective volume corresponding to $r = \tau_H \sinh \rho < R(b, \phi)$ and $\eta_{\min} \leq \eta \leq \eta_{\max}$ is

$$V_{\text{eff}} = \int_{\sigma(t, \vec{x})} d^3\sigma_{\mu}(t, \vec{x}) u^{\mu}(t, \vec{x}) = \tau_H \int_0^{2\pi} d\phi \int_0^{R(b, \phi)} (n_{\mu} u^{\mu}) r dr \int_{\eta_{\min}}^{\eta_{\max}} d\eta \quad (3.73)$$

with

$$\begin{aligned} (n_{\mu} u^{\mu}) &= \cosh^2 \rho \left(\sqrt{1 + \delta(b) \tanh^2 \rho \cos 2\phi} \right. \\ &\quad \left. - \tanh^2 \rho (\sqrt{1 + \delta(b)} \cos^2 \phi + \sqrt{1 - \delta(b)} \sin^2 \phi) \right) \simeq 1 + o(\delta^2(b)). \end{aligned} \quad (3.74)$$

Our MC procedure to generate the freeze-out hadron multiplicities, four-momenta and four-coordinates for central collisions has been described in detail in Ref. [79]. For noncentral collisions, only the generation of the transverse radius r is slightly different, taking place in the azimuthally dependent interval $[0, R(b, \phi)]$.

3.10 Different chemical and thermal freeze-outs

Since the assumption of a common chemical and thermal freeze-out can hardly be justified (see, e.g., [27]), we consider here a more complicated scenario with different chemical and thermal freeze-outs.

The mean particle numbers \bar{N}_i^{th} at thermal freeze-out can be determined using the following procedure [27]. Above in this chapter, the temperature and chemical potentials at chemical freeze-out have been fixed by fitting the ratios of the numbers of (quasi)stable particles. The common factor, $V_{\text{eff}}^{\text{ch}}$, and, thus, the absolute particle and resonance numbers was fixed by pion multiplicities. Within the concept of chemically frozen evolution these numbers are assumed to be conserved except for corrections due to decay of some part of short-lived resonances that can be estimated from the assumed chemical to thermal freeze-out evolution time. Then one can calculate the mean numbers of different particles and resonances reaching a (common) thermal freeze-out hypersurface. At a given thermal freeze-out temperature T^{th} these mean numbers can be expressed through the thermal effective volume $V_{\text{eff}}^{\text{th}}$ and the chemical potentials for each particle species μ_i^{th} . The latter can no longer be expressed in the form $\mu_i = \vec{q}_i \vec{\mu}$, which is valid only for chemically equilibrated systems. For a given parametrization of the thermal freeze-out hypersurface, the thermal effective volume $V_{\text{eff}}^{\text{th}}$ (and thus all μ_i^{th}) can be fixed with the help of pion interferometry data.

In practical calculations the particle number density $\rho_i^{\text{eq}}(T, \mu_i)$ is represented in the form of a fast converging series [79]:

$$\rho_i^{\text{eq}}(T, \mu_i) = \frac{g_i}{2\pi^2} m_i^2 T \sum_{k=1}^{\infty} \frac{(\mp)^{k+1}}{k} \exp\left(\frac{k\mu_i}{T}\right) K_2\left(\frac{km_i}{T}\right), \quad (3.75)$$

where K_2 is the modified Bessel function of the second order, m_i and $g_i = 2J_i + 1$ are the mass and the spin degeneracy factor of particle i respectively.

Using Eq. (3.75) and the assumption of the conservation of the particle number ratios from the chemical to thermal freeze-out evolution time, we obtain the following ratios for i -particle specie to π^+ :

$$\frac{\rho_i^{\text{eq}}(T^{\text{ch}}, \mu_i)}{\rho_{\pi^+}^{\text{eq}}(T^{\text{ch}}, \mu_{\pi^+}^{\text{ch}})} = \frac{\rho_i^{\text{eq}}(T^{\text{th}}, \mu_i^{\text{th}})}{\rho_{\pi^+}^{\text{eq}}(T^{\text{th}}, \mu_{\pi^+}^{\text{eff th}})}. \quad (3.76)$$

The absolute values of particles densities $\rho_i^{\text{eq}}(T^{\text{th}}, \mu_i^{\text{th}})$ are determined by the choice of the free parameter of the model: effective pion chemical potential $\mu_{\pi^+}^{\text{eff th}}$ at the temperature of thermal freeze-out T^{th} . Assuming for the other particles (heavier then pions) the Boltzmann approximation in Eq. (3.75) one deduces from Eqs. (3.75) - (3.76) the chemical potentials of particles and resonances at thermal

freeze-out:

$$\mu_i^{\text{th}} = T^{\text{th}} \ln\left(\frac{\rho_i^{\text{eq}}(T^{\text{ch}}, \mu_i^{\text{ch}})}{\rho_i^{\text{eq}}(T^{\text{th}}, \mu_i = 0)} \frac{\rho_\pi^{\text{eq}}(T^{\text{th}}, \mu_\pi^{\text{eff th}})}{\rho_\pi^{\text{eq}}(T^{\text{ch}}, \mu_i^{\text{ch}})}\right). \quad (3.77)$$

The correct way to determine the best set of model parameters would be achieved by fitting all the observables together as it was suggested in Ref. [57], but for our MC-type model it is technically impossible. For the example calculations with our model at RHIC energies we choose $T^{\text{ch}} = 0.165$ GeV and the thermal temperatures as in the analytical models which performed the successful fitting of RHIC data: $T^{\text{th}} = T^{\text{ch}} = 0.165$ GeV (Cracow model [38]) and $T^{\text{th}} = 0.100$ GeV (Blast-Wave model [37]), and some arbitrary intermediate temperature $T^{\text{th}} = 0.130$ GeV. It is well known (see, e.g., [27]) that the pion transverse spectra at thermal freeze-out can be described in two regimes: low temperature and large transverse flow on the one hand, and higher temperature and non-relativistic transverse flow on the other hand (see section 3.11). The low temperature regime seems to be preferable because the strong transverse flow is expected to describe the large inverse slopes of transverse spectra of the heavy hadrons (especially protons) and small correlation radii obtained at RHIC better [37, 48]. We present the calculated correlation radii in section 3.11.

In the considered here last version of FASTMC the new table of resonances was included. It contains 360 resonances and stable particles, instead of 85 ones included in the previous versions. This particle table is produced from the SHARE [94] particle table excluding not well established resonances states. The decays of resonances are controlled by its lifetime $1/\Gamma$, there Γ is the width of resonance specified in the particle table, and they occur with the probability density $\Gamma \exp(-\Gamma\tau)$ in the resonance rest frame. Then the decay products are boosted to the reference frame in which the freeze-out hypersurface was defined. Because we need to compare our calculations with data from different experiments we made possible to switch on/off different decays based on their lifetime (i.e. turn on/off weak decays). Only the two- and three-body decays are considered in our model. The branching ratios are also taken from the particle decay table produced from the SHARE decay table [94]. The cascade decays are also possible.

3.11 Input parameters and results for non-central collisions

Model input parameters

First, we summarize the input parameters which control the execution of our MC hadron generator in the case of Bjorken-like and Hubble-like parametrizations, and should be specified for different energies, ion beams and event centralities.

1. Thermodynamic parameters at chemical freeze-out: temperature T^{ch} and chemical potentials per a unit charge $\tilde{\mu}_B, \tilde{\mu}_S, \tilde{\mu}_Q$. As an option, an additional parameter $\gamma_s \leq 1$ takes into account the strangeness suppression according to the partially equilibrated distribution [54, 55]:

$$f_i(p^{*0}; T, \mu_i, \gamma_s) = \frac{g_i}{\gamma_s^{-n_i^s} \exp([p^{*0} - \mu_i]/T) \pm 1}, \quad (3.78)$$

where n_i^s is the number of strange quarks and antiquarks in a hadron i , p^{*0} is the hadron energy in the fluid element rest frame, $g_i = 2J_i + 1$ is the spin degeneracy factor. Optionally, the parameter γ_s can be fixed using its phenomenological dependence on the temperature and baryon chemical potential [56].

2. Volume parameters: the fireball transverse radius $R(b=0)$ (determined in central collisions; in noncentral collisions we use the scaling option (3.56,3.57) to recalculate $R(b)$ from $R(b=0)$), the freeze-out proper time τ and its standard deviation $\Delta\tau$ (emission duration) [93].
3. Maximal transverse flow rapidity $\rho_u^{\text{max}}(b=0)$ for Bjorken-like parametrization in central collisions.
4. Maximal space-time longitudinal rapidity η_{max} which determines the rapidity interval $[-\eta_{\text{max}}, \eta_{\text{max}}]$ in the collision center-of-mass system. To account for the violation of the boost invariance, we have included in the code an option corresponding to the substitution of the uniform distribution of the space-time longitudinal rapidity η in the interval $[-\eta_{\text{max}}, \eta_{\text{max}}]$ by a Gaussian distribution $\exp(-\eta^2/2\Delta\eta^2)$ with a width parameter $\Delta\eta = \eta_{\text{max}}$ (see, e.g., [57, 35]).
5. Impact parameter range: minimal b_{min} and maximal b_{max} impact parameters.
6. Flow anisotropy parameter $\delta(b)$ in Bjorken-like and Hubble-like parametrizations (or $\rho_0(b)$ and $\rho_2(b)$ in the ‘‘Blast-Wave’’ parametrization of Ref. [37]).
7. Coordinate anisotropy parameter $\epsilon(b)$.
8. Thermal freeze-out temperature T^{th} (if single freeze-out is considered, $T^{\text{th}} = T^{\text{ch}}$).
9. Effective chemical potential of π^+ at thermal freeze-out $\mu_\pi^{\text{eff th}}$ (0, if single freeze-out is considered).
10. Parameter which enables/disables weak decays.

Table 3.4: Model parameters for central Au + Au collisions at $\sqrt{s_{NN}} = 200$ GeV. Chemical freeze-out parameters: $T^{\text{ch}}=0.165$ GeV, $\tilde{\mu}_B=0.028$ GeV, $\tilde{\mu}_S=0.007$ GeV, $\tilde{\mu}_Q = -0.001$ GeV.

T^{th} , GeV	0.165	0.130	0.100
τ , fm/c	7.0	7.2	8.0
$\Delta\tau$, fm/c	2.0	2.0	2.0
$R(b=0)$, fm	9.0	9.5	10.0
$\rho_u^{\text{max}}(b=0)$	0.65	0.9	1.1
$\mu_\pi^{\text{eff th}}$	0.	0.10	0.11

Table 3.5: Model parameters for Au + Au collisions at $\sqrt{s_{NN}} = 200$ GeV at different centralities. Chemical freeze-out parameters: $T^{\text{ch}}=0.165$ GeV, $\tilde{\mu}_B=0.028$ GeV, $\tilde{\mu}_S=0.007$ GeV, $\tilde{\mu}_Q = -0.001$ GeV. Thermal freeze-out parameters: $T^{\text{th}}=0.1$ GeV, $\mu_\pi^{\text{eff th}}=0.11$ GeV. Volume parameters determined in the central collisions: $R(b=0) = 10.0$ fm, $\tau = 8.0$ fm/c, $\rho_u^{\text{max}}(b=0) = 1.1$

centrality	c=0-5%	c=5-10%	c=10-20%	c=20-30%	c=30-40%	c=40-60%
b_{min}/R_A	0.	0.447	0.632	0.894	1.095	1.265
b_{max}/R_A	0.447	0.632	0.894	1.095	1.265	1.549
$\epsilon(b)$	0	0	0	0.1	0.15	0.15
$\delta(b)$	0.05	0.08	0.12	0.25	0.34	0.36

The parameters used to simulate central collisions are given in Table 3.4. The parameters determined in central collisions for $T^{\text{th}}=0.1$ GeV: $\tau=8.0$ fm/c, $R(b=0)=10.$ fm, $\Delta\tau=2.0$ fm/c; $\rho_u^{\text{max}}(b=0) = 1.1$ (3-th column in Table 3.4) were used to simulate Au+Au collisions at $\sqrt{s_{NN}} = 200$ GeV at different centralities. The additional parameters needed only for noncentral collisions are given in Table 3.5.

m_t -spectra

In Fig. 3.9 the m_t -spectra measured by the STAR Collaboration [95] at 0 – 5% centrality are shown for π^+ , K^+ and p in comparison with the model calculations under the assumption of the common chemical and thermal freeze-out at $T^{\text{th}} = T^{\text{ch}} = 0.165$ GeV (Fig. 3.9(a)) and under the assumption that the thermal freeze-out at $T^{\text{th}} = 0.100, 0.130$ GeV occurs after the chemical one (Fig. 3.9(b, c)).

The correction on weak decays was introduced by the STAR Collaboration in pion spectra only [95]. It was approximately 12% and was estimated from the measured K_s^0 and Λ decays. In Ref. [95] the STAR Collaboration doesn't introduce the weak decay correction in proton spectra. To reproduce the STAR weak decay correction procedure, we excluded pions from K_s^0 and Λ decays from pions m_t -

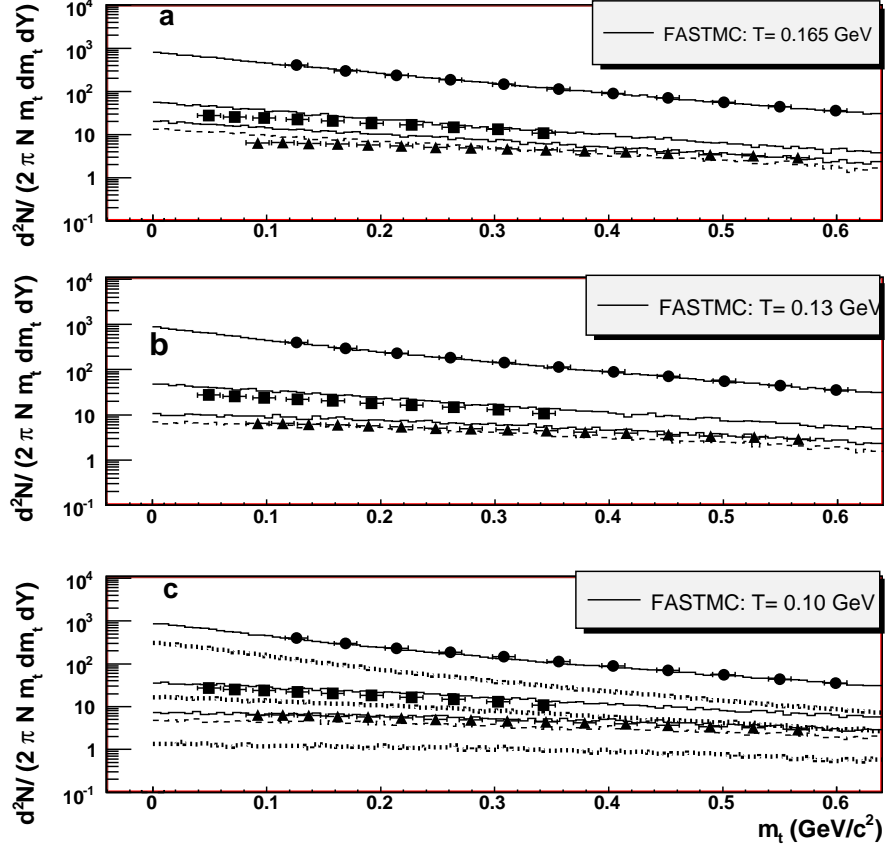


Figure 3.9: m_t -spectra (in c^4/GeV^2) measured by the STAR Collaboration [95] for π^+ (circles), K^+ (squares) and p (up-triangles) at 0 – 5% centrality in comparison with the model calculations at $T^{\text{th}} = 0.165(a), 0.130(b), 0.100(c)$ GeV, with the parameters from Table 3.4, for protons weak decays are taken into account (solid lines); for protons weak decays are not taken into account (dashed lines). The direct π^+ , K^+ and p contributions are shown on (c) by dotted lines.

spectra in Fig. 3.9. The contribution of weak decays in the simulated proton spectra can be estimated from Fig. 3.9 by comparison of the solid lines (protons from K_s^0 and Λ decays are included) and the dashed lines (without contribution of protons from the weak decays). The model parameters at different temperatures are presented in Table 3.4. The parameters were optimized this way to obtain the good description of the pion m_t -spectra and the correlation radii. The best description of the m_t -spectra was achieved at $T^{\text{th}} = 0.100$ GeV (Fig. 3.9(c)).

The same set of parameters $T, \rho_u^{\text{max}}, R$ and τ which was determined for central collisions (Table 3.4) was used for noncentral ones. The additional parameters of the model for noncentral collisions were coordinate and momentum asymmetries: ϵ and δ (Table 3.5). At the freeze-out moment we consider them as free parameters because we do not trace the evolution here. The influence of the choice of ϵ and δ on m_t -spectra averaged over azimuthal angle φ is negligible. The decrease of the effective volume in noncentral collisions (Eq. 3.68) due to nonzero values of ϵ and δ allows us to obtain the correct absolute normalization of m_t -spectra without introduction of the additional parameters. In Fig. 3.10 the m_t -spectra measured by the STAR Collaboration [95] are shown for π^+, K^+ and p at centralities: 0 – 5%, 5 – 10%, 10 – 20%, 20 – 30%, 30 – 40%, 40 – 50% in comparison with the model calculations which assume that the thermal freeze-out at $T^{\text{th}} = 0.1$ GeV occurs after the chemical one (solid lines). It appears that the procedure described in section 3.9 allows one to achieve the absolute normalization of pion spectra correct within $\sim 13\%$.

Elliptic flow

Following a standard procedure [96, 97] we make a Fourier expansion of the hadron distribution in the azimuthal angle φ at mid-rapidity:

$$\frac{dN}{d^2p_t dy} = \frac{dN}{2\pi p_t dp_t dy} (1 + 2v_2 \cos 2\varphi + 2v_4 \cos 4\varphi + \dots). \quad (3.79)$$

The elliptic flow coefficient, v_2 , is defined as the second order Fourier coefficient,

$$v_2 = \frac{\int_0^{2\pi} d\varphi \cos 2(\varphi - \psi_R) \frac{d^3 N}{dy d\varphi p_t dp_t}}{\int_0^{2\pi} d\varphi \frac{d^3 N}{dy d\varphi p_t dp_t}}, \quad (3.80)$$

where ψ_R is the reaction plane angle (in our generation $\psi_R = 0$), y and p_t are the rapidity and transverse momentum of particle under consideration, respectively.

The value of v_2 is an important signature of the physics occurring in heavy ion collisions. According to the typical hydrodynamic scenario shown in Fig. 3.8, the elliptic flow is generated mainly during the high density phase of the fireball evolution. The system driven by the internal pressure gradients expands more

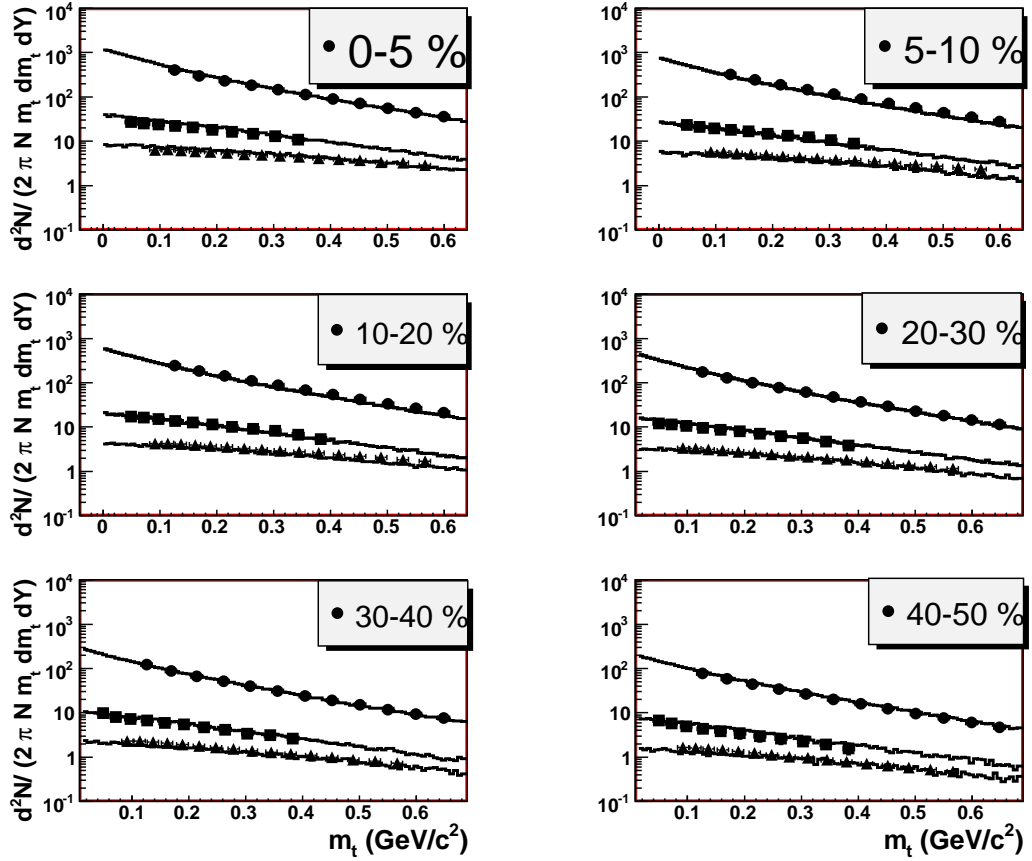


Figure 3.10: m_t -spectra (in c^4/GeV^2) measured by the STAR Collaboration [95] for π^+ (circles), K^+ (squares) and p (up-triangles) at different centralities in comparison with our fast MC calculations at $T^{\text{th}} = 0.100$ GeV (solid lines) with the parameters from Table 3.4 and Table 3.5.

strongly in its short direction (into the direction of the impact parameter x in Fig. 3.8, which is chosen as a “positive” direction) than in the perpendicular one (“negative” direction, y in Fig. 3.8) where the pressure gradients are smaller. Figure 3.8 illustrates qualitatively that the initial spacial anisotropy of the system disappears during the evolution, while the momentum anisotropy grows. The developing of strong flow observed at RHIC requires a short time scale and large pressure gradients, which are characteristics of a strongly interacting system. The reason for the generation of v_2 at the early times is that the system should be hot and dense, when the system cools and become less dense the developing of the large pressure gradients becomes impossible. The elliptic flow coefficient, v_2 , depends on the transverse momentum p_t , the impact parameter b or centrality, as well as, the type of the considered particle. All these dependencies have been measured at RHIC [98].

The p_t -dependence of v_2 measured by the STAR Collaboration [98] for charged particles at centralities: 0 – 5%, 5 – 10%, 10 – 20%, 20 – 30%, 30 – 40%, 40 – 60% is shown in Fig. 3.11 in comparison with our MC calculations obtained with the optimal model parameters from Table 3.5. The calculations were performed under the assumption that thermal freeze-out at $T^{\text{th}} = 0.1$ GeV occurs after the chemical one at $T^{\text{th}} = 0.165$ GeV.

The calculations under the assumption of the common chemical and thermal freeze-out at $T^{\text{th}} = T^{\text{ch}} = 0.165$ GeV demonstrate not so good agreement with the experimental data at small $p_t < 0.4$ GeV/ c for the centralities larger than 20%; irrespective of the choice of ϵ and δ one cannot get a satisfactory description in the whole p_t -range (see e.g. Fig. 3.12).

Correlation radii

The parameters of the model presented in Table 3.4 were optimized to obtain the best description of the pion m_t -spectra and the correlation radii in the following cases: under the assumption of the common chemical and thermal freeze-out at $T^{\text{th}} = T^{\text{ch}} = 0.165$ GeV and under the assumption that the thermal freeze-out at $T^{\text{th}} = 0.100, 0.130$ GeV occurs after the chemical one. In Fig. 3.13 the fitted correlation radii R_{out} , R_{side} and R_{long} are compared with those measured by the STAR Collaboration [77]. The three-dimensional correlation function was fitted with the standard Gaussian formula:

$$CF(p_1, p_2) = 1 + \lambda \exp(-R_{\text{out}}^2 q_{\text{out}}^2 - R_{\text{side}}^2 q_{\text{side}}^2 - R_{\text{long}}^2 q_{\text{long}}^2), \quad (3.81)$$

where $\vec{q} = \vec{p}_1 - \vec{p}_2 = (q_{\text{out}}, q_{\text{side}}, q_{\text{long}})$ is the relative three-momentum of two identical particles with four-momenta p_1 and p_2 . The form of Eq. (3.81) assumes azimuthal symmetry of the production process [74]. Generally, e.g., in the case of the correlation analysis with respect to the reaction plane, all three cross terms

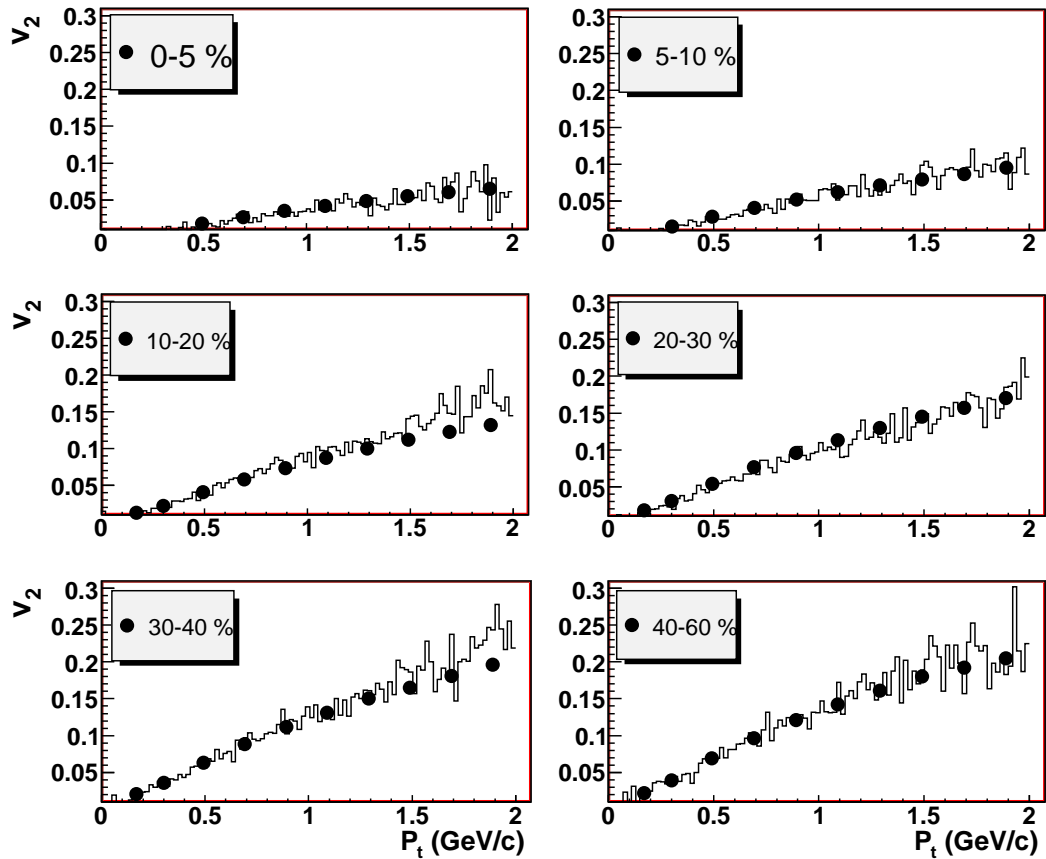


Figure 3.11: The p_t -dependence of v_2 measured by the STAR Collaboration [98] (points) for charged particles at different centralities in comparison with our fast MC calculations at $T^{\text{th}} = 0.100$ GeV (solid line) with the parameters from Table 3.4 and Table 3.5.

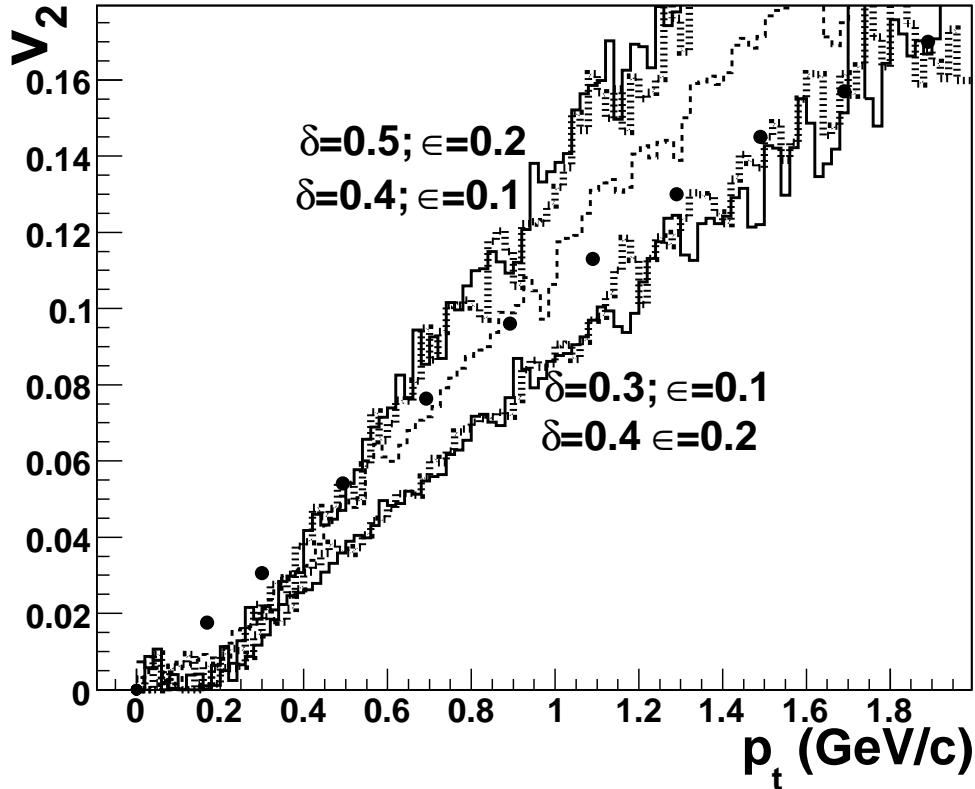


Figure 3.12: The p_t -dependence of v_2 measured by the STAR Collaboration [98] (points) for charged particles at centrality 20–30% in comparison with our fast MC calculations under assumption of the single freeze-out at $T^{\text{th}} = T^{\text{ch}} = 0.165$ GeV. The different sets of coordinate and momentum asymmetries parameters were tried: $\epsilon = 0.1$, $\delta = 0.3$ (solid line), $\epsilon = 0.2$, $\delta = 0.4$ (dotted line), $\epsilon = 0.1$, $\delta = 0.4$ (solid line), $\epsilon = 0.2$, $\delta = 0.5$ (dotted line), $\epsilon = 0.15$, $\delta = 0.4$ (dashed line)

$q_i q_j$ can be significant [57]. We will consider this case below. We choose the longitudinal co-moving system (LCMS) as the reference frame [76]. In LCMS each pair is emitted transverse to the reaction axis so that the pair rapidity vanishes. The parameter λ measures the correlation strength.

The regime with the large temperature $T^{\text{th}} = T^{\text{ch}} = 0.165$ GeV was tested in Ref. [79]. We have repeated this test here with the new resonances table and the additional parameter $\Delta\tau$ (Fig. 3.13(a), dashed line). We have found that these modifications lead to a better description of the correlation radii. In Fig. 3.13(a, bottom) (dashed line) the intercept λ is larger than the experimental one, but taking into account the secondary pions from the weak decays essentially improves the description of the λ (Fig. 3.13(a, bottom), solid line).

In Fig. 3.13(b, c) we consider the lower thermal freeze-out temperatures: 0.130, 0.100 GeV. The secondary pions coming from the weak decays were taken into account.

It is worth to note a good description of the correlation radii (within $\sim 10\%$ accuracy) altogether with the absolute value of the m_t spectra in the scenario with a low temperature thermal freeze-out of chemically frozen hadron-resonance gas. There are three important reasons for this success. First, a relatively small (compared with dynamic models) effective volume of the system $\sim \tau R^2$ that reduces the correlation radii. Second, relatively large transverse flow in the model that further reduces the radii. Third, rather large effective pion chemical potential which is needed to describe the absolute value of the pion spectra at relatively small effective volumes; it reduces correlation radii at small p_t and so makes their m_t behavior flatter. This reduction happens due to vanishing of the homogeneity length of Bose-Einstein distribution for low- p_t pions when the pion chemical potential approaches the pion mass (see also Ref. [99] for the analysis of the reduction of the pion correlation radii near the point of the Bose-Einstein condensation in static systems). We do not consider here the question whether such conditions could be realized in realistic dynamical models.

It should be noted that the description of the k_t -dependence of the correlation radii has been achieved within $\sim 10\%$ accuracy for all three considered thermal temperatures: $T^{\text{th}} = 0.165, 0.130, 0.100$ GeV. However, at lower temperatures there is more flexibility in the simultaneous description of particle spectra and correlations because the effective volume isn't strictly fixed as it is in the case of the single freeze-out ($T^{\text{th}} = T^{\text{ch}} = 0.165$ GeV). In present work, we have not attempted to fit the model parameters ($T^{\text{th}}, R, \tau, \mu_\pi^{\text{eff th}}$) since it is rather complicated task requiring a lot of computer time. We have performed only example calculations with several sets of the parameters.

In noncentral collisions the measurement of azimuthally sensitive correlation radii provides the additional information about the source shape. For the corresponding femtoscopy formalism with respect to the reaction plane see, e.g., [91, 57].

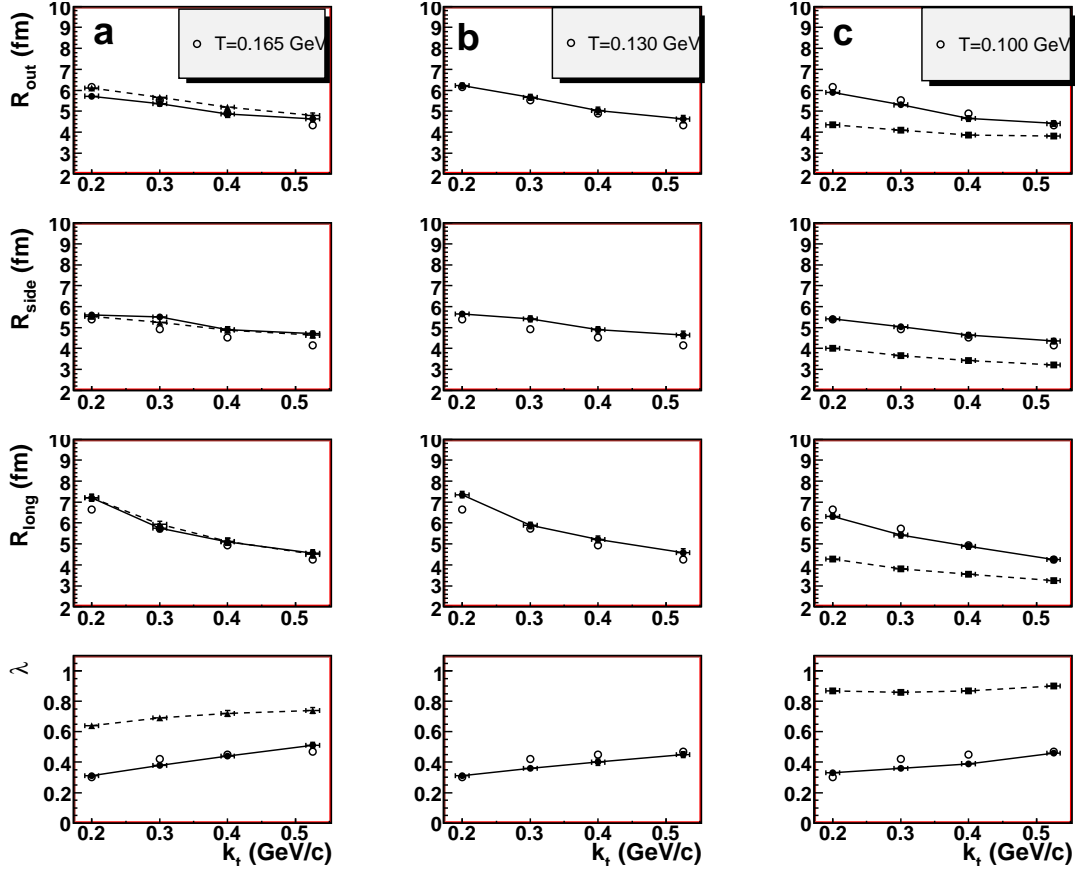


Figure 3.13: The π^+ correlation radii at mid-rapidity in central Au+Au collisions at $\sqrt{s_{NN}} = 200$ GeV from the STAR experiment [77] (open circles) and MC calculations within the Bjorken-like model with the parameters presented in Table 3.4 in different intervals of the pair transverse momentum k_t . The full calculation with resonances (a), (b). (a) single freeze-out $T^{\text{ch}} = T^{\text{th}} = 0.165$ GeV, no weak decays (dashed line), with weak decays (solid line); (b) thermal freeze-out at $T^{\text{th}} = 0.130$ GeV occurs after the chemical one, weak decays are taken into account (solid line); (c) the full calculation with resonances, weak decays are taken into account at $T^{\text{th}} = 0.100$ GeV (solid line), the direct pions only (dotted lines).

In the absence of azimuthal symmetry, the three additional cross terms contribute to the Gaussian parametrization of the correlation function in Eq. (3.81):

$$CF(p_1, p_2) = 1 + \lambda \exp(- R_o^2 q_{out}^2 - R_s^2 q_{side}^2 - R_l^2 q_{long}^2 - 2R_{os}^2 q_{out} q_{side} - 2R_{ol}^2 q_{out} q_{long} - 2R_{sl}^2 q_{side} q_{long}). \quad (3.82)$$

In the boost-invariant case, the transverse-longitudinal cross terms R_{ol}^2 and R_{sl}^2 vanish in the LCMS frame, while the important out-side R_{os}^2 cross term is present.

In the Gaussian approximation, the radii in the Eq. (3.82) are related to space-time variances via the set of equations [91, 57]:

$$\begin{aligned} R_s^2 &= 1/2(\langle \tilde{x}^2 \rangle + \langle \tilde{y}^2 \rangle) - 1/2(\langle \tilde{x}^2 \rangle - \langle \tilde{y}^2 \rangle) \cos(2\Phi) - \langle \tilde{x}\tilde{y} \rangle \sin(2\Phi), \\ R_o^2 &= 1/2(\langle \tilde{x}^2 \rangle + \langle \tilde{y}^2 \rangle) + 1/2(\langle \tilde{x}^2 \rangle - \langle \tilde{y}^2 \rangle) \cos(2\Phi) + \langle \tilde{x}\tilde{y} \rangle \sin(2\Phi) \\ &\quad - 2\beta_\perp (\langle \tilde{t}\tilde{x} \rangle \cos(\Phi) + \langle \tilde{t}\tilde{y} \rangle \sin(\Phi)) + \beta_\perp^2 \langle \tilde{t}^2 \rangle, \\ R_l^2 &= \langle \tilde{z}^2 \rangle - 2\beta_l \langle \tilde{t}\tilde{z} \rangle + \beta_l^2 \langle \tilde{t}^2 \rangle, \\ R_{os}^2 &= \langle \tilde{x}\tilde{y} \rangle \cos(2\Phi) - 1/2(\langle \tilde{x}^2 \rangle - \langle \tilde{y}^2 \rangle) \sin(2\Phi) \\ &\quad + \beta_\perp (\langle \tilde{t}\tilde{x} \rangle \sin(\Phi) - \langle \tilde{t}\tilde{y} \rangle \cos(\Phi)), \end{aligned} \quad (3.83)$$

where $\beta_l = k_z/k^0$, $\beta_\perp = k_\perp/k^0$ and $\Phi = \angle(\vec{k}_\perp, \vec{b})$ is the azimuthal angle of the pair three-momentum \vec{k} with respect to the reaction plane z - x determined by the longitudinal direction and the direction of the impact parameter vector $\vec{b} = (x, 0, 0)$; the space-time coordinates \tilde{x}^μ are defined relative to the effective source center $\langle x^\mu \rangle$: $\tilde{x}^\mu = x^\mu - \langle x^\mu \rangle$. The averages are taken with the source emission function $S(t, \vec{x}, k)$, [91]:

$$\langle f(t, \vec{x}) \rangle = \frac{\int d^4x f(t, \vec{x}) S(t, \vec{x}, k)}{\int d^4x S(t, \vec{x}, k)}. \quad (3.84)$$

The illustrative calculations of the correlation radii as a function of the azimuthal angle Φ were done with the following fast MC parameters: $T^{\text{th}} = 0.1$ GeV, $\rho_u^{\text{max}}(b=0) = 1.0$; $R(b=0) = 11.5$ fm, $\tau = 7.5$ fm/ c , $\Delta\tau = 0$. fm/ c , $\epsilon = 0.1$ and $\delta = 0.25$. The azimuthal dependence of the correlation radii in different k_t intervals is shown in Fig. 3.14.

The R_s^2 oscillates downward, in the same phase as "RHIC" source extended out of plane [100], which means the larger sideward radius viewed from the x -direction (in the reaction plane), than from y -direction (out-of plane). The source has small coordinate asymmetry $\epsilon = 0.1$, it is almost round (as in Fig. 3.8 step 3), however the emission zone, or "homogeneity region", varies with Φ because of the non-isotropic flow.

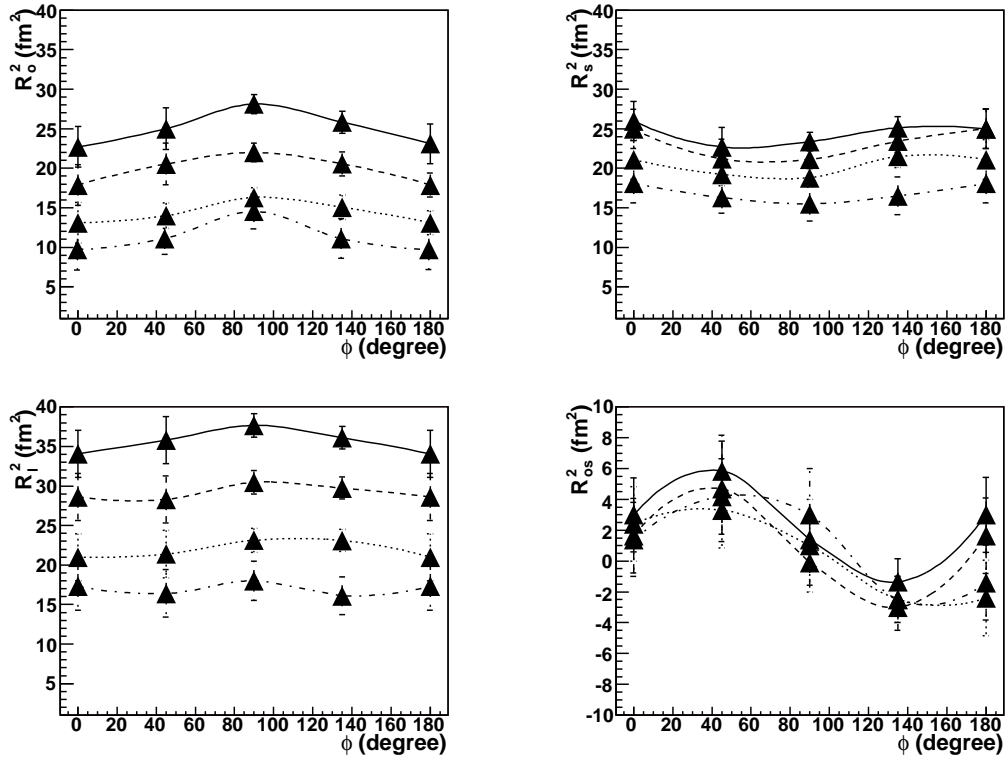


Figure 3.14: Simulated with FASTMC squared correlation radii versus the azimuthal angle Φ of the $\pi^+\pi^+$ pair with respect to the reaction plane, 20-30 % centrality events in k_T (GeV/c) intervals: $0.15 < k_T < 0.25$ (solid line), $0.25 < k_T < 0.35$ (dashed line), $0.35 < k_T < 0.45$ (dotted line), $0.45 < k_T < 0.60$ (dotted-dashed line). simulation was done with the special set of parameters: $T^{\text{th}} = 0.1$ GeV, $\rho_u^{\text{max}}(b = 0) = 1.0$; $R(b = 0) = 11.5$ fm, $\tau = 7.5$ fm/c, $\Delta\tau = 0$. fm/c, $\epsilon = 0.1$ and $\delta = 0.25$, weak decays were not taken into account.

3.12 Conclusions

A MC simulation procedure is developed as well as corresponding C++ code, that allows a fast realistic description of multiple hadron production both in central and noncentral relativistic heavy ion collisions. A high generation speed and an easy control through input parameters make our MC generator code particularly useful for detector studies. As options, we have implemented two freeze-out scenarios with coinciding and with different chemical and thermal freeze-outs. We have compared the RHIC experimental data with our MC generation results obtained within the single and separated freeze-out scenarios with Bjorken-like freeze-out surface parameterization.

Fixing the temperatures of the chemical and thermal freeze-out at 0.165 GeV and 0.100 GeV respectively, and, using the same set of the model parameters as for the central collisions, we have described single particle spectra at different centralities with the absolute normalization correct within $\sim 13\%$.

The comparison of the RHIC v_2 measurements with our MC generation results shows that the scenario with two separated freeze-outs is more favorable for the description of the p_t -dependence of the elliptic flow.

The description of the k_t -dependence of the correlation radii has been achieved within $\sim 10\%$ accuracy. The experimentally observed values of the correlation strength parameter λ has been reproduced due to the account of the weak decays.

The analysis of the azimuthal dependence of the correlation radii indicates that the source considered in the model oscillates downward, in the same phase as "RHIC" source extended out of plane.

The achieved understanding of the reasons leading to a good simultaneous description of particle spectra, elliptic flow and femtoscopic correlations within the considered simple model could be useful for building of the complete dynamic picture of the matter evolution in A+A collisions, like presented in the next chapters.

Hybrid model

The material presented in this chapter is a continuation of studies towards building realistic dynamical models for matter evolution in ultrarelativistic A+A collisions. The model presented here is a truly dynamical model, based on numerical solution of equations of relativistic hydrodynamics, together with microscopic initial state model and UrQMD code for final stage. The realistic features of ultrarelativistic heavy ion collisions are included in the model, and lead to a good description of wide range of experimental data collected in 200A GeV Au+Au collisions at RHIC.

4.1 Introduction

In this chapter, we present a realistic treatment of the hydrodynamic evolution of ultrarelativistic heavy ion collisions. The present model has several improvements compared to existing ones:

- initial conditions obtained from a flux tube approach (EPOS) [141], compatible with the string model used since many years for elementary collisions (electron-positron, proton proton), and the color glass condensate picture;
- consideration of the possibility to have a (moderate) initial collective transverse flow;
- event-by-event procedure, taking into the account the highly irregular space structure of single events.
- core-corona separation [149], considering the fact that only a part of the matter thermalizes;

- use of an efficient code for solving the hydrodynamic equations in 3+1 dimensions, including the conservation of baryon number, strangeness, and electric charge;
- employment of a realistic equation-of-state, compatible with lattice gauge results – with a cross-over transition from the hadronic to the plasma phase;
- use of a complete hadron resonance table, making our calculations compatible with the results from statistical models;
- hadronic cascade procedure (UrQMD) [155] after hadronization from the thermal system at an early stage.

All the above mentioned features are not new, what is new is the attempt to put all these elements into a single approach, bringing together topics like statistical hadronization, flow features, saturation, the string model, and so on, which are often discussed independently. For any quantitative analysis of heavy ion results we have to admit that there is just one common mechanism, which accounts for the whole soft physics. We therefore test our approach by comparing to all essential observables in Au-Au scatterings at RHIC.

Starting from the flux-tube initial condition from EPOS [141], the system expands very rapidly, thanks to the realistic cross-over equation-of-state, flow (also elliptical one) develops earlier compared to the case of a strong first order equation-of-state as in [115, 116], temperatures corresponding to the cross-over (around 170 MeV) are reached in less than 10 fm/c. The system hadronizes in the cross-over re-

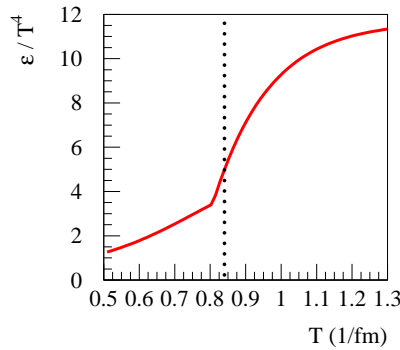


Figure 4.1: The energy density over T^4 as a function of the temperature T . The dotted line indicates the “hadronization temperature”, i.e. end of the thermal phase, when “matter” is transformed into hadrons.

gion, where here “hadronization” is meant to be the end of the completely thermal phase: matter is transformed into hadrons. We stop the hydrodynamical evolution

at this point, but particles are not yet free. Our favorite hadronization temperature is 166 MeV, shown as the dotted line in fig. 4.1, which is indeed right in the transition region, where the energy density varies strongly with temperature. At this point we employ statistical hadronization, which should be understood as hadronization of the quark-gluon plasma state into a hadronic system, at an early stage, not the decay of a resonance gas in equilibrium.

Particle production seems to be governed by statistical hadronization in the framework of an ideal resonance gas, with a hadronization temperatures T_H close to 170 MeV [108, 109, 110, 223, 111, 112, 113], which corresponds to the critical temperature of the (cross-over) transition between the resonance gas and the quark gluon plasma. Such a high temperature is in particular necessary to accommodate the yields of heavy particles like baryons and antibaryons. Thus, we consider an early “chemical freeze-out” $T_{\text{ch}} \approx T_H$, and then force the particle yields to stay constant till the final “thermal freeze-out” T_{th} [114].

After this hadronization –although no longer thermal– the system still interacts via hadronic scatterings, still building up (elliptical) flow, but much less compared to an idealized thermal resonance gas evolution, which does not exist in reality.

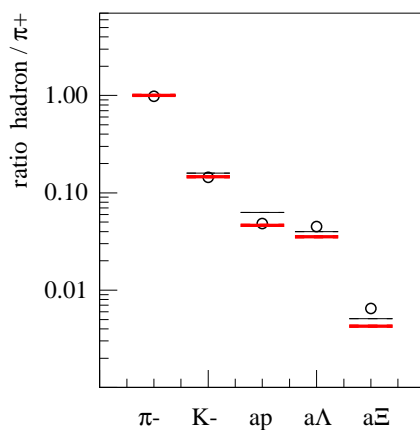


Figure 4.2: Particle ratios (hadron yields to π^+ yields) from our model calculations (thick horizontal line) as compared to the statistical model [108] (thin horizontal line), and to data [138, 139, 140] (points).

Despite the non-equilibrium behavior in the finale stage of the collision, our sophisticated procedure gives particle yields close to what has been predicted in statistical models, see fig. 4.2.

This is because the final hadronic cascade does not change particle yields too much (with some exceptions to be discussed later), but it affects slopes and –as mentioned– azimuthal asymmetry observables.

In the following, we will present the details of our realistic approach to the hydrodynamic evolution in heavy ion collisions. In the present thesis, the hydrodynamic evolution is brought to a focus, for more details see [102].

4.2 Initial state model : EPOS

The initial state approach is called EPOS, which stands for

- Energy conserving quantum mechanical multiple scattering approach, based on
- Partons (parton ladders)
- Off-shell remnants
- Splitting of parton ladders

We are going to explain the different items in the following.

One may consider the simple parton model to be the basis of hadron-hadron interaction models at high energies. It is well known that the inclusive cross section is given as a convolution of two parton distribution functions with an elementary parton-parton interaction cross section. The latter one is obtained from perturbative QCD, the parton distributions are deduced from deep inelastic scattering. Although these distributions are taken as black boxes, one should not forget that they represent a dynamical process, namely the successive emission of partons (initial state space-like cascade), which have to be considered in a complete picture. In addition, the produced partons are generally off-shell, giving rise again to parton emissions (final state time-like cascade). All this is sketched in fig. 4.3, where we also indicate that we refer to this whole structure as “parton ladder”, with a corresponding simple symbol, to simplify further discussion.

For practical calculations, each parton ladder is finally translated into two color strings, which fragment into hadrons. This is a purely phenomenological procedure for the non-perturbative hadronization process.

Actually our “parton ladder” is meant to contain two parts: the hard one, as discussed above, and a soft one, which is a purely phenomenological object, parametrized in Regge pole fashion.

Still the picture is not complete, since so far we just considered two interacting partons, one from the projectile and one from the target. These partons leave behind a projectile and target remnant, colored, so it is more complicated than simply projectile/target deceleration. One may simply consider the remnants to be diquarks, providing a string end, but this simple picture seems to be excluded from strange antibaryon results at the SPS [101].

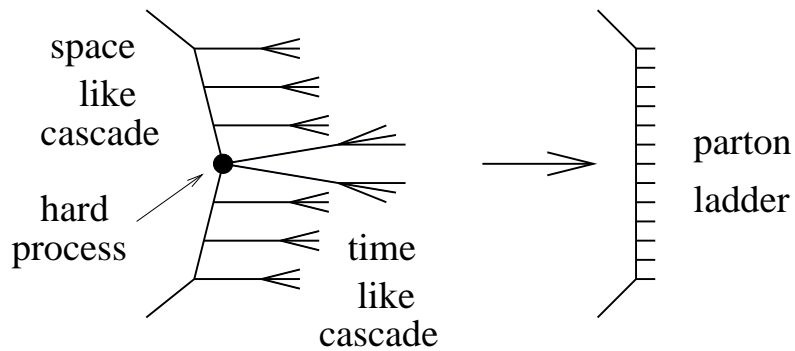


Figure 4.3: Elementary parton-parton scattering: the hard scattering in the middle is preceded by parton emissions (initial state space-like cascade); these partons being usually off-shell, they emit further partons (final state time-like cascade). For all this we use a symbolic parton ladder.

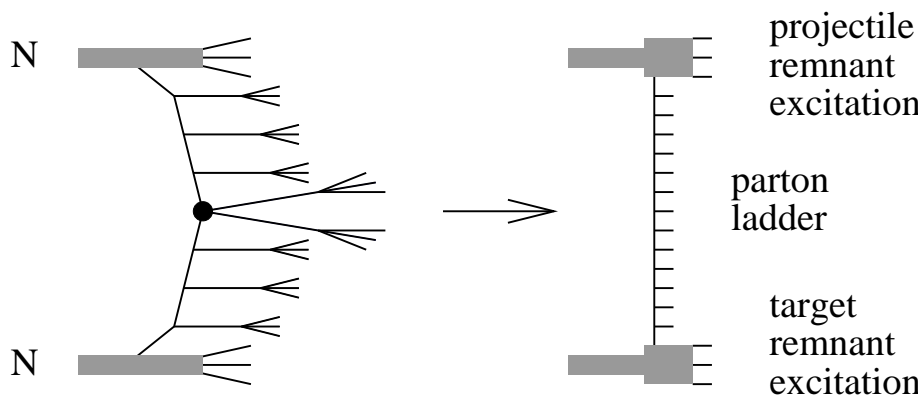


Figure 4.4: The complete picture, including remnants. The remnants are an important source of particle production at RHIC energies.

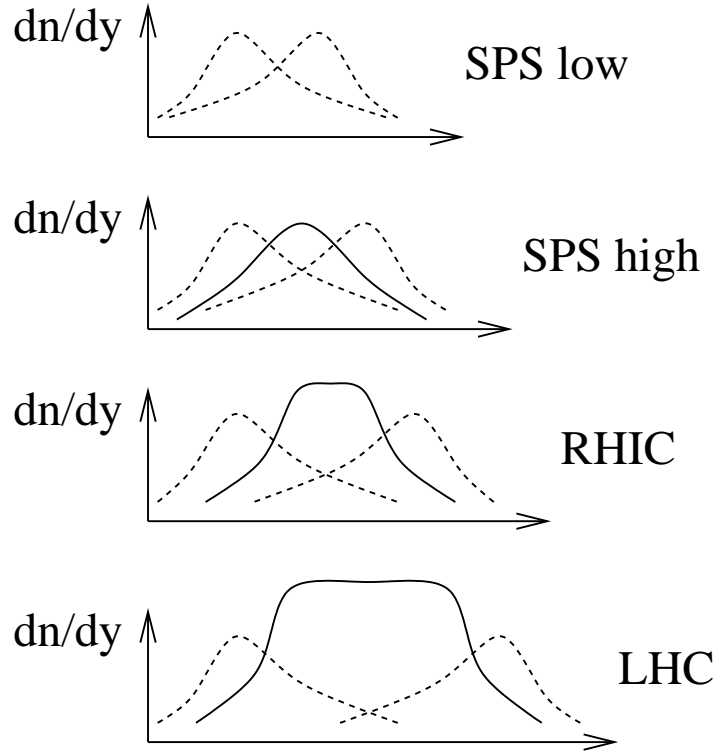


Figure 4.5: Inner contributions, from the parton ladder (full lines), and “outer” contributions, from the remnants (dashed lines), to the rapidity distribution of hadrons. (Artists view)

We therefore adopt the following picture, as indicated in fig. 4.4: not only a quark, but a two-fold object takes directly part in the interaction, being a quark-antiquark, or a quark-diquark, leaving behind a colorless remnant, which is, however, in general excited (off-shell). So we have finally three “objects”, all being white: the two off-shell remnants, and the parton ladders between the two active “partons” on either side (by “parton” we mean quark, antiquark, diquark, or antidiquark). We also refer to “inner contributions” (from parton ladders) and “outer contributions” (from remnants), reflecting the fact that the remnants produce particles mainly at large rapidities and the parton ladders at central rapidities, see fig. 4.5. Whereas the outer contributions are essentially energy independent, apart of a shift in rapidity, the inner contributions grows with energy, to eventually dominate completely central rapidities. But at RHIC, there is still a substantial remnant contribution at mid-rapidity.

Even inclusive measurements require often more information than just inclusive cross sections, for example via trigger conditions. Anyhow, for detailed com-

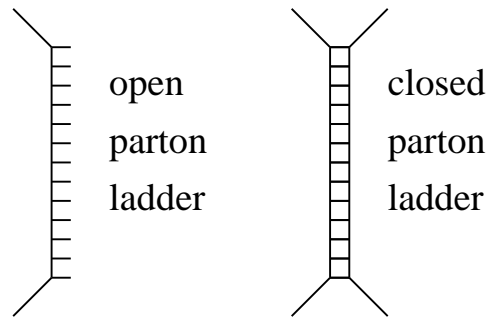


Figure 4.6: The two elements of the multiple scattering theory: open ladders, representing inelastic interactions, and closed ladders, representing elastic interactions.

parisons we need an event generator, which obviously requires information about exclusive cross sections (the widely used pQCD generators are not event generators in this sense, they are generators of inclusive spectra, and a Monte Carlo event is not a physical event). This problem is known since many years, the solution is Gribov’s multiple scattering theory, employed since by many authors. This formulation is equivalent to using the eikonal formula to obtain exclusive cross sections from the knowledge of the inclusive one.

We indicated recently inconsistencies in this approach, proposing an “energy conserving multiple scattering treatment”. The main idea is simple: in case of multiple scattering, when it comes to calculating partial cross sections for double, triple ... scattering, one has to explicitly care about the fact that the total energy has to be shared among the individual elementary interactions.

A consistent quantum mechanical formulation requires not only the consideration of the (open) parton ladders, discussed so far, but also of closed ladders, representing elastic scattering, see fig. 4.6. The closed ladders do not contribute to particle production, but they are crucial since they affect substantially the calculations of partial cross sections. Actually, the closed ladders simply lead to large numbers of interfering contributions for the same final state, all of which have to be summed up to obtain the corresponding partial cross sections.

We can do the complicated calculations, since we fit for example the result of a numerical calculation of a squared amplitude corresponding to a (open) parton ladder of energy \sqrt{s} , using a simple form αs^β , which allows then to perform analytical calculations. Furthermore, we employ very sophisticated Markov chain techniques to generate configurations according to multidimensional probability distributions.

Important concerning numerical results: There are a couple of parameters which determine the parameterization of the soft elementary interaction (soft Pomeron), which are essentially fixed to get the pp cross sections right. The pQCD parameters (soft virtuality cutoff, K-factor, parton emission cutoff, parton-hadron coupling) are fixed to provide a reasonable parton distribution function (which we calculate, it is not input!).

We assume the remnants to be off-shell with probability p_O , a mass distribution given as

$$\text{prob} \propto M^{-2\alpha_O}, \quad (4.1)$$

with parameter values which are not necessarily the same for diffractive and non-diffractive interactions (the latter ones being defined to be those without parton ladders). We use currently for p_O 0.75 (dif) and 0.95 (nondif), and for α_O 0.75 (dif) and 1.1 (nondif). Those excitation exponents may give rise to quite high mass remnants, RHIC and also SPS data seem to support this. High mass remnants will be treated as strings.

There are four important fragmentation parameters: the break probability (per unit space-time area) p_B , which determines whether a string breaks earlier or later, the diquark break probability p_D , the strange break probability p_S , and the mean transverse momentum \bar{p}_t of a break, with obvious consequences for baryon and strangeness production, and the p_t of the produced hadrons. We use three sets of these parameters, for the three types of strings: soft-, kinky(hard)-, remnant-strings. We do not really use the full freedom of these parameters, but one single set would not work – if we are interested in high precision. Somewhat surprising: p_S is 0.14 for soft and 0.06 for kinky strings. Maybe this reflects the fact that soft strings may have low masses, where strangeness is suppressed, and which needs some compensation. The parameter p_D is as well bigger for soft compared to kinky strings.

4.3 Hydrodynamic evolution, realistic equation-of-state

Having fixed the initial conditions, the core evolves according to the equations of ideal hydrodynamics, namely the local energy-momentum conservation

$$\partial_\mu T^{\mu\nu} = 0, \quad \nu = 0, \dots, 3, \quad (4.2)$$

and the conservation of net charges,

$$\partial N_k^\mu = 0, \quad k = B, S, Q, \quad (4.3)$$

with B , S , and Q referring to respectively baryon number, strangeness, and electric charge. In this thesis we treat ideal hydrodynamic, so we use the decomposition

$$T^{\mu\nu} = (\epsilon + p) u^\mu u^\nu - p g^{\mu\nu}, \quad (4.4)$$

$$N_k^\mu = n_k u^\mu, \quad (4.5)$$

where u is the four-velocity of the local rest frame. Solving the equations, as discussed above, provides the evolution of the space-time dependence of the macroscopic quantities energy density $\epsilon(x)$, collective flow velocity $\vec{v}(x)$, and the net flavor densities $n_k(x)$. Here, the crucial ingredient is the equation of state, which closes the set of equations by providing the ϵ -dependence of the pressure p . The equation-of-state should fulfill the following requirements:

- flavor conservation, using chemical potentials μ_B , μ_S , μ_Q ;
- compatibility with lattice gauge results in case of $\mu_B = \mu_S = \mu_Q = 0$.

The starting point for constructing this “realistic” equation-of-state is the pressure p_H of a resonance gas, and the pressure p_Q of an ideal quark gluon plasma, including bag pressure. Be T_c the temperature where p_H and p_Q cross. The correct pressure is assumed to be of the form

$$p = p_Q + \lambda (p_H - p_Q), \quad (4.6)$$

where the temperature dependence of λ is given as

$$\lambda = \exp\left(-\frac{T - T_c}{\delta}\right) \Theta(T - T_c) + \Theta(T_c - T), \quad (4.7)$$

with

$$\delta = \delta_0 \exp\left(-(\mu_B/\mu_c)^2\right) \left(1 + \frac{T - T_c}{2T_c}\right). \quad (4.8)$$

From the pressure one obtains the entropy density S as

$$S = \frac{\partial p}{\partial T} = S_Q + \lambda (S_H - S_Q) + \frac{\partial \lambda}{\partial T} (p_H - p_Q), \quad (4.9)$$

and the flavor densities n^i as

$$n^i = \frac{\partial p}{\partial \mu^i} = n_Q^i + \lambda (n_H^i - n_Q^i) + \frac{\partial \lambda}{\partial \mu^i} (p_H - p_Q). \quad (4.10)$$

The energy density is finally given as

$$\varepsilon = TS + \sum_i \mu^i n^i - p, \quad (4.11)$$

or

$$\varepsilon = \varepsilon_Q + \lambda(\varepsilon_H - \varepsilon_Q) + \left(T \frac{\partial \lambda}{\partial T} + \mu^i \frac{\partial \lambda}{\partial \mu^i} \right) (p_H - p_Q). \quad (4.12)$$

Our favorite equation-of-state, referred to as “X3F”, is obtained for $\delta_0 = 0.15$, which reproduces lattice gauge results for $\mu_B = \mu_S = \mu_Q = 0$, as shown in figs. 4.7 and 4.8.

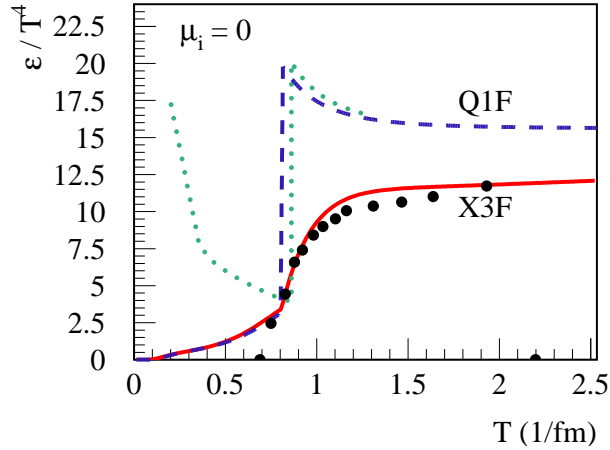


Figure 4.7: Energy density versus temperature, for our equation-of-state X3F (full line), compared to lattice data [154] (points), and some other EoS choices, see text.

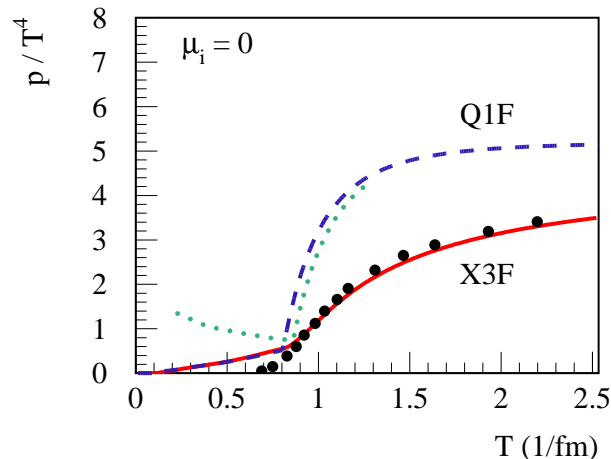


Figure 4.8: Pressure versus temperature, for our equation-of-state X3F (full line), compared to lattice data [154] (points), and some other EoS choices, see text.

The symbol X3F stands for “cross-over” and “3 flavor conservation”. Also shown in the figures is the EoS Q1F, referring to a simple first order equation-of-state, with baryon number conservation, which we will use as a reference to compare with. Many current calculations are still based on this simple choice, as for example the one in [115, 116], shown as dotted lines in figs. 4.7 and 4.8.

In the next subsections, the details of the equation of state are described.

4.3.1 Hydrodynamic algorithm

The algorithm is based on the Godunov method: one introduces finite cells and computes fluxes between cells using the (approximate) Riemann problem solution for each cell boundary. A relativistic HLLC solver is used to solve the Riemann problem. To achieve more accuracy in time, a predictor-corrector scheme is used for the second order of accuracy in time, i.e. the numerical error is $O(dt^3)$, instead of $O(dt^2)$. To achieve more accuracy in space, namely a second order scheme, the linear distributions of quantities (conservative variables) inside cells are used. The conservative quantities are $(e + p * v^2)/(1 - v^2)$, $(e + p) * v/(1 - v^2)$.

We rewrite equations in hyperbolic coordinates. These coordinates are suitable for the dynamical description at ultrarelativistic energies. It is convenient to write

the equations in conservative form, the conservative variables are

$$\vec{Q} = \begin{pmatrix} Q_\tau \\ Q_x \\ Q_y \\ Q_\eta \\ Q_B \\ Q_S \\ Q_Q \end{pmatrix} = \begin{pmatrix} \gamma^2(\epsilon + p) - p \\ \gamma^2(\epsilon + p)v_x \\ \gamma^2(\epsilon + p)v_y \\ \gamma^2(\epsilon + p)v_\eta \\ \gamma n_B \\ \gamma n_S \\ \gamma n_Q \end{pmatrix}, \quad (4.13)$$

where n_B , n_S , n_Q are the densities of the conserved quantities B , S , and Q . The components Q_m are conservative variables in the sense that the integral (discrete sum over all cells) of Q_m gives the total energy, momentum, and the total B , S , and Q , which are conserved up to the fluxes at the grid boundaries. The velocities in these expressions are defined in the ‘‘Bjorken frame’’ related to velocities in laboratory frame as

$$\begin{aligned} v_x &= v_x^{\text{lab}} \cdot \frac{\cosh y}{\cosh(y - \eta_s)} \\ v_y &= v_y^{\text{lab}} \cdot \frac{\cosh y}{\cosh(y - \eta_s)} \\ v_\eta &= \tanh(y - \eta_s) \end{aligned} \quad (4.14)$$

where $y = \frac{1}{2} \ln[(1 + v_z^{\text{lab}})/(1 - v_z^{\text{lab}})]$ is the longitudinal rapidity of the fluid element, $\eta_s = \frac{1}{2} \ln[(t + z)/(t - z)]$ is space-time rapidity. The full hydrodynamical equations are then

$$\underbrace{\partial_\tau \begin{pmatrix} Q_\tau \\ Q_x \\ Q_y \\ Q_\eta \\ Q_B \\ Q_S \\ Q_Q \end{pmatrix}}_{\text{quantities}} + \underbrace{\vec{\nabla} \cdot \begin{pmatrix} Q_\tau \\ Q_x \\ Q_y \\ Q_\eta \\ Q_B \\ Q_S \\ Q_Q \end{pmatrix}}_{\text{fluxes}} + \underbrace{\begin{pmatrix} \vec{\nabla}(p \cdot \vec{v}) \\ \partial_x p \\ \partial_y p \\ \frac{1}{\tau} \partial_\eta p \\ 0 \\ 0 \\ 0 \end{pmatrix}}_{\text{sources}} + \underbrace{\begin{pmatrix} (Q_\tau + p)(1 + v_\eta^2)/\tau \\ Q_x/\tau \\ Q_y/\tau \\ 2Q_\eta/\tau \\ Q_B/\tau \\ Q_S/\tau \\ Q_Q/\tau \end{pmatrix}}_{\text{sources}} = 0 \quad (4.15)$$

with $\vec{\nabla} = (\partial_x, \partial_y, \frac{1}{\tau} \partial_\eta)$.

We base our calculations on the finite-volume approach : we discretize the system on a fixed grid in the calculational frame and interpret $Q_{m,ijk}^n$ as average value over some space interval ΔV_{ijk} , which is called a cell. The index n refers to the discretized time.

The values of $Q_{m,ijk}^n$ are then updated after each time-step according to the fluxes on the cell interface during the time-step Δt_n . One has the following update formula :

$$\begin{aligned} Q_{m,ijk}^{n+1} = & Q_{m,ijk}^n - \frac{\Delta t}{\Delta x_1} (F_{(i+1/2),jk} + F_{(i-1/2),jk}) \\ & - \frac{\Delta t}{\Delta x_2} (F_{i,(j+1/2),k} + F_{i,(j-1/2),k}) \\ & - \frac{\Delta t}{\Delta x_3} (F_{ij,(k+1/2)} + F_{ij,(k-1/2)}), \end{aligned} \quad (4.16)$$

where F is the average flux over the cell boundary, the indexes $+1/2$ and $-1/2$ correspond to the right and the left cell boundary in each direction. This is the base of the Godunov method [192], which also implies that the distributions of variables inside a cell are piecewise linear (or piecewise parabolic etc, depending on the order of the numerical scheme), which forms a Riemann problem at each cell interface. Then the flux through each cell interface depends only on the solution of a single Riemann problem, supposing that the waves from the neighboring discontinuities do not intersect. The latter is satisfied with the Courant-Friedrichs-Lewy (CFL) condition [193].

To solve the Riemann problems at each cell interface, we use the relativistic HLLE solver [194], which approximates the wave profile in the Riemann problem by a single intermediate state between two shock waves propagating away from the initial discontinuity. Together with the shock wave velocity estimate, in this approximation one can obtain an analytical dependence of the flux on the initial conditions for the Riemann problem, which makes the algorithm explicit.

We proceed then to construct a higher-order numerical scheme:

- in time: the *predictor-corrector* scheme is used for the second order accuracy in time, i.e. the numerical error is $O(dt^3)$, instead of $O(dt^2)$
- in space: in the same way, to achieve the second order scheme, the *linear distributions* of quantities (conservative variables) inside cells are used.

Some final remarks:

At each time-step, we compute and sum the fluxes for each cell with all its neighbors and update the value of conservative variables with the total flux. Thus, we do not use operator splitting (dimensional splitting) and thus avoid the numerical artifacts introduced by this method, e.g. artificial spatial asymmetry.

To treat grid boundaries, we use the method of *ghost cells*. We include 2 additional cells on either end of grid in each direction, and set the quantities in these cells at the beginning of each time-step. For simplicity, we set the quantities

in ghost cells to be equal to these in the nearest "real" cell, thus implementing non-reflecting boundary conditions (outflow boundary). This physically correspond to boundary which does not reflect any wave, which is consistent with expansion into vacuum.

In our simulations we deal with spatially finite systems expanding into vacuum. Thus the computational grid in Eulerian algorithm must initially contain both system and surrounding vacuum. To account for the finite velocity of the expansion into the vacuum, which equals c for an infinitesimal slice of matter on the boundary, we introduce additional (floating-point) variables in each cell which keep the extent of matter expansion within a cell, having the value unity for the complete cell, zero for a cell with vacuum only. The matter is allowed to expand in the next vacuum cell only if the current cell is filled with matter.

4.3.2 Resonance gas

Whereas for hadronization we employ the correct quantum statistics, we use the Boltzmann approximation for the calculation of the equation of state. This is reasonable even for pions at zero chemical potential, the excluded volume correction at nonzero chemical potentials is considerably bigger than the difference coming from quantum statistical treatment. We account for all well known hadrons made from u, d, s quarks from the PDG table For energy density, pressure and net charges we get :

$$\epsilon = \sum_i \frac{g_i}{2\pi^2} m_i^2 T \left[3T K_2\left(\frac{m_i}{T}\right) + \frac{m_i}{2} K_1\left(\frac{m_i}{T}\right) \right] \exp(\mu_i/T) \quad (4.17)$$

$$p = \sum_i \frac{g_i}{2\pi^2} m_i^2 T^2 \cdot K_2\left(\frac{m_i}{T}\right) \cdot \exp(\mu_i/T) \quad (4.18)$$

$$n_B = \sum_i B_i \frac{g_i}{2\pi^2} m_i^2 T \cdot K_2\left(\frac{m_i}{T}\right) \cdot \exp(\mu_i/T) \quad (4.19)$$

$$n_Q = \sum_i Q_i \frac{g_i}{2\pi^2} m_i^2 T \cdot K_2\left(\frac{m_i}{T}\right) \cdot \exp(\mu_i/T) \quad (4.20)$$

$$n_S = \sum_i S_i \frac{g_i}{2\pi^2} m_i^2 T \cdot K_2\left(\frac{m_i}{T}\right) \cdot \exp(\mu_i/T) \quad (4.21)$$

with

$$\mu_i = B_i \mu_B + Q_i \mu_Q + S_i \mu_S, \quad (4.22)$$

where μ_B , μ_S , μ_Q are the chemical potentials associated to B , S , Q , and B_i , S_i , Q_i are the baryon charge, strangeness, and the electric charge of i -th hadron state, $g_i = (2J_i + 1)$ is degeneracy factor.

For large baryon chemical potential the EoS correction for the deviations from ideal gas due to particle interactions becomes more important. We employ this correction in a form of an excluded volume effect, like a Van der Waals hard core correction. According to this prescription,

$$p(T, \mu_B, \mu_Q, \mu_S) = \sum_i p_i^{\text{boltz}}(T, \tilde{\mu}_i), \quad (4.23)$$

$$\tilde{\mu}_i = \mu_i - v_i \cdot p. \quad (4.24)$$

If one supposes equal volume $v_i = v$ for all particle species, then the correction can be computed as a solution $p(T, \mu_B, \mu_Q, \mu_S)$ of a fairly simple, however transcendental equation,

$$p(T, \mu_B, \mu_Q, \mu_S) = p^{\text{boltz}}(T, \mu_B, \mu_Q, \mu_S) e^{-vp(T, \mu_B, \mu_Q, \mu_S)/T} \quad (4.25)$$

We take the value $v \approx 1.44 \text{ fm}^3$, which corresponds to the hard core radius $r = 0.7 \text{ fm}$.

4.3.3 Ideal QGP

In this ideal phase, matter is made from massless u, d quarks and massive s -quark (+antiquarks). Due to the possibility of a large strange quark chemical potential, comparable to its mass $m_s = 120 \text{ MeV}$ which is taken in our calculations, we perform the integration of the strange quark contribution to thermodynamic quantities exactly, without Boltzmann or zero-mass approximation. So we have

$$\begin{aligned} p = & \frac{g_l}{6\pi^2} \left[\frac{1}{4}\mu_u^4 + \frac{\pi^2}{2}\mu_u^2 T^2 + \frac{7\pi^4 T^4}{60} \right] \\ & + \frac{g_l}{6\pi^2} \left[\frac{1}{4}\mu_d^4 + \frac{\pi^2}{2}\mu_d^2 T^2 + \frac{7\pi^4 T^4}{60} \right] + \\ & + p_s(T, \mu_s) + p_{\bar{s}}(T, \mu_s) + \frac{gg\pi^2}{90} T^4 - B, \end{aligned} \quad (4.26)$$

with $p_{\bar{s}}(T, \mu_s) = p_s(T, -\mu_s)$, and

$$p_s(T, \mu_s) = \frac{g_l T}{2\pi^2} \int_0^\infty p^2 \ln \left[1 + \exp \left(\frac{1}{T} \sqrt{p^2 + m_s^2} + \frac{\mu_s}{T} \right) \right] dp, \quad (4.27)$$

where we use the degeneracy factors $g_l = 6$ for light quarks, $g_g = 16$ for gluons, and a bag constant $B = 0.38 \text{ GeV}/\text{fm}^3$. Quark chemical potentials are

$$\mu_u = \frac{1}{3}\mu_B + \frac{2}{3}\mu_Q, \quad (4.28)$$

$$\mu_d = \frac{1}{3}\mu_B - \frac{1}{3}\mu_Q, \quad (4.29)$$

$$\mu_s = \frac{1}{3}\mu_B - \frac{1}{3}\mu_Q - \mu_S. \quad (4.30)$$

Using the relations $n_i = \partial p / \partial \mu_i$, $s = \partial p / \partial T$, $\varepsilon = Ts + \sum \mu_i n_i - p$, we get

$$\varepsilon = 3(p - p_s - p_{\bar{s}} + B) + \varepsilon_s + \varepsilon_{\bar{s}} + B \quad (4.31)$$

$$\begin{aligned} n_B &= \frac{1}{3} \frac{g_l}{6\pi^2} [\mu_u^3 + \pi^2 \mu_u T^2 + \mu_d^3 + \pi^2 \mu_d T^2] + \\ &+ \frac{1}{3} [n_s(T, \mu_s) - n_{\bar{s}}(T, -\mu_s)] \end{aligned} \quad (4.32)$$

$$\begin{aligned} n_Q &= \frac{1}{3} \frac{g_l}{6\pi^2} [2\mu_u^3 + 2\pi^2 \mu_u T^2 - \mu_d^3 - \pi^2 \mu_d T^2] - \\ &- \frac{1}{3} [n_s(T, \mu_s) - n_{\bar{s}}(T, -\mu_s)] \end{aligned} \quad (4.33)$$

$$n_S = -[n_s(T, \mu_s) - n_{\bar{s}}(T, -\mu_s)] \quad (4.34)$$

with $\varepsilon_{\bar{s}}(T, \mu_s) = \varepsilon_s(T, -\mu_s)$, and

$$\varepsilon_s(T, \mu_s) = \frac{g_l}{2\pi^2} \int_0^\infty \frac{p^2 \sqrt{p^2 + m_s^2}}{\exp\left(\frac{1}{T} \sqrt{p^2 + m_s^2} - \frac{\mu_s}{T}\right) + 1} dp, \quad (4.35)$$

$$n_s(T, \mu_s) = \frac{g_l}{2\pi^2} \int_0^\infty \frac{p^2}{\exp\left(\frac{1}{T} \sqrt{p^2 + m_s^2} - \frac{\mu_s}{T}\right) + 1} dp. \quad (4.36)$$

4.4 Freeze-out

When the evolution reaches the hadronization hypersurface, defined by a given temperature T_H , we switch from ‘‘matter’’ description to particles, using the Cooper-Frye description. Particles may still interact, as discussed below, so hadronization here means an intermediate stage, particles are not yet free streaming, but they are not thermalized any more.

We parametrize the hadronization hyper-surface $x^\mu = x^\mu(\tau, \varphi, \eta)$ as

$$x^0 = \tau \cosh \eta, \quad x^1 = r \cos \varphi, \quad x^2 = r \sin \varphi, \quad x^3 = \tau \sinh \eta, \quad (4.37)$$

with $r = r(\tau, \varphi, \eta)$ being some function of the three parameters τ, φ, η . The hypersurface element is

$$d\Sigma_\mu = \varepsilon_{\mu\nu\kappa\lambda} \frac{\partial x^\nu}{\partial \tau} \frac{\partial x^\kappa}{\partial \varphi} \frac{\partial x^\lambda}{\partial \eta} d\tau d\varphi d\eta, \quad (4.38)$$

with $\varepsilon^{\mu\nu\kappa\lambda} = -\varepsilon_{\mu\nu\kappa\lambda} = 1$. Computing the partial derivatives $\partial x^\mu / d\alpha$, with $\alpha = \tau, \varphi, \eta$, one gets

$$d\Sigma_0 = \left\{ -r \frac{\partial r}{\partial \tau} \tau \cosh \eta + r \frac{\partial r}{\partial \eta} \sinh \eta \right\} d\tau d\varphi d\eta, \quad (4.39)$$

$$d\Sigma_1 = \left\{ \frac{\partial r}{\partial \varphi} \tau \sin \varphi + r \tau \cos \varphi \right\} d\tau d\varphi d\eta, \quad (4.40)$$

$$d\Sigma_2 = \left\{ -\frac{\partial r}{\partial \varphi} \tau \cos \varphi + r \tau \sin \varphi \right\} d\tau d\varphi d\eta, \quad (4.41)$$

$$d\Sigma_3 = \left\{ r \frac{\partial r}{\partial \tau} \tau \sinh \eta - r \frac{\partial r}{\partial \eta} \cosh \eta \right\} d\tau d\varphi d\eta. \quad (4.42)$$

Cooper-Frye hadronization amounts to calculating

$$E \frac{dn}{d^3p} = \int d\Sigma_\mu p^\mu f(up),$$

with u being the flow four-velocity in the global frame, which can be expressed in terms of the four-velocity \tilde{u} in the ‘‘Bjorken frame’’ as

$$u^0 = \tilde{u}^0 \cosh \eta + \tilde{u}^3 \sinh \eta, \quad (4.43)$$

$$u^1 = \tilde{u}^1, \quad (4.44)$$

$$u^2 = \tilde{u}^2, \quad (4.45)$$

$$u^3 = \tilde{u}^0 \sinh \eta + \tilde{u}^3 \cosh \eta. \quad (4.46)$$

In a similar way one may express p in terms of \tilde{p} in the Bjorken frame. Using $\gamma = \tilde{u}^0$ and the flow velocity $v^\mu = \tilde{u}^\mu / \gamma$, we get

$$\frac{dn}{dy d\phi dp_\perp} = \quad (4.47)$$

$$p_\perp \int \left\{ -r \frac{\partial r}{\partial \tau} \tau \tilde{p}^0 + r \tau \tilde{p}^r + \frac{\partial r}{\partial \varphi} \tau \tilde{p}^t - r \frac{\partial r}{\partial \eta} \tilde{p}^3 \right\} f(x, p),$$

with $\tilde{p}^r = \tilde{p}^1 \cos \varphi + \tilde{p}^2 \sin \varphi$ and $\tilde{p}^t = \tilde{p}^1 \sin \varphi - \tilde{p}^2 \cos \varphi$ being the radial and the tangential transverse momentum components. Our Monte Carlo generation procedure is based on the invariant volume element moving through the FO surface,

$$dV^* = d\Sigma_\mu u^\mu = w d\tau d\varphi d\eta, \quad (4.48)$$

with

$$w = \gamma \left\{ -r \frac{\partial r}{\partial \tau} \tau + r \tau v^r + \frac{\partial r}{\partial \varphi} \tau v^t - r \frac{\partial r}{\partial \eta} v^3 \right\}, \quad (4.49)$$

and with $v^r = v^1 \cos \varphi + v^2 \sin \varphi$ and $v^t = v^1 \sin \varphi - v^2 \cos \varphi$ being the radial and the tangential transverse flow. Freeze out is done as follows (equivalent to Cooper-Frye): the proposal of isotropic particles production in the local rest frame as

$$dn_i = \alpha d^3 p^* dV^* f_i(E^*), \quad (4.50)$$

is accepted with probability

$$\kappa = \frac{d\Sigma_\mu p^\mu}{\alpha dV^* E^*}. \quad (4.51)$$

In case of acceptance, the momenta are boosted to the global frame.

After the “intermediate” hadronization, the particles at their hadronization positions (on the corresponding hypersurface) are fed into the hadronic cascade model UrQMD [155, 156], performing hadronic interaction until the system is so dilute that no interaction occur any more. The “final” freeze out position of the particles is the last interaction point of the cascade process, or the hydro hadronization position, if no hadronic interactions occurs.

4.5 UrQMD afterburner

The UrQMD-model [155] is a microscopic transport theory based on the covariant propagation of all hadrons on classical trajectories in combination with stochastic binary scatterings, color string formation and resonance decay. It represents a Monte Carlo solution of a large set of coupled partial integro-differential equations for the time evolution of the various phase space densities $f_i(x, p)$ of particle species $i = N, \Delta, \Lambda$, etc., which non-relativistically assumes the Boltzmann form:

$$\frac{df_i(x, p)}{dt} \equiv \frac{\partial p}{\partial t} \frac{\partial f_i(x, p)}{\partial p} + \frac{\partial x}{\partial t} \frac{\partial f_i(x, p)}{\partial x} + \frac{\partial f_i(x, p)}{\partial t} = \text{St} f_i(x, p) \quad , \quad (4.52)$$

where x and p are the position and momentum of the particle, respectively, and $\text{St} f_i(x, p)$ denotes the collision (or rather source-) term of these particle species, which are connected to any other particle species f_k .

The exchange of electric and baryonic charge, strangeness and four momentum in the t -channel is considered for baryon-baryon (BB) collisions at low energies, while meson-baryon (MB) and meson-meson (MM) interactions are treated via the formation and decay of resonances, i.e. the s -channel reactions. t -channel reactions for MB and MM collisions are taken into account from $\sqrt{s} > 3$ GeV on increasing to the only MB, MM interaction type above $\sqrt{s} = 6$ GeV. For nucleus-nucleus collisions the soft binary and ternary interactions between nucleons can

be described by the real part of the in-medium G-Matrix, which is approximated by a non-relativistic density-dependent Skyrme potential of the form

$$V^{Sk} = \frac{1}{2!}t_1 \sum_{i \neq j} \delta(\vec{x}_i - \vec{x}_j) + \frac{1}{3!}t_2 \sum_{i \neq j \neq k} \delta(\vec{x}_i - \vec{x}_j)\delta(\vec{x}_j - \vec{x}_k) \quad , \quad (4.53)$$

where \vec{x}_α denotes the coordinate variable in the quantum phase space. The first term simulates the attractive potential of the NN-interaction, and the second one yields the saturation. In addition, Yukawa and Coulomb potentials are implemented in the model. The potentials allow to calculate the equation of state of the interacting many body system, as long as it is dominated by nucleons. Note that these potential interactions are only used in the model for baryons/nucleons with relative momenta Δp of less than $2 \text{ GeV}/c$. For the hadronic collisions discussed here, the potential interactions are omitted. Further details of the application of the UrQMD model to heavy-ion reactions may be found in [155].

This framework allows to bridge with one concise model the entire available range of energies from the SIS energy region ($\sqrt{s} \approx 2 \text{ GeV}$) to the RHIC energy ($\sqrt{s} = 200 \text{ GeV}$). At the highest energies, a huge number of different particle species can be produced. The model should allow for subsequent rescatterings. The collision term in the UrQMD model includes more than fifty baryon species and five meson nonetts (45 mesons). In addition, their antiparticles have been implemented using charge-conjugation to assure full baryon-antibaryon symmetry. The implemented meson multiplets are: pseudo-scalar, vector, scalar, pseudo-vector and the tensor mesons as well as the heavy vector meson resonances $\rho(1450)$, $\rho(1700)$, $\omega(1420)$, and $\omega(1600)$. Extremely heavy meson resonances ($m > 2 \text{ GeV}$) are not explicitly implemented, however they may be important when investigating, e.g. the dynamics of $\Phi\Phi$ correlations in future experiments.

All particles can be produced in hadron-hadron collisions and can interact further with each other. The different decay channels all nucleon-, Δ - and hyperon-resonances up to $2.25 \text{ GeV}/c^2$ mass as well as the meson (e.g. K^*) decays etc. are implemented. At higher energies we take advantage of the hadron universality and use a string model for the decay of intermediate states. The cross-sections of various hadronic processes as well as the formation and fragmentation of the strings are described in details in [155]

4.6 Results: Elliptical flow

In this and the next sections, the results for the model application to 200A GeV RHIC data description are presented. As it was already said, important information about the space-time evolution of the system is provided by the study of the

azimuthal distribution of particle production. One usually expands

$$\frac{dn}{d\phi} \propto 1 + 2v_2 \cos 2\phi + \dots, \quad (4.54)$$

where a non-zero coefficient v_2 is referred to as elliptical flow [160]. It is usually claimed that the elliptical flow is proportional to the initial space eccentricity

$$\epsilon = \frac{\langle y^2 - x^2 \rangle}{\langle y^2 + x^2 \rangle}. \quad (4.55)$$

We therefore plot in fig. 4.9 the ratio of v_2 over eccentricity. The points are data;

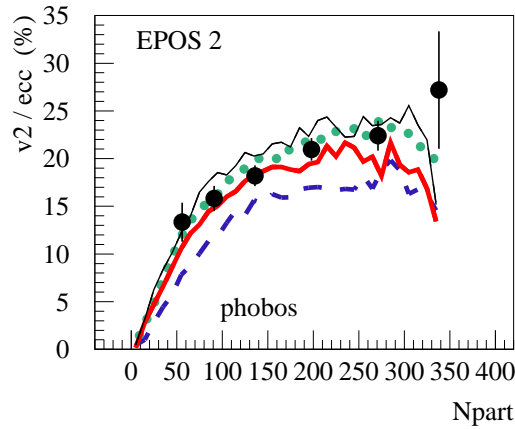


Figure 4.9: Centrality dependence of the ratio of v_2 over eccentricity. Points are data [161], the different curves refer to the full calculation – hydro & cascade (full line), only elastic hadronic scatterings (dotted), and no hadronic cascade at all (dashed). The thin solid line –above all others– refers to the hydrodynamic calculation till final freeze-out at 130 MeV.

the full line is the full calculation: hydrodynamical evolution with subsequent hadronic cascade, from flux tube initial conditions, in event-by-event treatment. The dotted line refers to a simplified hadronic cascade, allowing only elastic scatterings, the dashed line is the calculation without hadronic cascade. In all cases, hadronization from the thermal phase occurs at $T_H = 166$ MeV. We also show as thin solid line the hydrodynamic calculation till final freeze-out at 130 MeV. We use an energy density weighted average for the computation of the eccentricity. For both v_2 and ϵ , we take into account the fact that the principle axes of the initial matter distribution are tilted with respect to the reaction plane. So we get non-zero values even for very central collisions, due to the random fluctuations.

For all theoretical curves, the ratio v_2/ϵ is not constant, but increases substantially from peripheral towards central collisions – in agreement with the data. In

our case, this increase is a core-corona effect [162]. Adding final state hadronic rescattering leads to the full curve (full cascade) or the dotted one (only elastic scattering), adding some more 20 % to v_2 . The difference between the two rescattering scenarios is small, which means the effect is essentially due to elastic scatterings. Continuing the hydrodynamic expansion through the hadronic phase till freeze out at a low temperature (130MeV), instead of employing a hadronic cascade, we obtain a even higher elliptic flow, as shown by the thin line in fig. 4.9, and as discussed already in [115, 116, 163].

We now discuss the effect of the equation of state (see also [164]). Using a (non-realistic) first-order equations of state (curve Q1F from fig. 4.7), one obtains considerably less elliptical flow compared to the calculation using the the cross-over equation of state X3F, as seen in fig. 4.10. Taking a wrong equation-of-state

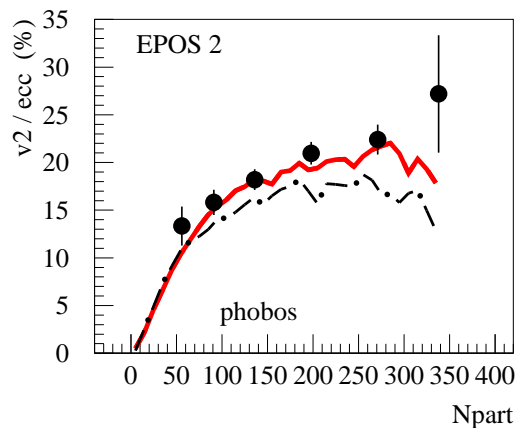


Figure 4.10: Centrality dependence of the ratio of v_2 over eccentricity, for a full calculation, hydro & hadronic cascae, for a (non-realistic) first-order transition equations of state (dashed-dotted line) compared to the cross-over equations of state, the default case (full line, same as the one in fig. 4.9). Points are data [161].

and a wrong treatment of the hadronic phase (thermally equilibrated rather than hadronic cascade) compensate each other, concerning the elliptical flow results.

In fig. 4.11, the (pseudo)rapidity dependence of the elliptical flow, for different centralities, is shown for Au-Au collisions at 200 GeV. Again, several scenarios are compared: the full treatment, namely hydrodynamic evolution from flux tube initial conditions with early hadronization (at 166 MeV) and subsequent hadronic cascade, and the calculations with only elastic rescattering, or no hadron scattering at all. Also shown as thin line is the case where the hydrodynamic expansion is continued through the hadronic phase till freeze out at a low temperature (130MeV), instead of employing a hadronic cascade.

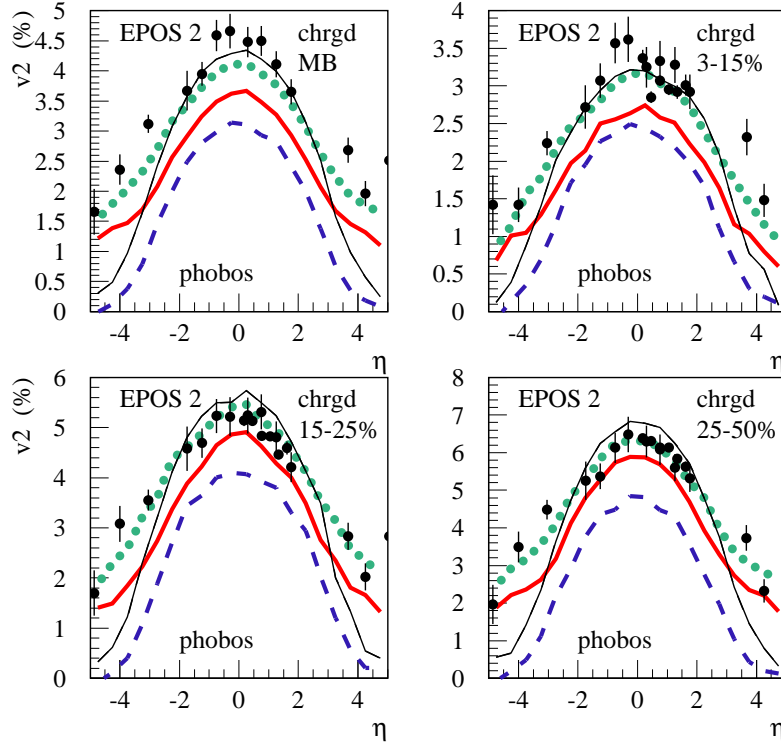


Figure 4.11: Pseudorapidity distributions of the elliptical flow v_2 for minimum bias events (upper left) and different centrality classes, in Au-Au collisions at 200 GeV. Points are data [166], the different curves refer to the full calculation – hydro & cascade (full thick line), only elastic hadronic scatterings (dotted), no hadronic cascade at all (dashed), and hydrodynamic calculation till final freeze-out at 130 MeV (thin line).

4.7 Transverse momentum spectra and yields

The next results show that the model created actually reproduces more elementary observables like simple transverse momentum (p_t) spectra and the integrated particle yields, for identified hadrons. We will restrict the following p_t spectra to values less than 1.5 GeV (2 GeV in some cases), mainly in order to limit the ordinate to three or at most four orders of magnitude, which allows still to see 10% differences between calculations and data.

In the upper panel of fig. 4.12, we show the p_t spectra of π^+ (left) and π^- (right) in central Au-Au collisions, for rapidities (from top to bottom) of 0, 2, and 3. The middle panels show the transverse momentum / transverse mass spectra of π^+ and π^- , for different centralities, and the lower panel the centrality dependence of the integrated particle yields per participant for charged particles and π^- mesons. In

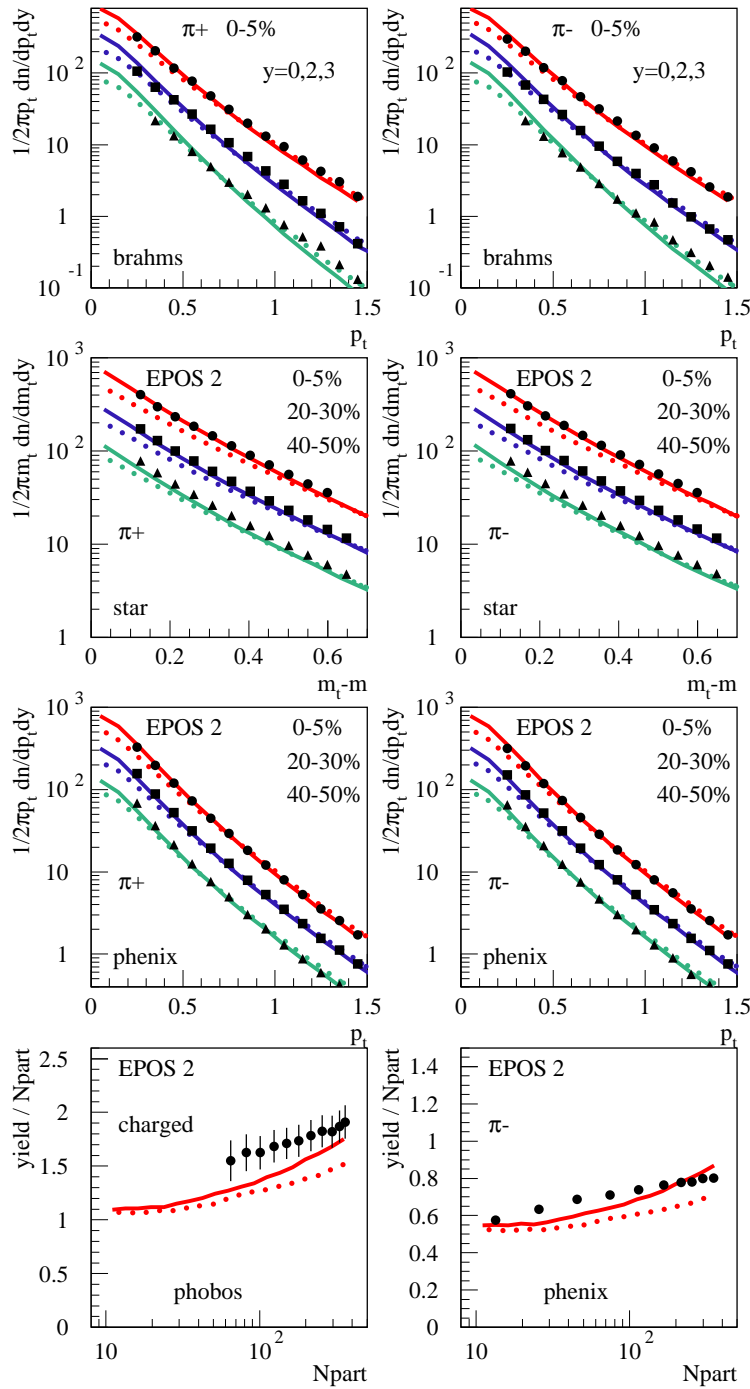


Figure 4.12: Production of pions in Au-Au collisions at 200 GeV. Upper panel: transverse momentum spectra for central collisions at different rapidities (from top to bottom: 0, 2, 3). The lower curves are scaled by factors of 1/2 and 1/4, for better visibility. Middle panels: transverse momentum (mass) distributions at rapidity zero for different centrality classes: from top to bottom: the 0-5%, the 20-30%, and the 40-50% most central collisions. Lower panel: the centrality dependence of the integrated yields for charged particles and pions. The symbols refer to data [173, 95, 72, 174], the full lines to our full calculations, the dotted lines to the calculations without hadronic cascade.

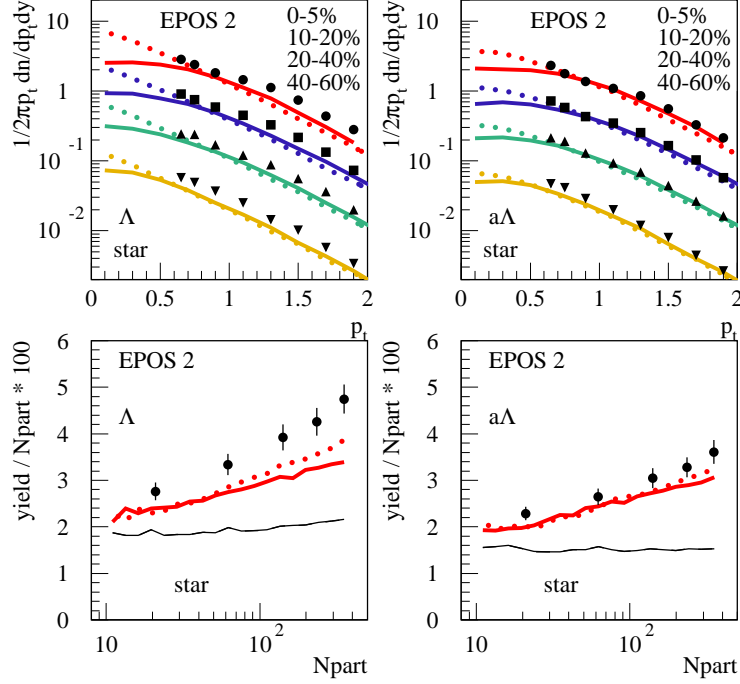


Figure 4.13: Production of lambdas (left) and antilambdas (right) in Au-Au collisions at 200 GeV. Upper panel: transverse momentum distributions at rapidity zero for different centrality classes: from top to bottom: the 0-5%, the 20-30%, and the 40-50% most central collisions. The lower curves are scaled by factors of 1/2, 1/4, and 1/8, for better visibility. Lower panel: the centrality dependence of the integrated yields. The symbols refer to data [140], the full lines to our full calculations, the dotted lines to the calculations without hadronic cascade. The thin line refers to a hydrodynamic calculation till final freeze-out at 130 MeV.

the upper panels, for the $y = 2$ and $y = 3$ curves, we apply scaling factors of 1/2 and 1/4, for better visibility, all other curves are unscaled. We present always two calculations: the full one (full lines), namely hydrodynamic evolution plus final state hadronic cascade, and the calculation without cascade (dotted lines). There is a slight increase of pion production in particular at low p_t during the hadronic rescattering phase, but the difference between the two scenarios is not very big. We see almost no difference between between the calculation with and without hadronic rescattering in case of kaons. For both, pions and kaons, we observe a change of slope of the p_t distributions with rapidity. Concerning the centrality dependence, we observe an increase of the yields per participant.

In fig. 4.13 we show p_t spectra and centrality dependence of particle yields per participant, for the (multi)strange baryons Λ , $\bar{\Lambda}$, Ξ , and $\bar{\Xi}$. Same conventions

as for the previous plots. Here we see a big effect due to rescattering: for the lambdas, the yields are not affected too much, but the p_t spectra get much softer, when comparing the full calculation with the one without rescattering. Similarly the slopes for the Ξ , and $\bar{\Xi}$ get softer due to rescattering.

To summarize the above discussion on yields and p_t spectra: an early hadronization at 166 MeV gives a reasonable description of the particle yields, which are not much affected by the hadronic final state rescattering, except for the protons. The main effect of the hadronic cascade is a softening of the p_t spectra of the baryons.

4.8 Femtoscopy

All the observables discussed so-far are strongly affected by the space-time evolution of the system, nevertheless we investigate the momentum space, and conclusions about space-time are indirect, as for example our conclusions about early hadronization based on particle yields and elliptical flow results. A direct insight into the space-time structure at hadronization is obtained from using femtoscopical methods [175, 176, 75, 177, 178].

In this section, $\pi^+ - \pi^+$ correlations are investigated. Here, we only consider quantum statistics for Ψ , no final state interactions, to compare with Coulomb corrected data. To compute the discretized correlation function $C_{ij} = C(\mathbf{P}_i, \mathbf{q}_j)$, we do our event-by-event simulations, and compute for each event $C'_{ij} = \sum_{pairs} |\Psi(\mathbf{q}', \mathbf{r}')|^2$, where the sum extends over all π^+ pairs with \mathbf{P} and \mathbf{q} within elementary momentum-space-volumes at respectively \mathbf{P}_i and \mathbf{q}_j . Then we compute the number of pairs N_{ij} for the corresponding pairs from mixed events, being used to obtain the properly normalized correlation function $C_{ij} = C'_{ij}/N_{ij}$. The correlation function will be parametrized as

$$C(\mathbf{P}, \mathbf{q}) = \frac{1}{1 + \lambda \exp(-R_{\text{out}}^2 q_{\text{out}}^2 - R_{\text{side}}^2 q_{\text{side}}^2 - R_{\text{long}}^2 q_{\text{long}}^2)}, \quad (4.56)$$

where "long" refers to the beam direction, "out" is parallel to projection of \mathbf{P} perpendicular to the beam, and "side" is the direction orthogonal to "long" and "out" [180, 181, 182]. In fig. 4.14, we show the results for the fit parameters λ , R_{out} , R_{side} , and R_{long} , for five different centrality classes and for four k_T intervals defined as (in MeV): KT1= [150, 250], KT2= [250, 350], KT3= [350, 450], KT4= [450, 600], where k_T of the pair is defined as

$$k_T = \frac{1}{2} (|\vec{p}_T(\text{pion } 1) + \vec{p}_T(\text{pion } 2)|). \quad (4.57)$$

Despite what appears in [77], this is the correct definition of k_T used by STAR in

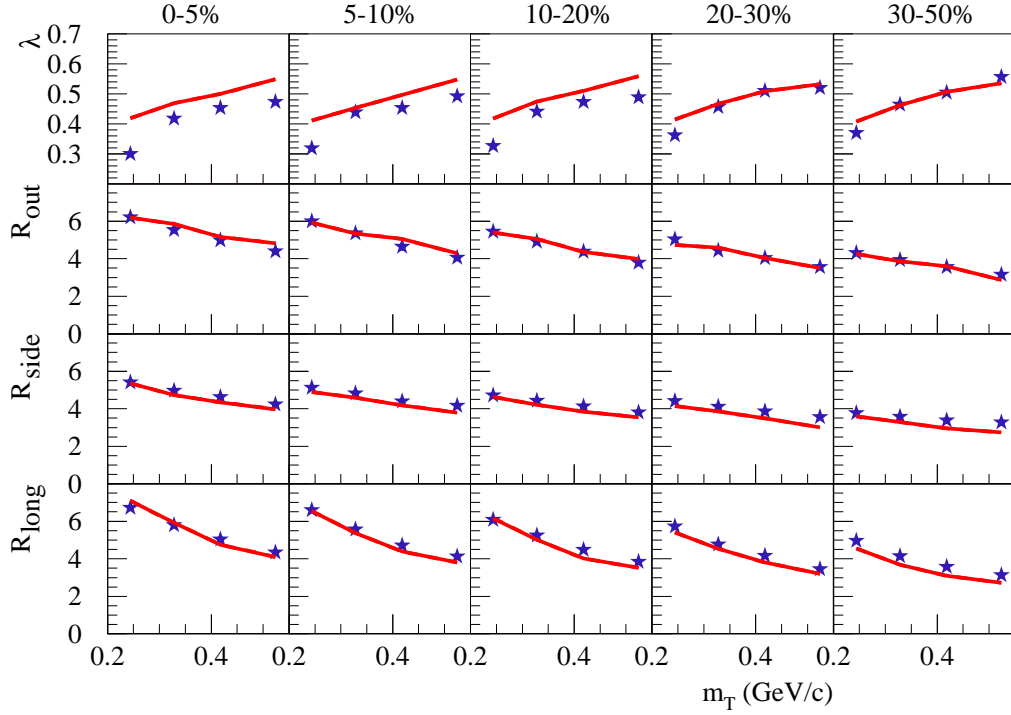


Figure 4.14: Femtosopic radii R_{out} , R_{side} , and R_{long} , as well as λ as a function of m_T for different centralities (0-5% most central, 5-10% most central, and so on). The full lines are the full calculations (including hadronic cascade), the stars data [77]

their analysis in[183]. The results are plotted as a function of $m_T = \sqrt{k_T^2 + m_\pi^2}$. The model describes well the radii, the experimental lambda values are slightly below the calculations, maybe due to particle misidentification. Both data and theory provide lambda values well below unity, maybe due to pions from long-lived resonances, which is compatible with the results of previous section. Concerning the m_T dependence of the radii, we observe the same trend as seen in the data [77]: all radii decrease with increasing m_T , and the radii decrease as well with decreasing centrality.

The reason for the decrease of radii with m_T is the strong space-momentum correlation. In fig. 4.15, we show the average p_x of produced π^+ mesons as a function of the x coordinate of their formation positions, for different centralities. Clearly visible is the strong $x - p_x$ correlation, being typical for radial flow. Also visible in the figure is the smaller spatial extension for peripheral compared to central collisions.

We now consider two other scenarios: the calculation without hadronic cascade

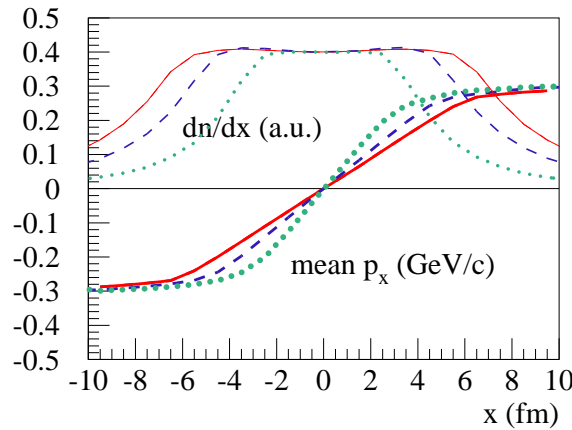


Figure 4.15: The mean transverse momentum component p_x of π^+ as a function of the x coordinate of the emission point. Also shown is the number of produced π^+ as a function of x . The different curves refer to different centralities: 0-5% = full line, 10-20% = dashed, 30-50% = dotted.

(final freeze out at 166 MeV), and the fully thermal scenario, where we continue the hydrodynamical evolution till a late freeze-out at 130 MeV (and no cascade afterwards either). In figs. 4.16 and 4.17, we see a similar space-momentum correlation as for the complete calculation in fig. 4.15: the mean transverse momentum

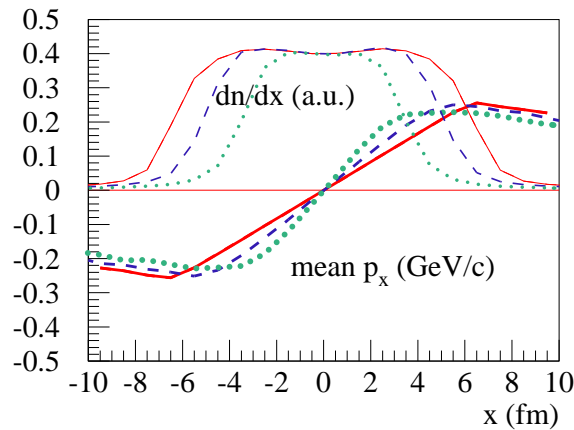


Figure 4.16: Same as fig. 4.15, but for the calculation without hadronic cascade.

components p_x is roughly a linear function of the transverse coordinate x , in the region where the particle density is non-zero. The maximum mean p_x is smaller in the no-cascade case, and bigger in the fully thermal case, as compared to the complete calculation. Interesting are the dn/dx distributions: the no-cascade results

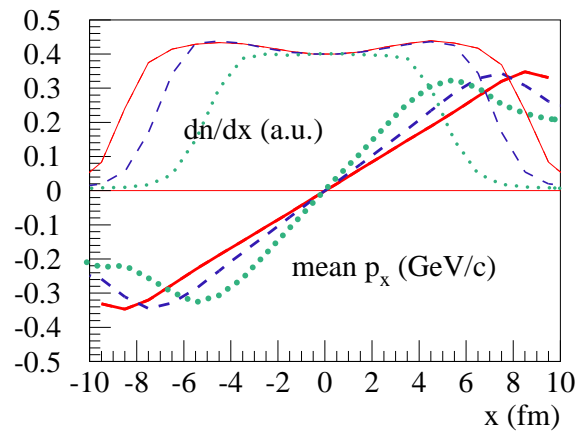


Figure 4.17: Same as fig. 4.15, but for the full thermal scenario (freeze-out at 130 MeV).

(with early hadronization) are much narrower than the full thermal ones. The complete calculation of fig. 4.15 is in-between, in the sense that the plateau of the dn/dx distribution is similar to the no-cascade case, but the tails are much wider.

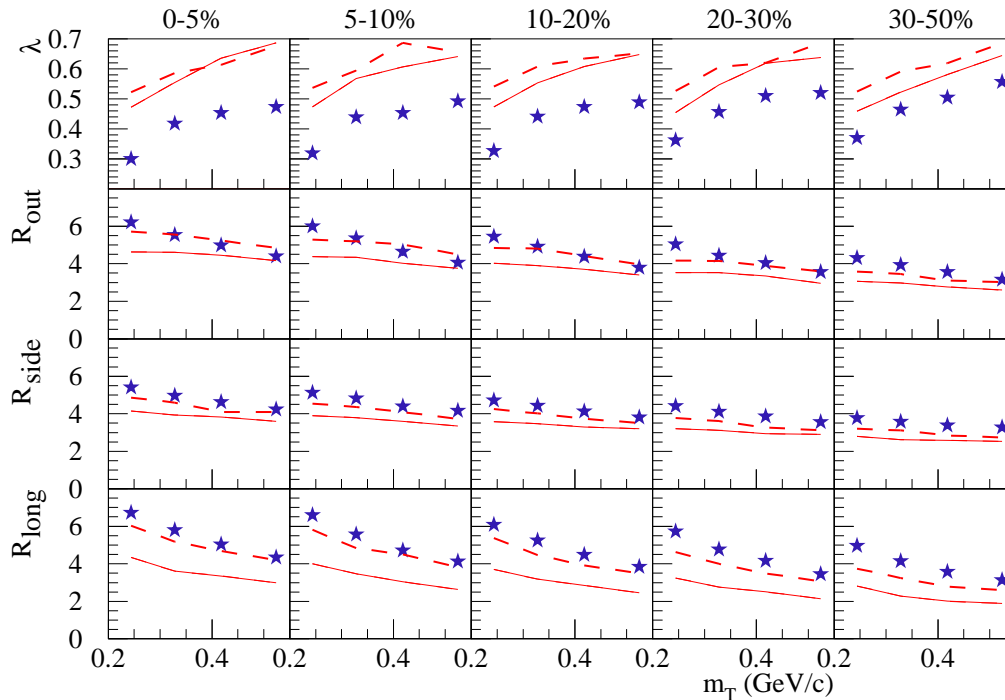


Figure 4.18: Same as fig. 4.14, but the calculations are done without hadronic cascade (full line) or with a hydrodynamic evolution through the hadronic phase with freeze-out at 130 MeV (dashed).

Although the Gaussian parameterizations represent only an incomplete information about the source functions, the centrality and transverse momentum dependence of the radii is nevertheless very useful. As it is stated above, it is a necessary requirement for all models of soft physics to describe these radii correctly. There has been for many years an inconsistency, referred to as “HBT puzzle” [153]. Although hydrodynamics describes very successfully elliptical flow and to some extent particle spectra, one cannot get the femtoscopic radii correctly, when one uses “simple” hydrodynamics. Using transport models (and an event-by-event treatment) may help [177]. In [153], it has been shown that the puzzle can actually be solved by adding pre-equilibrium flow, taking a realistic equation of state, adding viscosity, using a more compact or more Gaussian initial energy density profile, and treating the two-pion wave function more accurately. It has also been shown [7, 190, 191] that using a Gaussian initial energy density profile, an early starting time (equivalent to initial flow), and a cross-over equation of state, and a late sudden freeze-out (at 145 MeV) helps to describe the femtoscopic radii, and to some extent the spectra.

The scenario in [7, 190, 191] is compatible with our scenario “hydrodynamical evolution till final freeze-out at 130MeV”, which allows us to get the femtoscopic radii correctly (see fig. 4.18), as well as some v_2 results and some spectra. One cannot describe, however, yields and spectra of lambdas and xis.

4.9 Summary and conclusions

In this chapter, the new hybrid dynamical model for matter evolution in ultrarelativistic heavy ion collisions is presented. It has many improvements, as compared to existing ones: flux-tube initial conditions (EPOS), event-by-event treatment, use of an efficient (3+1)D hydro code including flavor conservation, employment of a realistic equation-of-state, use of a complete hadron resonance table, and a hadronic cascade procedure after an hadronization from thermal matter at an early time.

The approach is able to describe simultaneously different soft observables: transverse spectra for pions, kaons, protons, lambdas, xis; v_2 -coefficients for pions, protons and kaons; interferometry (HBT)-radii for pions.

An agreement with experimental data supports the dynamical picture, realized in this model: a hydrodynamic evolution starting from EPOS initial conditions, till hadronization at an early time in the cross-over region of the phase transition, with subsequent hadronic rescatterings.

Hydro-kinetic model

In this chapter, the hydrokinetic approach, which incorporates hydrodynamic expansion of the systems formed in A+A collisions and their dynamical decoupling, is presented. The approach provides the alternative way of connection between the dense hydrodynamic stage and kinetic stage, and allows to account for the deviations from local equilibrium at hydrodynamic stage. It is demonstrated how the approximation of sudden freeze-out can be obtained within this dynamical picture of continuous emission. The approach is extended to include realistic features of A+A collisions and applied then to describe pion and kaon HBT data at RHIC collisions. Finally, a study of energy behavior of the pion spectra and interferometry scales is carried out for the top SPS, RHIC and LHC energies.

5.1 Introduction

It has been known for a long time that CFp leads to inconsistencies [46, 47], if the freeze-out hypersurface contains the non-space-like sectors, and should be modified to exclude formally negative contributions to the particle number at the corresponding momenta. The simplest prescription is to present the distribution function as a product of a local thermal distribution and the step function like $\theta(p_\mu n^\mu(x))$ [47], $n^\mu n_\mu = \pm 1$, where n^μ is a time-like or space-like outward normal to a freeze-out hypersurface σ . Thereby freeze-out is restricted to those particles for which $p_\mu n^\mu(x)$ is positive. This receipt was used in Ref. [48] to describe particle emission from enclosed freeze-out hypersurface with non-space-like sectors and it was found that a satisfactory description of central $Au+Au$ collisions at RHIC can be reached for a physically reasonable set of parameters. The main features of the experimental data were reproduced: in particular, the obtained ratio of the outward to sideward interferometry radii is less than unity and decreases with

increasing transverse momenta of pion pairs. Thereby, the results of Ref. [48] clearly indicate that early particle emission off the surface of the hydrodynamically expanding fireball could be essential for proper description of matter evolution in $A+A$ collisions.

However, sharp freeze-out at some 3D hypersurfaces is a rather rough approximation of the spectrum formation, because the particle emission process of fireballs created in high energy heavy ion collisions is gradual in time. Results of many studies based on cascade models contradict the idea of sudden freeze-out and demonstrate that in fact particles are emitted from the 4D volume during the whole period of the system evolution, and deviations from local equilibrium conditioned by continuous emission should take place (see, e.g., [93]). Moreover, freeze-out hypersurfaces typically contain non-space-like parts that lead to a problem with energy-momentum conservation law in realistic dynamical models [47]. This concerns also hybrid models [201] where the transport model matches hydrodynamics on such a kind of isothermal hypersurface of hadronization [198].¹

An attempt to introduce 4D continuous emission in hydrodynamic framework has been done in Ref. [200] within a simple ideal hydrodynamics, and also supported by numerical transport codes calculations. It was found in these papers that the transport freeze-out process is similar to evaporation: high- p_T particles freeze out early from the surface, while low- p_T ones decouple later from the system's center.

The idea of continuous decoupling was further developed based on Boltzmann equations in Ref. [199] where, in particular, an approximate method that accounts for the back reaction of the emission on the fluid dynamics was proposed. It is worth noting that the back reaction is not reduced just to an energy-momentum recoiling of emitted particles on the expanding thermal medium, but also leads to a rearrangement of the medium, producing a deviation of its state from the local equilibrium, accompanied by changing of the local temperature, densities and collective velocity field. This complex effect is mainly a consequence of the impossibility to split the evolution of the single finite system of hadrons into the two components: expansion of the interacting locally equilibrated medium and free streaming of emitted particles, which the system consists of. Such a splitting, accounting only for the momentum-energy conservation law, contradicts the underlying dynamical equations such as a Boltzmann one [199]. In view of this, the ideas proposed and results obtained in the quasiclassical approach should be a clue for a quantum treatment of the problem which recently started to be developed

¹Note that in this hybrid picture the initial conditions for hadronic cascade calculations could be formulated also on some (arbitrary) *space-like* hypersurface where, however, hadronic distributions deviate from the local equilibrium, in particular, because of an opacity effect for hadrons which are created during a “mixed” stage of phase transition. These nonequilibrium effects could seriously influence the results of hybrid models in its modern form [201].

[196]. Note, however, that the estimates of the influence of the quantum effects, such as the distortion of the wave function, on the spectra and Bose-Einstein correlations testify to be relatively small corrections to the quasiclassical approximation [197].

5.2 General formalism

It was proposed in Ref. [199] to describe the hadronic momentum spectra in $A+A$ collisions based on the escape function of particles which are gradually liberated from hydrodynamically expanding systems. The escape function, introduced in [200], is calculated within the Boltzmann equations in a specific approximation based on a hydrodynamic approach. It was shown that such a picture corresponds to a relativistic kinetic equation with the relaxation time approximation for the collision term, where the relaxation time tends to infinity, $\tau_{\text{rel}} \rightarrow \infty$, when $t \rightarrow \infty$, indicating a transition to the free streaming regime. For one component system the equation has the form:

$$\frac{p^\mu}{p_0} \frac{\partial f(x, p)}{\partial x^\mu} = - \frac{f(x, p) - f^{\text{leq}}(x, p)}{\tau_{\text{rel}}(x, p)}. \quad (5.1)$$

Here $f(x, p)$ is the phase-space distribution function, $f^{\text{leq}}(x, p)$ is the local equilibrium distribution with local velocities, temperatures, and chemical potentials that should be found from Eq. (5.1) and the initial $f_0(x, p)$, and $\tau_{\text{rel}}(x, p)$ is the relaxation time (inverse rate of collisions in gases),

$$\tau_{\text{rel}}(x, p) = \frac{p_0 \tau_{\text{rel}}^*(x, p)}{p^\mu u_\mu}. \quad (5.2)$$

Here $\tau_{\text{rel}}^*(x, p)$ is related to the local fluid rest frame (local rest frame of the energy flow) where the collective four-velocity is $u_\mu = (1, \mathbf{0})$. The relaxation time depends on the cross section and is a functional of $f^{\text{leq}}(x, p)$.

As it is well known, such kinds of equations at $\tau_{\text{rel}} \ll \tau_{\text{exp}}$ (inverse of expansion rate) describe in the first approximation the viscosity effects in gases with a coefficient of shear viscosity $\eta \propto \tau_{\text{rel}} n T$. Therefore the method explained below catches in the first approximation also the viscosity effects in an expanding hadronic gas, characterized by fields of temperatures T and particle densities n . The viscosity effects in the quark-gluon plasma (QGP) evolution cannot be described in this way because strongly interacting QGP is not a gas, but almost an ideal liquid [16].

The formal solution of Eq. (5.1) can be presented in the following form:

$$f(t, \mathbf{r}, p) = f(t_0, \mathbf{r} - \frac{\mathbf{P}}{p_0}(t - t_0), p) \exp \left\{ - \int_{t_0}^t \frac{1}{\tau_{\text{rel}}(s, \mathbf{r} - \frac{\mathbf{P}}{p_0}(t - s), p)} ds \right\} + \int_{t_0}^t \frac{f^{\text{leq}}(t', \mathbf{r} - \frac{\mathbf{P}}{p_0}(t - t'), p)}{\tau_{\text{rel}}(t', \mathbf{r} - \frac{\mathbf{P}}{p_0}(t - t'), p)} \exp \left\{ - \int_{t'}^t \frac{1}{\tau_{\text{rel}}(s, \mathbf{r} - \frac{\mathbf{P}}{p_0}(t - s), p)} ds \right\} dt', \quad (5.3)$$

where $f(t_0, \mathbf{r}, p)$ is the initial distribution at $t = t_0$. The relaxation time τ_{rel}^* as well as the local equilibrium distribution function f^{leq} are functionals of hydrodynamic variables: temperature T , chemical potential μ , and collective four-velocity u_μ . The space-time dependence of the corresponding variables is determined by demanding the local conservation of the energy-momentum, with tensor $T^{\mu\nu}(x)$ and, if necessary, net particle number, with current $n^\mu(x)$ (assuming no particle production)

$$\partial_\mu T^{\mu\nu}(x) = 0, \quad (5.4)$$

$$\partial_\mu n^\mu(x) = 0, \quad (5.5)$$

where (see, e.g., Ref. [39])

$$T^{\mu\nu}(x) = \int \frac{d^3k}{k_0} k^{\mu\nu} f(x, k), \quad (5.6)$$

$$n^\mu(x) = \int \frac{d^3k}{k_0} k^\mu f(x, k). \quad (5.7)$$

These conservation laws lead to rather complicated equations for hydrodynamic variables. It is worth noting that for an expanding system the relaxation time $\tau_{\text{rel}}^*(x, p)$ increases with time and, therefore, the deviations from local equilibrium increase too, thereby preventing a use of the widely applied approximate methods based on the expansion of the distribution function in the vicinity of the local equilibrium.

Then to solve the kinetic equation (5.1), in accordance with the conservation laws (5.4) and (5.5), we need an approximate method that could be applied even for strong deviations from local equilibrium. It is not our aim here to suggest an exclusive solution of the problem. Rather some arguments are presented below by the example of the relativistic one component Boltzmann gas with particle number conservation,

$$f^{\text{leq}}(x, p) = (2\pi)^{-3} \exp \left(- \frac{p^\mu u_\mu + \mu}{T} \right), \quad (5.8)$$

to show that such a method could be developed based on the following procedure.

To take into account nonequilibrium effects accompanying the particle emission in inhomogeneous violently expanding systems, we utilize the integral representation (5.3) of kinetic equation (5.1). Then, performing a partial integration of the second term in Eq. (5.3) and, assuming that $f(t_0, \mathbf{r}, p) = f^{\text{leq}}(t_0, \mathbf{r}, p)$, one can decompose the distribution function to a local equilibrium part, f^{leq} , and a part describing a deviation from the local equilibrium behavior, g :

$$f = f^{\text{leq}}(x, p) + g(x, p), \quad (5.9)$$

where

$$g(x, p) = - \int_{t_0}^t \frac{df^{\text{leq}}(t', \mathbf{r} - \frac{\mathbf{p}}{p_0}(t-t'), p)}{dt'} \times \\ \times \exp \left\{ - \int_{t'}^t \frac{1}{\tau_{\text{rel}}(s, \mathbf{r} - \frac{\mathbf{p}}{p_0}(t-s), p)} ds \right\} dt'. \quad (5.10)$$

Note that both functions, f^{leq} and g , are functionals of hydrodynamic variables, g depends also on the relaxation time τ_{rel} that defines the mean time interval between collisions, and τ_{rel} depends in its turn on the distribution function f^{leq} and the cross section. The evolution of the distribution function $f(x, p)$ should satisfy the energy-momentum conservation and, because $T^{\mu\nu}[f] = T^{\mu\nu}[f^{\text{leq}} + g] = T^{\mu\nu}[f^{\text{leq}}] + T^{\mu\nu}[g]$ for systems where the interaction energy can be neglected, it takes the form of hydrodynamic equations for the perfect fluid with ‘‘source’’,

$$\partial_\nu T^{\nu\beta}[f^{\text{leq}}] = G^\beta[g], \quad (5.11)$$

where

$$G^\beta[g] = -\partial_\nu T^{\nu\beta}[g]. \quad (5.12)$$

The equation that takes into account the conservation of particle number has a similar form:

$$\partial_\nu n^\nu[f^{\text{leq}}] = S[g], \quad (5.13)$$

where

$$S[g] = -\partial_\nu n^\nu[g]. \quad (5.14)$$

To find an approximate solution of Eqs. (5.11)-(5.14), one can solve the equations

$$\partial_\nu T^{\nu\mu}[f^{\text{leq}}] = 0, \quad (5.15)$$

$$\partial_\nu n^\nu[f^{\text{leq}}] = 0, \quad (5.16)$$

and, thereby, utilize the hydrodynamic variables in the perfect fluid approximation. Namely, the hydrodynamic variables in this approximation can be used to calculate the deviation from local equilibrium $g(x, p)$ according to Eq. (5.10) and, then, “source” terms $G^\beta[g]$ and $S[g]$ on the right-hand sides of Eqs. (5.11) and (5.13). Then the left-hand sides of these equations are functionals of local equilibrium functions and have the simple ideal fluid forms, while the right-hand sides associated with a “source” are explicit functions which describe a deviation from the local equilibrium and depend on hydrodynamic variables in the perfect fluid approximation:

$$\partial_\nu T^{\nu\beta}[f^{\text{leq}}(T, u_\mu, \mu)] = G^\beta[T_{\text{id}}, u_\mu^{\text{id}}, \mu_{\text{id}}, \tau_{\text{rel}}^{\text{id}}], \quad (5.17)$$

$$\partial_\nu n^\nu[f^{\text{leq}}(T, u_\mu, \mu)] = S[T_{\text{id}}, u_\mu^{\text{id}}, \mu_{\text{id}}, \tau_{\text{rel}}^{\text{id}}], \quad (5.18)$$

where, for one component Boltzmann gas with elastic collisions only, the relaxation time $\tau_{\text{rel}}^{\text{id}}$ is the inverse of collision rate in ideal fluid, $R^{\text{id}}(x, p)$, and has the following form (in the co-moving frame):

$$\begin{aligned} \frac{1}{\tau_{\text{rel}}^{\text{id}*}(x, p)} &= R^{\text{id}}(x, p) = \\ &= \int \frac{d^3k}{(2\pi)^3} \exp\left(-\frac{E_k - \mu_{\text{id}}(x)}{T_{\text{id}}(x)}\right) \sigma(s) \frac{\sqrt{s(s - 4m^2)}}{2E_p E_k}. \end{aligned} \quad (5.19)$$

Here $E_p = \sqrt{\mathbf{p}^2 + m^2}$, $E_k = \sqrt{\mathbf{k}^2 + m^2}$, $s = (p + k)^2$ is the squared c.m. energy of the pair, and $\sigma(s)$ is the corresponding cross section. A solution $(T(x), u_\mu(x), \mu(x))$ of Eqs. (5.17), (5.18) accounts for the back reaction of the emission process on hydro-evolution and provides us with the hydrodynamic parameters which finally should be used to calculate the locally equilibrated part $f^{\text{leq}}(x, p)$ of the complete distribution function $f(x, p)$. Then, the distribution function obtained in this way, $f(x, p) = f^{\text{leq}}[T, u_\mu, \mu] + g[T_{\text{id}}, u_\mu^{\text{id}}, \mu_{\text{id}}, \tau_{\text{rel}}^{\text{id}}]$, satisfies the conservation laws, takes into account the nonequilibrium peculiarities of the evolution and is constructed in agreement with the corresponding EoS. Of course, this scheme allows us to make the next iterations in solving Eq. (5.1). Note also that because the “source” term on the right-hand side of Eq. (5.17) is a known function, the causality is preserved in this description of dissipative systems.

5.3 Cooper-Frye prescription

In this section, we will try to derive the Cooper-Frye approximation within the approach. Let us start from Boltzmann equation in general form:

$$\frac{p^\mu}{p^0} \frac{\partial f_i(x, p)}{\partial x^\mu} = G_i(x, p) - L_i(x, p). \quad (5.20)$$

The expressions $G_i(x, p)$ and $L_i(x, p) = R_i(x, p)f_i(x, p)$ are so-called (G)ain and (L)oss terms for the particle of species i . Typically, R_i is a rate of collisions of i -th particle. Below we will omit index i , the corresponding expression can be related then, e.g., to pions.

The probability $\mathcal{P}_{t \rightarrow t'}(x, p)$ for a particle to reach the point $x' = (t', \mathbf{r}')$ starting from the point $x = (t, \mathbf{r})$ without collisions is

$$\mathcal{P}_{t \rightarrow t'}(x, p) = \exp \left(- \int_t^{t'} d\bar{t} R(\bar{x}_t, p) \right), \quad (5.21)$$

where

$$\bar{x}_t = (\bar{t}, \mathbf{r} + \frac{\mathbf{P}}{p^0}(\bar{t} - t)).$$

In terms of this probability, the Boltzmann equation can be rewritten in the following integral form

$$\begin{aligned} f(t, \mathbf{r}, p) &= f(t_0, \mathbf{r} - \frac{\mathbf{P}}{p^0}(t - t_0), p) \mathcal{P}_{t_0 \rightarrow t}(t_0, \mathbf{r} - \frac{\mathbf{P}}{p^0}(t - t_0), p) \\ &+ \int_{t_0}^t G(\tau, \mathbf{r} - \frac{\mathbf{P}}{p^0}(t - \tau), p) \mathcal{P}_{\tau \rightarrow t}(\tau, \mathbf{r} - \frac{\mathbf{P}}{p^0}(t - \tau), p) d\tau. \end{aligned} \quad (5.22)$$

Let us integrate the distribution (5.22) over the space variables to represent the particle momentum density at large enough time, $t \rightarrow \infty$, when particles in the system stop to interact. To simplify notation let us introduce the escape probability for the particle with momentum p in the point $x = (t, \mathbf{r})$ to leave system without collisions: $\mathcal{P}(t, \mathbf{r}, p) \equiv \mathcal{P}_{t \rightarrow (\tau \rightarrow \infty)}(t, \mathbf{r}, p)$. Then the result can be presented in the general form found in Ref. [199]:

$$\begin{aligned} n(t \rightarrow \infty, p) &\equiv n(p) = \int d^3r f(t_0, \mathbf{r}, p) \mathcal{P}(t_0, \mathbf{r}, p) \\ &+ \int d^3r \int_{t_0}^{\infty} dt' G(t', \mathbf{r}, p) \mathcal{P}(t', \mathbf{r}, p). \end{aligned} \quad (5.23)$$

The first term in Eq. (5.23) describes the contribution to the momentum spectrum from particles that are emitted from the very initial time, while the second one describes the continuous emission with emission density $S(x, p) = G(t, \mathbf{r}, p) \mathcal{P}(t, \mathbf{r}, p)$ from 4D volume delimited by the initial and final (where particles stop to interact) 3D hypersurfaces.

In what follows we will use the (generalized) relaxation time approximation proposed in [199], which is the basis of the hydro-kinetic approach, described in detail in [202]. Namely, it was argued [199] that there is such a local equilibrium distribution function $f_{l.eq.}(T(x), u'(x), \mu(x))$ that, in the region of not very small densities where term $G \sim S$ gives noticeable contribution to particle spectra, the function f is approximately equal to that one which would be obtained if all functions in r.h.s. of Eq. (5.22) calculated by means of that function $f_{l.eq.}$. The function $f_{l.eq.}$ is determined from the local energy-momentum conservation laws based on the non-equilibrium function f in the way specified in [202]. Then, in accordance with this approach we use

$$R(x, p) \approx R_{l.eq.}(x, p), G \approx R_{l.eq.}(x, p) f_{l.eq.}(x, p). \quad (5.24)$$

The “relaxation time” $\tau_{rel} = 1/R_{l.eq.}$ grows with time in this method.

Let us generalize now the Landau/Cooper-Frye prescription (CFp) of sudden freeze-out. For this aim we apply the saddle point method to calculate the integral in the expression for spectra (5.23) with account of (5.24). To simplify notation we neglect the contribution to the spectra from hadrons which are already free at the initial thermalization time $t_0 \sim 1$ fm/c and thus omit the first term in (5.22).

To provide straightforward calculations leading to the Cooper-Frye form let us shift the spacial variables, $\mathbf{r}' = \mathbf{r} + \frac{\mathbf{p}}{p_0}(t_0 - t')$, in (5.23) aiming to eliminate the variable t' in the argument of the function R which is the integrand in $\mathcal{P}(t', \mathbf{r}, p)$. Then

$$n(p) \approx \int d^3 r' \int_{t_0}^{\infty} dt' f_{l.eq.}(t', \mathbf{r}' + \frac{\mathbf{p}}{p_0}(t' - t_0), p) Q(t', \mathbf{r}', \mathbf{p}), \quad (5.25)$$

where

$$Q(t', \mathbf{r}', p) = R(t', \mathbf{r}' + \frac{\mathbf{p}}{p_0}(t' - t_0), p) \times \\ \times \exp \left\{ - \int_{t'}^{\infty} R(s, \mathbf{r}' + \frac{\mathbf{p}}{p_0}(s - t_0), p) ds \right\} \quad (5.26)$$

Note that

$$Q(t', \mathbf{r}', p) = \frac{d}{dt'} P(t', \mathbf{r}', \mathbf{p}), \quad (5.27)$$

where $P(t', \mathbf{r}', p)$ is connected with the escape probability \mathcal{P} :

$$P(t', \mathbf{r}', p) = \mathcal{P}(t', \mathbf{r}' + \frac{\mathbf{p}}{p_0}(t' - t_0), p). \quad (5.28)$$

Therefore

$$\int_{t_0}^{\infty} dt' Q(t', \mathbf{r}', p) = 1 - \mathcal{P}(t_0, \mathbf{r}', p) \approx 1. \quad (5.29)$$

The saddle point $t_\sigma(\mathbf{r}, p)$ is defined by the standard conditions:

$$\begin{aligned} \frac{dQ(t', \mathbf{r}', p)}{dt'} \Big|_{t'=t_\sigma} &= 0, \\ \frac{d^2Q(t', \mathbf{r}', p)}{dt'^2} \Big|_{t'=t_\sigma} &< 0. \end{aligned} \quad (5.30)$$

Then one can get from (5.27), (5.28) the condition of the maximum of emission:

$$-\frac{p^\mu \partial_\mu R(t', \mathbf{r}, p)}{R(t'_\sigma, \mathbf{r}, p)} \Big|_{t'=t'_\sigma, \mathbf{r}=\mathbf{r}' + \frac{\mathbf{p}}{p_0}(t'_\sigma - t_0)} = p_0 R(t'_\sigma, \mathbf{r}' + \frac{\mathbf{p}}{p_0}(t'_\sigma - t_0), p). \quad (5.31)$$

If one neglects terms $\mathbf{p}^* \partial_{\mathbf{r}^*} R$ in l.h.s. and supposes that in the rest frame (marked by asterisk) of the fluid element with four-velocity $u(x)$ the collision rate, $R^*(x, p) = \frac{p_0 R(x, p)}{p^\mu u_\mu}$, does not depend on particle momentum: $R^*(x) \approx \langle v^* \sigma \rangle(x) n^*(x)$ (here $n(x)$ is particle density, σ is the particle cross-section, v is the relative velocity, $\langle \dots \rangle$ means the average over all momenta), then the conditions (5.31) are equivalent to the requirement that at the temporal point of maximum of the emission function the rate of collisions is equal to the rate of system expansion [202]. This is the heuristic freeze-out criterion for sudden freeze-out [204]. However, as we will demonstrate, the neglect of momentum dependence leads to quite significant errors.

To pass to the Cooper-Frye representation we use the variables which include the saddle point:

$$\mathbf{r} = \mathbf{r}' + \frac{\mathbf{p}}{p_0}(t'_\sigma(\mathbf{r}', p) - t_0). \quad (5.32)$$

Then the expression for the spectrum takes the form:

$$n(p) \approx \int d^3r \left| 1 - \frac{\mathbf{p}}{p_0} \frac{\partial t_\sigma}{\partial \mathbf{r}} \right| \int_{t_0}^{\infty} dt' S(t', \mathbf{r}, p), \quad (5.33)$$

where the emission density in saddle point representation is ($t_\sigma \equiv (t_\sigma(\mathbf{r}, p))$)

$$\begin{aligned} S(t', \mathbf{r}, p) &= f_{1.\text{eq.}}(t', \mathbf{r} + \frac{\mathbf{p}}{p_0}(t' - t_\sigma), p) \\ &\times R(t_\sigma, \mathbf{r}, p) \mathcal{P}(t_\sigma, \mathbf{r}, p) \exp(-(t' - t_\sigma)^2 / 2D^2(t_\sigma, \mathbf{r}, p)). \end{aligned} \quad (5.34)$$

According to Eq. (5.21) $\mathcal{P}(t_\sigma, \mathbf{r}, p) = e^{-1}$, since the freeze-out zone is the region of the last collision for the particle. Then the normalization condition for Q (Q is presented by the bottom line in (5.34)) allows one to determine the temporal width of the emission at the point $(t_\sigma(\mathbf{r}, p), \mathbf{r}, p)$:

$$D(t_\sigma, \mathbf{r}, p) = \frac{e}{\sqrt{2\pi}} \frac{1}{R(t_\sigma, \mathbf{r}, p)} \approx \tau_{\text{rel}}(t_\sigma, \mathbf{r}, p). \quad (5.35)$$

Therefore if the temporal homogeneity length $\lambda(t, \mathbf{r}, p)$ of the distribution function $f_{1.\text{eq.}}$ near the 4-point $(t_\sigma(\mathbf{r}, p), \mathbf{r})$ is much larger than the width of the emission zone, $\lambda(t_\sigma, \mathbf{r}, p) \gg \tau_{\text{rel}}(t_\sigma, \mathbf{r}, p)$, then one can approximate $f_{1.\text{eq.}}(t', \mathbf{r} + \frac{\mathbf{p}}{p_0}(t' - t_\sigma), p)$ by $f_{1.\text{eq.}}(t_\sigma, \mathbf{r}, p)$ in Eq. (5.33) and perform integration over t' accounting for normalization condition (5.29). As a result we get from (5.33) and (5.34) the momentum spectrum in a form similar to the Cooper-Frye one (3.19):

$$p^0 n(p) = p^0 \frac{d^3 N}{d^3 p} \approx \int_{\sigma(p)} d\sigma_\mu p^\mu f_{1.\text{eq.}}(x, p). \quad (5.36)$$

It is worthy to note that the representation of the spectrum through emission function (5.23) is the result of the integration of the total non-equilibrium distribution function $f(x, p)$, Eqs. (5.22), (5.24), over the asymptotical hypersurface in time, while the approximate representation of the spectrum, Eq. (5.36), uses only the local equilibrium part $f_{1.\text{eq.}}$ of the total function $f(x, p)$ at the set of points of maximal emission - at hypersurface $(t_\sigma(\mathbf{r}, p), \mathbf{r})$.

Generalized Cooper-Frye prescription

Now let us summarize the conditions when the Landau/Cooper-Frye form for sudden freeze-out can be used. They are the following:

i) For each momentum \mathbf{p} , there is a region of \mathbf{r} where the emission function as well as the function Q , Eq. (5.26), have a clear maximum. The temporal width of the emission D , defined by Eq. (5.34), which is found to be equal to the relaxation time (inverse of collision rate), should be smaller than the corresponding temporal homogeneity length of the distribution function: $\lambda(t_\sigma, \mathbf{r}, p) \gg D(t_\sigma, \mathbf{r}, p) \simeq \tau_{\text{rel}}(t_\sigma, \mathbf{r}, p)$.

ii) The contribution to the spectrum from the residual region of \mathbf{r} , where the saddle point method (Gaussian approximation (5.34) and/or condition $\tau_{\text{rel}} \ll \lambda$) is violated, does not affect essentially the particle momentum density.

If these conditions are satisfied, then the momentum spectra can be presented in the Cooper-Frye form *despite the fact that actually it is not sudden freeze-out and the decoupling region has a finite temporal width $\tau_{\text{rel}}(t_\sigma, \mathbf{r}, p)$* .

The analytical results as for the temporal width of the spectra agree remarkably with the numerical calculations of pion emission function within hydro-kinetic

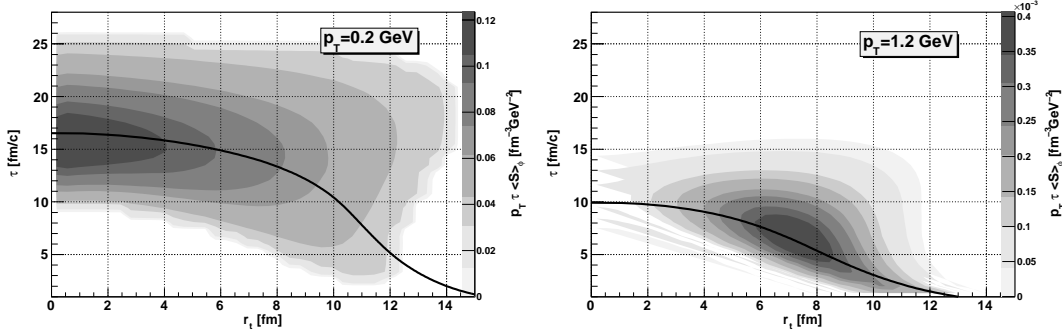


Figure 5.1: The pion emission function for different p_T in hydro-kinetic model (HKM) [202]. The isotherms of 80 MeV (left) and 135 MeV (right) are superimposed.

model (HKM) [202]. For example, near the point of maximum, $\tau = 16.5$ fm/c, $r = 0, p_T = 0.2$ GeV, the “experimental” temporal width D_{HKM} obtained by numerical solution of the complete hydro-kinetic equations is $D_{HKM} \approx 4.95$ fm (see Fig. 5.3, left). Our theoretical estimate is $D = \frac{e}{\sqrt{2\pi R}} \approx 5.00$ fm, since the rate of collisions in this phase-space point is $R(\tau_\sigma(\mathbf{r}, p) = 16.5 \text{ fm/c}, \mathbf{r} = 0, p_T = 0.2 \text{ GeV}, p_L = 0) \approx 0.217 \text{ c/fm}$.

It is worthy to emphasize that such a generalized Cooper-Frye representation is related to *freeze-out hypersurfaces that depend on the momentum \mathbf{p} and typically do not enclose the initially dense matter*. In Fig. 5.3, one can see the structure of the emission domains for different p_T in HKM [202] for initially (at $\tau=1$ fm/c) Gaussian energy density profile with $\epsilon_{max} = 6 \text{ GeV/fm}^3$. The maximal emission regions for different p_T are crossed by isotherms with different temperatures: 80 MeV for low momenta and 135 MeV for high ones. This is completely reflected in the concave structure of the transverse momentum spectrum as one can see in Fig. 5.3.

If a part of the hypersurface $t_\sigma(\mathbf{r}, p)$ is non-space-like and corresponds to the maximum of the emission of particles with momentum \mathbf{p} , directed outward the system, the same part of the hypersurface cannot correspond to the maximal emission for particles with momentum directed inward the system. It is clear that the emission function at these points is close to zero for such particles. Even formally, in the Gaussian approximation (5.34) for Q , validated in the region of its maximal value, the integral $\int_{t_\sigma}^{\infty} ds R(s, \mathbf{r} + \frac{\mathbf{p}}{p^0}(s - t_\sigma(\mathbf{r}, p)), p) \gg 1$, if particle world line crosses almost the whole system. The latter results in $Q \rightarrow 0$ and, therefore, completely destroys the saddle-point approximation (5.30) for Q and then the Cooper-Frye form (5.36) for spectra. Recall that if a particle crosses some non-space-like part of the hypersurface σ moving inward the system, this corresponds

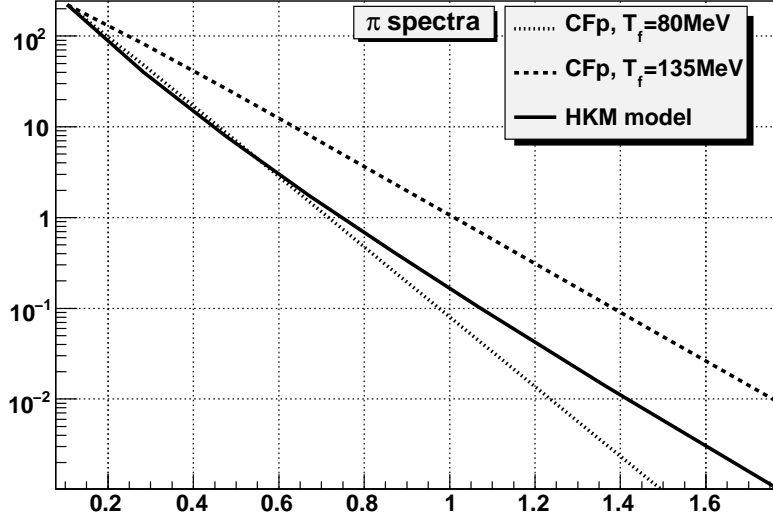


Figure 5.2: Transverse momentum spectrum of π^- in HKM, compared with the sudden freeze-out ones at temperatures of 80 and 160 MeV with arbitrary normalization.

to the condition $p^\mu d\sigma_\mu < 0$ [46]. Hence the value $p^\mu d\sigma_\mu(p)$ in the generalized Cooper-Frye formula (5.36) should be *always* positive: $p^\mu d\sigma_\mu(p) > 0$ across the hypersurface where fairly sharp maximum of emission of particles with momentum \mathbf{p} is situated; and so requirement $p^\mu d\sigma_\mu(p) > 0$ is a necessary condition for $t_\sigma(\mathbf{r}, p)$ to be a true hypersurface of the maximal emission. It means that hypersurfaces of maximal emission for a given momentum \mathbf{p} may be open in the space-time, not enclosing the high-density matter at the initial time t_0 , and different for different \mathbf{p} . All this is illustrated in Fig. 5.3, where the structure of particle emission domain is shown for two groups of particles. In the first one, the momentum is directed as the radius vector to the point of particle localization (they move outward the system), in the second one - in opposite direction (they move inward). The points of maximum for different p_T , where Cooper-Frye form can be applied, do not overlap. The calculations have been done in HKM [202].

Therefore, there are no negative contributions to the particle momentum density from non-space-like sectors of the freeze-out hypersurface, that is a well known shortcoming of the Cooper-Frye prescription [46, 47]; the negative contributions could appear only as a result of utilization of improper freeze-out hypersurface that roughly ignores its momentum dependence and so is common for all \mathbf{p} . If, anyhow, such a common hypersurface will be used, e.g. as the hypersurface of the maximal particle number emission (integrated over \mathbf{p}), there is no possibility to justify the approximate expression for momentum spectra similar to Eq. (5.36).

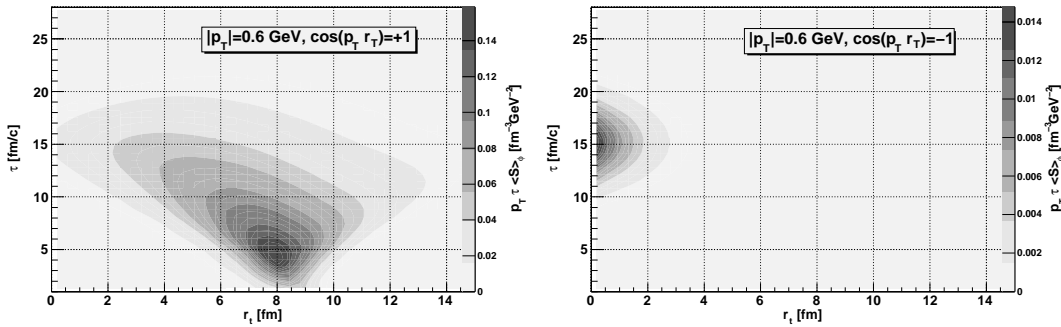


Figure 5.3: The emission function in HKM for particles with momentum directed along the radius vector at the emission points (left) and for those ones in the opposite direction to the radius vector (right).

5.4 Initial conditions for hydro-evolution of thermal matter

Starting from this section, the hydro-kinetic model (HKM) application to dynamics of A+A collisions is described. The basic hydrokinetic code, described above, is modified now to include realistic features of nucleus-nucleus collisions: initial conditions from initial state models, realistic equation of state, resonance decays, collision rates. Essentially, the model is applied to central A+A collisions.

Our results are all related to the central rapidity slice where we use the boost-invariant Bjorken-like initial condition in longitudinal direction. We consider the proper time of thermalization of quark-gluon matter as the minimal one discussed in the literature, $\tau_0 = 1$ fm/c [209].

We start the whole model description from initial conditions.

5.4.1 Pre-thermal flows

If one starts the hydrodynamic evolution at the "conventional time" $\tau_i = 1$ fm/c *without* transverse flow - since no pressure is established before thermalization - the resulting radial flow will not be developed enough to describe simultaneously the absolute values of pion, kaon and proton spectra, as well as the anisotropy of elliptic flow in non-central collisions. To describe the observables one needs to start the hydro-evolution at very small initial time, $\tau \sim 0.5$ fm/c [13], where it is difficult to expect the thermalization. This controversial situation is overcome due to the results of Ref. [210] where it is shown that the initial transverse flows in thermal matter as well as their anisotropy, leading to asymmetry of the transverse momentum spectra in non-central collisions, could be developed at the pre-thermal,

either classical field (Glasma) [211], string [141] or partonic stages, with even more efficiency than in the case of very early hydrodynamics. So, the hypothesis of early thermalization at times less than 1 fm/c is not necessary: the radial and elliptic flows develop no matter whether a pressure already established. The general reason for them is an essential finiteness of the system in transverse direction. Then the flows of particle number or energy directed outward the system cannot be compensated by the inward directed (from periphery to the center) flows. This difference means the non-zero net flows no matter how the collective velocity is defined: according to Ekkart or to Landau-Lifshitz. The further development and exploitation of these results were done in Refs. [212, 6, 213].

The initial transverse rapidity profile is supposed to be linear in radius r_T :

$$y_T = \alpha \frac{r_T}{R_T}, \quad \text{where} \quad R_T = \sqrt{\langle r_T^2 \rangle}, \quad (5.37)$$

here α is the second fitting parameter. Note that the fitting parameter α should include also a positive correction for underestimated resulting transverse flow since in this work we did not account in direct way for the viscosity effects [208] neither at QGP stage nor at hadronic one. In formalism of HKM [202] the viscosity effects at hadronic stage are incorporated in the mechanisms of the back reaction of particle emission on hydrodynamic evolution which we ignore in current calculations. Since the corrections to transverse flows which depend on unknown viscosity coefficients are unknown, we use fitting parameter α to describe the "additional unknown portions" of flows, caused by both factors: by a developing of the pre-thermal flows and the viscosity effects in quark-gluon plasma.

5.4.2 Glauber-like initial transverse profile

A simple Glauber model initialization assumes that the initial energy density in the transverse plane is proportional to the participant nucleon density [214],

$$\epsilon(\mathbf{b}, \mathbf{x}_T) = \epsilon_0 \frac{\rho(\mathbf{b}, \mathbf{x}_T)}{\rho_0} \quad (5.38)$$

with $\rho_0 \equiv \rho(0, 0)$ and

$$\rho(\mathbf{b}, \mathbf{x}_T) = (T(\mathbf{x}_T + \mathbf{b}/2)S(\mathbf{x}_T - \mathbf{b}/2) + T(\mathbf{x}_T - \mathbf{b}/2)S(\mathbf{x}_T + \mathbf{b}/2)),$$

$$S(\mathbf{x}_T) = \left[1 - \left(1 - \sigma_{NN} \frac{T(\mathbf{x}_T)}{A} \right)^A \right], \quad (5.39)$$

where A is atomic number, equal to 197 for Au+Au collision, and $\sigma_{NN} = 51 \text{ mb}(=5.1 \text{ fm}^2)$ is the nucleon-nucleon cross-section at $\sqrt{s_{NN}} = 200 \text{ AGeV}$. The impact parameter

$\mathbf{b} = (b, 0)$ is equal to zero, $b=0$, in the considered case of central collision. The parameter $\epsilon_0 \equiv \epsilon(b=0, \mathbf{x}_T=0)$ is the maximal energy density at the initial moment of thermalization. The thickness $T(\mathbf{x}_T)$ is expressed through the Woods-Saxon distribution profile:

$$T(\mathbf{x}_T) = \int_{-\infty}^{\infty} F_{\text{WS}}(\mathbf{x}) dx_L, \quad (5.40)$$

where

$$F_{\text{WS}}(\mathbf{x}) = \frac{a}{\exp \left[\left(\sqrt{x_L^2 + x_T^2} - R_A \right) / \delta \right] + 1}. \quad (5.41)$$

Here we use that $R_A = 1.12A^{1/3} - 0.86A^{-1/3} \approx 6.37$ fm, $\delta = 0.54$ fm. Constant a is obtained from normalization condition:

$$\int T(\mathbf{x}_T) d^2x_T = A. \quad (5.42)$$

One can think that transversal Glauber-like ϵ -profile has been formed to some initial time $\tau_0 \approx 0.1 - 0.3$ fm/c (see below) when the system is not thermal yet. However, the form of the profile is, practically, not modified to supposed thermalization time $\tau_0 \sim 1$ fm/c because the transverse velocities reached to this time are relatively small. At the same time, the absolute values of energy density can change significantly because of the strong longitudinal expansion. We use the maximal energy density ϵ_0 at time $\tau_i = 1$ fm/c as the second fitting parameter.

5.4.3 Initial conditions motivated by Color Glass Condensate model

Within CGC effective field theory some important physical properties of the field are defined by the parameter $\Lambda_s = g^2 \mu$ where $g^2 = 4\pi\alpha_s$ and μ^2 is dimensionless parameter, which is the variance of the Gaussian weight over the color charges ρ of partons. The value of Λ_{s0} is approximately equal to the saturation scale value, Q_s , and for the RHIC energies one can use $\Lambda_{s0} \approx Q_s \approx 2$ GeV² [215]. According to the results of Refs. [216, 217], (proper) time $\tau_0 \approx 3/\Lambda_s$ is an appropriate scale controlling the formation of gluons with a physically well-defined energy. At later times the dynamics of the classical Yang-Mills fields produced in nucleus-nucleus collisions can be linearized and approximated by that of a system of weakly coupled harmonic oscillators. Then one can compute the field amplitudes squared in momentum space and find corresponding distribution for the gluon number [217, 218] for cylindrically homogeneous transverse profile. It has the form at $p_T < 1.5\Lambda_s$

and $\eta = \frac{1}{2} \ln \frac{t+x_L}{t-x_L} \simeq 0$,

$$\begin{aligned} \frac{dN}{d^2p_T d^2x_T d\eta} &\equiv f(T_{\text{eff}}) \\ &= \frac{a_1}{g^2} \left[\exp \left(\sqrt{p_T^2 + m_{\text{eff}}^2} / T_{\text{eff}} \right) - 1 \right]^{-1}, \end{aligned} \quad (5.43)$$

where $m_{\text{eff}} = a_2 \Lambda_{s0}$, $T_{\text{eff}} = a_3 \Lambda_s$; $a_2 = 0.0358$, $a_3 = 0.465$. The constant a_1/g^2 will be absorb into factor ϵ_0 which is our fitting parameter.

The dependence of the distribution (5.43) on transverse coordinates \mathbf{x}_T is constructed as follows [217]:

$$\Lambda_s^2(\mathbf{x}_T) = \Lambda_{s0}^2 \frac{\rho(\mathbf{b}, \mathbf{x}_T)}{\rho_0}. \quad (5.44)$$

where the participant density at a particular position in the transverse plane is defined by (5.39).

To define the initial energy density profile we need the partonic phase-space distribution $f_0(x, p) = dN/d^3x d^3p$. Note, that it is associated with the hypersurfaces $t = \text{const}$. To express the phase-space density through the values $\frac{dN}{d^2x_T d^2pd\eta}$ defined at $\sqrt{t^2 - x_L^2} = \tau_0$, one should take into account that the density of partons with momentum \mathbf{p} crossing element $d^3\sigma(x)$ of this hypersurface is

$$\begin{aligned} p^0 \frac{dN}{d^3p} \Big|_{d\sigma(x)} &= p^\mu d\sigma_\mu(x) f_0(x, p) \\ &= f_0(x, p) \tau_0 p_T \cosh \theta d^2x_T d\eta, \end{aligned} \quad (5.45)$$

where $\theta = y - \eta$, y is rapidity of partons (in momentum space). Therefore

$$f_0(x, p) = \frac{1}{\tau_0 m_T \cosh \theta} \frac{dN}{d^2x_T d^2p_T d\eta dy}. \quad (5.46)$$

One can formally get the d^6N distribution from (5.43) by multiplying it by δ -function:

$$\frac{dN}{d^2p_T d^2x_T d\eta dy} = f(T_{\text{eff}}) \delta(y - \eta). \quad (5.47)$$

Such a phase-space distribution, corresponding the CGC asymptotic results [219], is widely used for a description of the initial state in A+A collisions [220]. However, a presence of the delta-function in the phase-space density contradicts evidently to the basic principle of the quantum mechanics. Indeed, the classical phase-space density has to follow from the quantum mechanical one in some limit. The Wigner function $f_W(x, p)$ [221], that is the quantum mechanical analog of the classical phase-space density $f(x, p)$, satisfies the restriction $\int f_W^2(x, p) d^3p d^3x \leq$

$(2\pi\hbar)^{-3}$ (see e.g. [222], note that the equality takes place for a pure state only), here the normalization condition $\int f_W(x, p)d^3pd^3x = 1$ is supposed. It evidently excludes utilization of the delta-function as factor in the structure of the Wigner function. Therefore, in order to escape contradiction with quantum mechanics, another prescription, instead of utilization of delta function, should be used for the longitudinal part of distribution $f(x, p)$; it can be, for example, the boost-invariant prescriptions used in Ref. [213]. Following to this receipt we smear the δ -function at hypersurface τ_0 in (5.47) as follows

$$\frac{dN}{d^2p_T d^2x_T d\eta dy} = f\left(\frac{T_{\text{eff}}}{\cosh(\eta - y)}\right). \quad (5.48)$$

In this way we fix the phase-space density (5.46). This may correspond to quasi-thermal averaged partonic distribution which can be reached at moment τ_0 due to quantum effects (uncertainly principle), different kind of turbulences and Schwinger-like mechanism of pair production in the pulse of strong color field. It does not mean that the true thermalization which should be supported by a permanent mechanism of partonic interactions is reached at $\tau_0 \approx 3/\Lambda_s \approx 3 \text{ fm}/c$.

As a result we use the following form of boost-invariant phase-space distribution for gluons at the initial hypersurface τ_0 :

$$f_0 = g^{-2} \frac{a_1(\tau_0 m_T \cosh \theta)^{-1}}{\exp\left(\sqrt{m_{\text{eff}}^2(\mathbf{x}_T) + p_T^2} \cosh \theta / T_{\text{eff}}(\mathbf{x}_T)\right) - 1}, \quad (5.49)$$

here $\theta = \eta - y$, $\mathbf{x}_T = (X, Y) = (x_T \cos \varphi, x_T \sin \varphi)$ and we consider gluons as massless particles, $m_T = p_T$. Such a distribution depends on the effective mass $m_{\text{eff}}(\mathbf{x}_T) = a_2 \Lambda_s(\mathbf{x}_T)$ and the temperature $T_{\text{eff}}(\mathbf{x}_T) = a_3 \Lambda_s(\mathbf{x}_T)$ (numerical values for a_2 and a_3 are the same as in Eq. (5.43)), which, in accordance with Ref. [217], are determined by the local scale $\Lambda_s(\mathbf{x}_T)$ (5.44).

The components of the energy-momentum tensor in the pseudo-Cartesian coordinates reads

$$T^{\mu\nu}(x) = \int p^\mu p^\nu f(x, p) p_T dp_T dy d\phi, \quad (5.50)$$

where the Lorentz-invariant integration measure d^3p/p_0 in the Cartesian variables is already re-written in Björken variables as $p_T dp_T dy d\phi$.

We numerically calculate the components of the energy-momentum tensor with the distribution function, following from Eq. (5.49), at $\eta = 0$.

Note that, at $\tau = \tau_0$, the energy-momentum tensor takes the form

$$T_0^{\mu\nu}(\mathbf{x}_T, x_L = 0) = \frac{a_1}{g^2 \tau_0} \Lambda_s^3(\mathbf{x}_T) t^{\mu\nu}, \quad (5.51)$$

where $t^{\mu\nu}$ are the constant coefficients fixed by the constants a_2 and a_3 . Therefore, the energy profile in transverse plane at τ_0 in central collisions can be presented in the form (see (5.44))

$$\epsilon(x_T) = \epsilon_0 \frac{\rho^{3/2}(0, x_T)}{\rho_0^{3/2}}, \quad (5.52)$$

where the number of participants is defined by (5.39). Under the same reason as for the Glauber-like IC we use the form of this profile to build the IC for hydrokinetic evolution at the thermalization time $\tau_i = 1$ fm/c. The maximal energy density ϵ_0 at (proper) time τ_i is the fitting parameter as in the case of the Glauber IC.

5.5 The thermal matter in A+A collision and equation of state

Here we describe the matter properties and its thermodynamic characteristics, e.g. equation of state, that are necessary components of the hydrokinetic model. We suppose that soon after thermalization the matter created in A+A collision at RHIC energies is in the quark gluon plasma (QGP) state. Also at time τ_i , there is a peripheral region with relatively small initial energy densities: $\epsilon(r) < 0.5$ GeV/fm³. This part of the matter ("corona") does not transform into QGP and has no chance to be involved in thermalization process [149]. By itself the corona gives no essential contribution to the hadron spectra [149]. One should consider it separately from the thermal bulk of the matter and should not include in hydrodynamic evolution. Therefore we cut the initial Glauber or CGC-like profiles at $\epsilon(r) \leq 0.5$ GeV/fm³ when consider IC for hydrodynamic evolution of the system.

During the system evolution the QGP is cooling and finally transforms into hadron phase, most probably, according to the crossover scenario. Such a transformation may occur in the interval of the temperatures 170-190 MeV. At the temperature $T = T_{ch} \approx 165$ MeV the chemical freeze-out happens, as demonstrates an analysis of the particle number ratios [223, 110]. The conception of the chemical freeze-out means that at the temperatures $T \geq T_{ch}$ the bulk of the expanding matter is in the local thermal and chemical equilibrium while at $T < T_{ch}$ the chemical composition becomes in some sense frozen: one can neglect the majority of inelastic reactions except for decays of resonances and recombination processes. The hadronic matter in the later thermodynamic region is not in the chemical equilibrium, moreover, the hadronic medium gradually emits particles being in this zone and, so, loose, in addition, also the local thermal equilibrium. Therefore, one should consider in different ways the matter evolution in the two 4D space-time zones separated by the 3D hypersurface corresponding to the isotherm

$T = T_{ch} \approx 165$ MeV. Let us describe the thermodynamic properties of matter in both these regions.

5.5.1 The EoS in the equilibrated space-time domain.

At high temperatures corresponding to the QGP phase and crossover transition to hadron phase we use a realistic EoS [225] adjusted to the lattice QCD results for zero baryonic chemical potential so that it is matched with an ideal chemically equilibrated multicomponent hadron resonance gas at $T_c = 175$ MeV. To take into account a conservation of the net baryon number, electric charge and strangeness in the QGP phase, one has first to make corrections to thermodynamic quantities for nonzero chemical potentials. As it is proposed in [226], a modification of the EoS can be evaluated by using of the Taylor series expansion in terms of the light and strange quark chemical potentials, or analogously in baryon and strange hadronic chemical potentials:

$$\frac{p(T, \mu_B, \mu_S)}{T^4} = \frac{p(T, 0, 0)}{T^4} + \frac{1}{2} \frac{\chi_B}{T^2} \left(\frac{\mu_B}{T}\right)^2 + \frac{1}{2} \frac{\chi_S}{T^2} \left(\frac{\mu_S}{T}\right)^2 + \frac{\chi_{BS}}{T^2} \frac{\mu_B}{T} \frac{\mu_S}{T} \quad (5.53)$$

The expansion coefficients χ_B and χ_S are the baryon number and strangeness susceptibilities which are related to thermal fluctuations of baryon number and strangeness in a thermal medium at zero chemical potentials.

To obtain the EoS in the equilibrium zone we use the numerical results for χ_B and χ_S as a function of the temperature given in [226]. The values for the ratios μ_q/T in (5.53) during the system evolution can be determined approximately. If at some hypersurface corresponding to an isotherm, like as at the chemical freeze-out hypersurface, the chemical potentials are uniform, then the following ratios remain constant

$$\frac{\mu_q}{T} = const_q, \quad \text{where } q = B, S, E$$

during the chemically equilibrated isentropic evolution of the Boltzmann massless gas. In our approximation we use these constraints and find the corresponding constants from the chemical potentials obtained together with T_{ch} from an analysis of the particle number ratios. In concrete calculations we use the chemical freeze-out temperature $T_{ch} = 165$ MeV, corresponding chemical potentials $\mu_B = 29$ MeV, $\mu_S = 7$ MeV, $\mu_E = -1$ MeV and also the strangeness suppression factor $\gamma_S = 0.935$ which are dictated by 200A GeV RHIC particle number ratios analysis done in the statistical model [223, 110].

5.5.2 The EoS in the chemically non-equilibrated domain.

At the chemical freeze-out temperature T_{ch} the "lattice" EoS taken from [225] and corrected for non-zero chemical potentials is matched with good accuracy

with ideal Boltzmann hadronic resonance gas which includes $N = 359$ hadron states made of u, d, s quarks with masses up to 2.6 GeV. Essentially, we use the same particle set in the FASTMC event generator [227]. Technically, in the numerical code, we input the corresponding N functions - the densities n_i of each hadron i and the equations for n_i already at the very beginning of the system evolution; however, these densities are meaningless in the QGP phase and their evaluation does not influence the system evolution in the equilibrated zone. These functions are brought into play at $T < T_{ch}$. If this thermodynamic region would correspond to the complete conservation of the particle numbers then, in addition to the energy-momentum conservation, one would account for the conservation equations for particle number flows in the form:

$$\partial_\mu(n_i u^\mu) = 0, \quad i = 1 \dots N \quad (5.54)$$

In our problem, however, during the system evolution in the non-equilibrated zone $T < T_{ch}$ the resonance decays have to be taken into account. The decay law in a homogeneous medium with $T \ll m_i$ (m_i is the resonances mass) implies a summing up of a decrease of unstable i th particle number due to decays and an increase because of decays of heavier j th resonance into i th particle:

$$\frac{dN_i}{dt} = -\Gamma_i N_i + \sum_j b_{ij} \Gamma_j N_j \quad (5.55)$$

where Γ_i is the total width of resonance i , $b_{ij} = B_{ij} M_{ij}$ denote the average number of i th particles coming from arbitrary decay of j th resonance, $B_{ij} = \Gamma_{ij}/\Gamma_{j,tot}$ is branching ratio, M_{ij} is a number of i th particles produced in $j \rightarrow i$ decay channel. The set on N equations (5.55), solved together, takes into account all possible cascade decays $i \rightarrow j \rightarrow k \rightarrow \dots$. This also conserves net charges, e.g. baryon, electric charge and strangeness, since the charges are conserved in resonance decay process. If one relates the Eq. (5.55) to the fluid element of some volume ΔV moving with four-velocity u^μ , then a covariant relativistic extension of the decay law for a hydrodynamic medium leads to the equation (5.54):

$$\partial_\mu(n_i(x) u^\mu(x)) = -\Gamma_i n_i(x) + \sum_j b_{ij} \Gamma_j n_j(x) \quad (5.56)$$

when one neglects a thermal motion of the resonance j , that can be justified because post (chemical) freeze-out temperatures are much less than the mass of the lightest known resonance. Also, Eq. (5.56) for the hydrodynamic evolution is written under supposition of an instant thermalization of the decay products, that is consistent with the ideal fluid approximation (mean free path is zero). In the kinetic part of the HKM we consider the next approximation when the non-equilibrium character of the distribution functions and the kinetics of resonance

decays are taken into account. We also can approximately account for a recombination in the processes of resonance decays into expanding medium just by utilizing the effective decay width $\Gamma_{i,eff} = \gamma\Gamma_i$ in Eq. (5.56). We use $\gamma = 0.75$ [228] for the resonances containing u and d quarks supposing thus that about 30% of such resonances are recombining during the evolution.

The equations (5.56) together with the hydrodynamic equations and the equation of state should give one the energy density and composition of the gas in each space-time points. To find the EoS $p = p(\epsilon, \{n_i\})$ for the mixture of hadron gases we start with the expressions for energy density and particle density for i th component of multicomponent Boltzmann gas :

$$\begin{aligned}\epsilon_i &= \frac{g_i}{2\pi^2} m_i^2 T (3TK_2(m_i/T) + mK_1(m_i/T)) \exp(\mu_i/T) \\ n_i &= \frac{g_i}{2\pi^2} m_i^2 T K_2(m_i/T) \exp(\mu_i/T).\end{aligned}\quad (5.57)$$

Then, the equation for the temperature is:

$$\epsilon = 3nT + \sum_i n_i m_i \frac{K_1(m_i/T)}{K_2(m_i/T)}, \quad (5.58)$$

where $n = \sum_i n_i$. Having solved this equation numerically for given ϵ and $\{n_i\}$, we get the temperature and then find the pressure using simple relation for multicomponent Boltzmann gas:

$$p = nT \quad (5.59)$$

The equations (5.58), (5.59) define $p = p(\epsilon, \{n_i\})$.

Thus, we follow the evolution of all N densities of hadron species in hydro calculation, and compute EoS dynamically for each chemical composition of N sorts of hadrons in every hydrodynamic cell in the system during the evolution. Using this method, we do not limit ourselves in chemically frozen or equilibrated evolution, keeping nevertheless thermodynamically consistent scheme.

As it was mentioned before, we use the Boltzmann approximation in the EoS calculation to decrease computational time. However, for emission function and spectra calculation we use quantum Bose-Einstein/Fermi-Dirac distribution functions with chemical potentials calculated to give the same particle densities as in the Boltzmann case. We checked that the measure of relative divergence in the energy density if one uses the quantum distribution functions instead of the Boltzmann one, is not bigger than 3% in the thermodynamic region which is actually contributing to formation of hadronic spectra.

5.6 Kinetics in the non-equilibrium hadronic zone

To describe the non-equilibrium evolution and decay of hadronic system we start from the Boltzmann equations for the mixture of hadrons, most of which have finite lifetimes and decay widths compatible with particle masses. The set of such equations for i -components of the hadron resonance gas which account for the only binary interactions (elastic scattering) and resonance decays are:

$$\begin{aligned} \frac{p_i^\mu}{p_i^0} \frac{\partial f_i(x, p)}{\partial x^\mu} &= G_i^{scatt}(x, p) - L_i^{scatt}(x, p) + G_i^{decay}(x, p) - L_i^{decay}(x, p) \equiv \\ &\equiv G_i(x, p) - L_i(x, p). \end{aligned} \quad (5.60)$$

Here we ignore the processes of resonance recombination which is simpler to account phenomenologically (see the previous Section). The term gain (G) describes an income of the particles into phase-space point (x, p) due to scatters and resonance decays. The term *loss* (L) is related to a decrease of particles in the vicinity of the phase space point (x, p) due to re-scattering and decays of resonances. The *loss* term is proportional to the particle number density in the point x and so $L_i^{scatt}(x, p) = f_i R_i$, $L_i^{decay}(x, p) = f_i D_i$ where R is scattering rate, and D is decay rate. If one considers the equations for stable or quasi-stable particles, then $L_i^{decay}(x, p) = 0$ ($D_i \equiv 0$).

The method allowing to find the emission function of the hadrons based on the Boltzmann equations in the (generalized) relaxation time approximation was proposed in Refs. [199, 202]. Following this method we put: $J_i(x, p) \approx R_{i,l.eq.}(x, p)$, $G_i \approx R_{i,l.eq.}(x, p) f_{i,l.eq.}(x, p) + G_i^{decay}(x, p)$. The quantity $R(x, p) = \tau_{rel}^{-1}(x, p)$ is the inverse relaxation time, or collision rate in global reference frame. Then,

$$\begin{aligned} \frac{p^\mu}{p^0} \partial_\mu f_i(x, p) &= (f_i^{l.eq.}(x, p) - f_i(x, p)) R_i(x, p) + \\ &+ G_i^{decay}(x, p) - L_i^{decay}(x, p) \end{aligned} \quad (5.61)$$

The explicit form of $G_i^{decay}(x, p)$ term will be derived later. In the first approximation to hydro-kinetic evolution the parameters of the locally equilibrium distribution function $f_{i,l.eq.}(x, p)$, e.g. the temperature $T(x)$, chemical potentials $\mu_i(x)$ are determined by the hydrodynamic evolution. The details of hydrodynamic approach used in the model are described in the next section.

5.6.1 Emission functions in hyperbolic coordinates and spectra formation

All our results are related to the very central rapidity interval, $y \approx 0$, and we will use the boost-invariant approach to describe strong longitudinal matter expansion

observed at RHIC. For such an approach the hyperbolic coordinates in (t, x_L) directions are more suitable than the Cartesian ones. Then the kinetic equations take a form

$$\frac{1}{m_T \cosh y} \left(m_T \cosh \theta \frac{\partial}{\partial \tau} - \frac{m_T \sinh \theta}{\tau} \frac{\partial}{\partial \eta} + \vec{p}_T \frac{\partial}{\partial \vec{r}_T} \right) f_i(\tau, \theta, \mathbf{r}_T, \mathbf{p}_T) = \left[f_i^{l.eq.}(\tau, \theta, \mathbf{r}_T, \mathbf{p}_T) - f_i(\tau, \theta, \mathbf{r}_T, \mathbf{p}_T) \right] R_i(\tau, \theta, \mathbf{r}_T, \mathbf{p}_T) + G_i^{decay}(\tau, \theta, \mathbf{r}_T, \mathbf{p}_T) \quad (5.62)$$

where $\tau = \sqrt{t^2 - x_L^2}$ is a proper time, $m_T = \sqrt{m^2 + p_T^2}$ is a transverse mass, $\theta = \eta - y$, η is a space-time rapidity, defined above Eq. (5.43), and y is a particle rapidity.

The formal solutions of (5.62) correspond to the non-equilibrium distribution functions in expanding and decaying multi-hadronic system:

$$\begin{aligned} f_i(\tau, \theta, \mathbf{r}_T, \mathbf{p}_T) &= f_i^{l.eq.}(\tau_0, \theta^{(\tau_0)}(\tau), \mathbf{r}_T^{(\tau_0)}(\tau), \mathbf{p}_T) \times \\ &\times \exp \left(- \int_{\tau_0}^{\tau} \tilde{R}_i(s, \theta^{(s)}(\tau), \mathbf{r}_T^{(s)}(\tau), \mathbf{p}_T) ds \right) + \\ &+ \int_{\tau_0}^{\tau} d\lambda \left[f_i^{l.eq.}(\lambda, \theta^{(\lambda)}(\tau), \mathbf{r}_T^{(\lambda)}(\tau), \mathbf{p}_T) \tilde{R}_i(\lambda, \theta^{(\lambda)}(\tau), \mathbf{r}_T^{(\lambda)}(\tau), \mathbf{p}_T) + \right. \\ &\left. + \tilde{G}_i^{decay}(\lambda, \theta^{(\lambda)}(\tau), \mathbf{r}_T^{(\lambda)}(\tau), \mathbf{p}_T) \right] \exp \left(- \int_{\lambda}^{\tau} \tilde{R}_i(s, \theta^{(s)}(\tau), \mathbf{r}_T^{(s)}(\tau), \mathbf{p}_T) ds \right) \end{aligned} \quad (5.63)$$

here $\tilde{R}_i(\lambda, \theta, \mathbf{r}_T, \mathbf{p}_T) = \frac{\cosh y}{\cosh \theta} R_i(\lambda, \theta, \mathbf{r}_T, \mathbf{p}_T)$,

$$\tilde{G}_i^{decay}(\lambda, \theta, \mathbf{r}_T, \mathbf{p}_T) = \frac{\cosh y}{\cosh \theta} G_i^{decay}(\lambda, \theta, \mathbf{r}_T, \mathbf{p}_T).$$

Here we use the notation

$$\begin{cases} \sinh \theta^{(\tau_0)}(\tau) = \frac{\tau}{\tau_0} \sinh \theta \\ \mathbf{r}_T^{(\tau_0)}(\tau) = \mathbf{r}_T - \frac{\mathbf{p}_T}{m_T} (\tau \cosh \theta - \sqrt{\tau_0^2 + \tau^2 \sinh^2 \theta}) \end{cases} \quad (5.64)$$

The invariant value is $p^0 R_i(x, p) = p^{*0} R_i^*(x, p)$, where the asterisk * denotes a value in the local rest frame of the fluid element in point x , so

$$\tilde{R}_i(x, p) = \frac{\cosh y}{\cosh \theta} R_i(x, p) = \frac{\cosh y}{\cosh \theta} \frac{p^\mu u_\mu}{p^0} R_i^*(p, T) = \frac{p^\mu u_\mu}{m_T \cosh \theta} R_i^*(p, T) \quad (5.65)$$

To connect the formal solution (5.63) with observables, e.g. particle spectrum, we use the equality

$$p^0 \frac{d^3 n}{d^3 p} = \frac{d^2 n}{2\pi p_T dp_T dy} = \int_{\sigma_{out}} d\sigma_\mu p^\mu f(x, p) \quad (5.66)$$

where σ_{out} is a "distant" hypersurface of large $\tau = const$, where all the interactions among hadrons are ceased.

In what follows we use the variable substitution in the first term of (5.63) describing the "initial emission" :

$$\begin{cases} \sinh \theta = \frac{\tau_0}{\tau} \sinh \theta' \\ \mathbf{r}_T = \mathbf{r}'_T + \frac{\mathbf{p}_T}{m_T} (\tau \cosh \theta - \sqrt{\tau_0^2 + \tau^2 \sinh^2 \theta}) \end{cases} \quad (5.67)$$

and the substitution :

$$\begin{cases} \sinh \theta = \frac{\lambda}{\tau} \sinh \theta' \\ \mathbf{r}_T = \mathbf{r}'_T + \frac{\mathbf{p}_T}{m_T} (\tau \cosh \theta - \sqrt{\lambda^2 + \tau^2 \sinh^2 \theta}) \end{cases} \quad (5.68)$$

in the second term of (5.63) related to the "4-volume emission". After transformation to new variables $\{\tau, \theta', \vec{r}'\}$ we arrive at the result:

$$\begin{aligned} \int_{\sigma_{out}} d\sigma_\mu p^\mu f(x, p) &= \int_{\sigma_0} d\sigma_0^\mu p_\mu f_i^{l.eq.}(\tau_0, \theta', \mathbf{r}'_T, p) \times \\ &\times \exp \left(- \int_{\tau_0}^{\infty} \tilde{R}_i(s, \theta^{(s)}(\tau_0), \mathbf{r}'_T^{(s)}(\tau_0), \mathbf{p}_T) ds \right) + \\ &\int_{\tau_0}^{\tau} d\lambda \int_{\sigma(\lambda)} d\sigma_\mu(\lambda) p^\mu \left[f_i^{l.eq.}(\lambda, \theta', \mathbf{r}'_T, \mathbf{p}_T) \tilde{R}_i(\lambda, \theta', \mathbf{r}'_T, \mathbf{p}_T) + \right. \\ &\left. \tilde{G}_i^{decay}(\lambda, \theta', \mathbf{r}'_T, \mathbf{p}_T) \right] \exp \left(- \int_{\lambda}^{\infty} \tilde{R}_i(s, \theta^{(s)}(\lambda), \mathbf{r}'_T^{(s)}(\lambda), \mathbf{p}_T) ds \right) = p^0 \frac{d^3 N}{d^3 p} \end{aligned}$$

where $\sigma(\lambda)$ is $\tau = \lambda = const$ hypersurface, so $d\sigma_\mu(\lambda) p^\mu = \lambda m_T \cosh \theta' d\theta' d^2 \vec{r}'_T$. The exponential values in these expressions are the escape probabilities

$$\mathcal{P}(\tau, \mathbf{r}_T, \theta, \mathbf{p}_T) = \exp \left(- \int_{\tau}^{\infty} \tilde{R}_i(s, \theta^{(s)}(\tau), \mathbf{r}_T^{(s)}(\tau), \mathbf{p}_T) ds \right) \quad (5.69)$$

for particles with momentum p at space-time point $(\tau, \mathbf{r}_T, \eta = \theta + y)$ (in hyperbolic coordinates) to become free without any collision [199, 202].

In the expression above we can separate the 4-volume emission function

$$\begin{aligned} S_i(\lambda, \theta, \mathbf{r}_T, \mathbf{p}_T) &= \\ &= \left[f_i^{l.eq.}(\lambda, \theta, \mathbf{r}_T, p) \tilde{R}_i(\lambda, \theta, r_T, p) + \tilde{G}_i^{decay}(\lambda, \theta, \mathbf{r}_T, \mathbf{p}_T) \right] \mathcal{P}(\lambda, \mathbf{r}_T, \theta, \mathbf{p}_T) \end{aligned} \quad (5.70)$$

and the initial emission function:

$$S_{i,0}(\theta, \mathbf{r}_T, \mathbf{p}_T) = f_i^{l.eq.}(\tau_0, \theta, \mathbf{r}_T, \mathbf{p}_T) \mathcal{P}(\tau_0, \mathbf{r}_T, \theta, \mathbf{p}_T) \quad (5.71)$$

These expressions demonstrate obviously that the particle emission is formed by the particles which undergo their *last* interaction or are already free initially. These expressions for the hadron emission function are the basic functions for calculations of the single- and multi- particle spectra [199]. To evaluate these quantities for observed (quasi) stable particles one needs to find the term gain G_i^{decay} for resonance decays and the collision rates R_i .

5.6.2 Resonance decays in multi-component gas

We suppose that in the first (hydrodynamic) approximation the products of resonance decays which interact with medium are thermalized and they become free later, after the last collision with one of other particles. However, at the late stages of matter evolution the system becomes fairly dilute, so that some of these produced particles get a possibility to escape without any collisions: $\mathcal{P} > 0$. To describe this we use the following form for L_i^{decay} and G_i^{decay} terms (for 2-particle resonance decay) [229]:

$$\begin{aligned} p_i^0 L_i^{decay}(x, p_i) &= \sum_k \sum_l \int \frac{d^3 p_k}{p_k^0} \int \frac{d^3 p_l}{p_l^0} \Gamma_{i \rightarrow kl} f_i(x, p_i) \times \\ &\times \frac{m_i}{F_{i \rightarrow kl}} \delta^{(4)}(p_i - p_k - p_l) = m_i \Gamma_i f_i(x, p_i) \end{aligned} \quad (5.72)$$

where resonance i decays into particles or resonances k and l .

$$p_i^0 G_i^{decay}(x, p_i) = \sum_j \sum_k \int \frac{d^3 p_j}{p_j^0} \int \frac{d^3 p_k}{p_k^0} \Gamma_{j \rightarrow ik} f_j(x, p_j) \frac{m_j}{F_{j \rightarrow ik}} \delta^{(4)}(p_j - p_k - p_i) \quad (5.73)$$

where the resonance j decays into particles i and k with partial width $\Gamma_{j \rightarrow ik}$ for this decay channel, and

$$F_{j \rightarrow ik} = \int \frac{d^3 p_k}{p_k^0} \int \frac{d^3 p_i}{p_i^0} \delta^{(4)}(p_j - p_k - p_i) = \frac{2\pi}{m_j^2} ((m_j^2 - m_k^2 - m_i^2)^2 - 4m_i^2 m_k^2)^{1/2} \quad (5.74)$$

To escape the complicated problem of satisfying the thermodynamic identities in hadron resonance gas we utilize in what follows the mass shell approximation for resonances, supposing that $m_i = \langle m_i \rangle$. Also, as it was already discussed, we take into account that the resonance mass in hadron resonance gas is much larger than the temperature, $m_i \gg T_c$. Then the most probable velocity of resonance in the rest system of a fluid element is small, $\bar{v}_i \approx \sqrt{\frac{2T}{m_i}}$, and one can use the approximation

$$p_i^\mu \approx m_i u^\mu. \quad (5.75)$$

So the resonance distribution function takes the form

$$f_j(x, p_i) \approx \frac{p_j^0}{m_j} n_j(x) \delta^3(\mathbf{p}_j - m_j \mathbf{u}(x)), \quad (5.76)$$

It allows us to perform integrations in (5.73) over p_j, p_k analytically and get :

$$G_i^{decay}(x, p_i) = \sum_j \sum_k \Gamma_{j \rightarrow ik} \frac{n_j(x)}{p_i^0 p_k^0 F_{j \rightarrow ik}} \delta(m_j u^0(x) - p_k^0 - p_i^0) \quad (5.77)$$

where $p_k^0 = \sqrt{m_k^2 + (m_j \mathbf{u}(x) - \mathbf{p}_i)^2}$.

Just this form of gain term is used when spectra are evaluated according to Eq. (5.6.1). Note that in practical calculations we substitute δ -function by its Gaussian representation:

$$\delta(x) = \frac{1}{R\sqrt{\pi}} e^{-x^2/R^2}$$

and take a finite parameter value $R = 50 MeV$.

5.6.3 Collision rates

The collision rate $R(x, p) = \frac{1}{\tau_{rel}(x, p)}$ is one of the basic value for calculation of the intensity of the interactions in the expanding system and its decoupling. The latter is described through the escape probability $\mathcal{P}(x, p)$ (5.69) - the integral value of R along the possible trajectory of a particle with momentum p running freely through the whole expanding system. The rate of collisions in the rest frame of some fluid element that accounts for scatters of given particle with any other i th hadronic species in the thermal Boltzmann system depends only on particle energy $E_p^* = p^\mu u_\mu$ and the thermodynamic parameters of this fluid element [230]:

$$R^*(E_p^*, T, \{\mu_i\}) = \sum_i \int d^3 k_i \frac{g_i}{(2\pi)^3} \exp\left(-\frac{E_{k,i} - \mu_i(x)}{T(x)}\right) \times \\ \times \sigma_i(s_i) \frac{\sqrt{(s_i - (m - m_i)^2)(s_i - (m + m_i)^2)}}{2E_p^* E_{k,i}} \quad (5.78)$$

Here $g_i = (2j_i + 1)$, $E_p = \sqrt{\mathbf{p}^{*2} + m^2}$, $E_{k,i} = \sqrt{\mathbf{k}_i^2 + m_i^2}$, $s_i = (p^* + k_i)^2$ is the squared c.m. energy of the pair, and $\sigma_i(s)$ is the total cross section of selected particle with particle i in the corresponding binary collision. One can change the integration variable to squared center of mass energy s , energy of scattering partner E_k and momentum angle ϕ , and perform E_k and ϕ -integration analytically, which gives the expression for remaining integral:

$$R^*(E_p^*, T, \{\mu_i\}) = \sum_i \frac{g_i T e^{\mu_i/T}}{8\pi^2 p^* E_p^*} \int_{(m+m_i)^2}^{\infty} ds \sigma_i(s) \sqrt{(s - m^2 - m_i^2)^2 - 4m_i^2 m^2} \times \\ \times \sinh\left(\frac{p^*}{2Tm^2} \sqrt{(s - m^2 - m_i^2)^2 - 4m_i^2 m^2}\right) \exp\left(-\frac{(s - m^2 - m_i^2)E_p^*}{2Tm^2}\right) \quad (5.79)$$

We calculate $\sigma_i(s)$ in a way similar to UrQMD code [231]:

- Breit-Wigner formula is applied for meson-meson and meson-baryon scattering:

$$\sigma_{total}^{MB}(\sqrt{s}) = \sum_{R=\Delta, N^*} \langle j_B, m_B, j_M, m_M || J_R, M_R \rangle \frac{2S_R + 1}{(2S_B + 1)(2S_M + 1)} \\ \times \frac{\pi}{p_{cm}^2} \frac{\Gamma_{R \rightarrow MB} \Gamma_{total}}{(M_R - \sqrt{s})^2 + \Gamma_{tot}^2/4} \quad ,$$

where $\Gamma_{total} = \sum_{(\text{channels})} \Gamma_{R \rightarrow MB}$, with \sqrt{s} -dependent parametrization of partial decay widths:

$$\Gamma_{R \rightarrow MB}(M) = \Gamma_R \frac{M_R}{M} \left(\frac{p_{CMS}(M)}{p_{CMS}(M_R)} \right)^{2l+1} \frac{1.2}{1 + 0.2 \left(\frac{p_{CMS}(M)}{p_{CMS}(M_R)} \right)^{2l}}$$

chosen to depend on absolute value of particle momentum in two-particle rest frame:

$$p_{CMS}(\sqrt{s}) = \frac{1}{2\sqrt{s}} \sqrt{(s - m_1^2 - m_2^2)^2 - 4m_1^2 m_2^2}$$

In the case of meson-meson scattering a constant elastic cross section of 5 mb is added in order to fully reproduce the measured cross section.

- PDG table data for $p - p$, $p - n$, $p - \bar{p}$, etc. scattering
- other baryon-baryon scattering: additive quark model:

$$\sigma_{total} = 40 \left(\frac{2}{3} \right)^{m_1+m_2} \left(1 - 0.4 \frac{s_1}{3 - m_1} \right) \left(1 - 0.4 \frac{s_2}{3 - m_2} \right) [\text{mb}] \quad ,$$

$m_i = 1(0)$ corresponds to meson(baryon), s_i - number of strange quarks in hadron i .

Note that all relevant resonance states (see above), 359 different species - are taken into account for the calculation of $\sigma_i(s)$.

5.7 Hydrodynamics

We describe the system evolution in the equilibrium zone at $T > T_{ch}$ by the perfect hydrodynamics. The small shear viscosity effect, which leads to an increase of the transverse flows [208], is taken into account phenomenologically in the parameter α of initial velocity as described above.

The matter evolution in this zone is described by the relativistic hydrodynamical equations related to the conservation of energy-momentum, $\partial_\nu T^{\mu\nu} = 0$, together with the equations for particle number densities (5.56).

At $T < T_{ch}$ the equations for the system evolution in the first approximation ($f_i = f_i^{l.eq}$) can be derived from the basic equation (5.61). Namely, integrating the left and right hand sides of Eq.(5.61) over d^3p one arrives at equation (5.56) for particle number flow in the non-equilibrium zone, and also to hydrodynamic equation by integrating Eq. (5.61) over $p_i' d^3p_i$ and summing over index i .

Note that in this work we limit ourselves by the first approximation when the matter evolution is described by the equations of ideal hydrodynamics while the distribution function (5.63) in decaying system is non-equilibrium.

For the resolution of hydrodynamic equations we use essentially *the same* numerical algorithm as described in Section 4.3.1.

However, here for hydrodynamic calculations related to midrapidity region on central A+A collisions we impose longitudinal symmetry and cylindrical symmetry in transverse direction. This actually means that tangential (in transverse direction) and longitudinal velocities in LCMS vanish, so $Q_\phi = Q_\eta = 0$, as well as the fluxes in ϕ and η directions. Then, one has to solve the following set of equations :

$$\underbrace{\partial_\tau \begin{pmatrix} Q_\tau \\ Q_r \\ \{Q_{n_i}\} \end{pmatrix}}_{\text{quantities}} + \underbrace{\partial_r \cdot \begin{pmatrix} (Q_\tau + p)v_r \\ Q_r v_r + p \\ \{Q_{n_i} v_r\} \end{pmatrix}}_{\text{fluxes}} + \underbrace{\begin{pmatrix} (Q_\tau + p)(1 + v_\eta^2)/\tau - (Q_\tau + p)v_r/r \\ Q_r/\tau - Q_r v_r/r \\ \{Q_{n_i}/\tau - Q_{n_i} v_r/r\} \end{pmatrix}}_{\text{sources}} = 0 \quad (5.80)$$

Practically v_r/r is ambiguous at $r = 0$, so we put $v_r/r = \alpha$ there and use α value interpolated from the neighboring points.

Here the expression in curly brackets denote N variables associated with the particle densities for each sort of hadrons, as in (5.54).

Thus, hydrodynamic algorithm (Section 4.3.1) is modified to solve equations 5.80 instead of 4.15, and to account for additional N particle number densities.

5.8 Results: pion and kaon femtoscopy at top RHIC energy

Our goal here is to apply the hydrokinetic model for an analysis of the space-time picture of Au+Au collisions at the top RHIC energies. Such an analysis provided in the evolutionary models of heavy ion collisions should be based on a detailed description of the pion and kaon femtoscopic scales as well as on the description of the *absolute* values of the spectra (not only spectra slopes) of the particles. As it was noted in Ref. [202], the following factors are favored by the simultaneous description of the mentioned data: a relatively hard EoS (crossover transition between hadronic and quark-gluon matters, not the first order phase transition), the pre-thermal transverse flows developed prior the thermalization time, an account for an "additional portion" of the transverse flows due to the shear viscosity effect [208], a correct description of the gradual decay of the system at the late stage of the expansion. All these factors are included in the present version of the HKM.

We use both the Glauber-like (Section 5.4.2) and CGC-like (Section 5.4.3) initial conditions. In the former case the mean transverse radius, defined by (5.37) is $R_T = 4.137$ fm for the top RHIC energy. The best fit for the Glauber IC is reached at the following values of the two fitting parameters related to the proper time $\tau = 1$ fm/c: $\epsilon_0 = 16.5$ GeV/fm³ ($\langle\epsilon\rangle = 11.69$ GeV/fm³) and parameter of the initial velocity defined by (5.37), $\alpha = 0.248$ ($\langle v_T \rangle = 0.224$). In the case of the CGC-like initial conditions $R_T = 3.88$ fm, the fitting parameters leading to the best data description are $\epsilon_0 = 19.5$ GeV/fm³ ($\langle\epsilon\rangle = 13.22$ GeV/fm³) and $\alpha = 0.23$ ($\langle v_T \rangle = 0.208$). The parameters α for the initial transverse flows are somewhat larger than they are for the free streaming approximation of the pre-thermal stage [213]. The reason is, as it is explained in Section 5.4, that the fitting parameter α is related to the "unknown portions" of flows, caused by the two factors: a developing of the pre-thermal flows and the viscosity effects in the quark-gluon plasma. In addition, an account of the event-by-event fluctuations of the initial conditions also leads to an increase of the "effective" transverse flows, obtained by averaging at the final stage, as compared with the results based on the initial conditions averaged over initial fluctuations [232]. Since we use the later kind of IC, it should lead also to an increase of the effective parameter α .

As it was discussed in Section 5.5, the chemically non-equilibrated evolution at the late stage, $T < T_{ch} = 165$ MeV, is not characterized by a simple EoS,

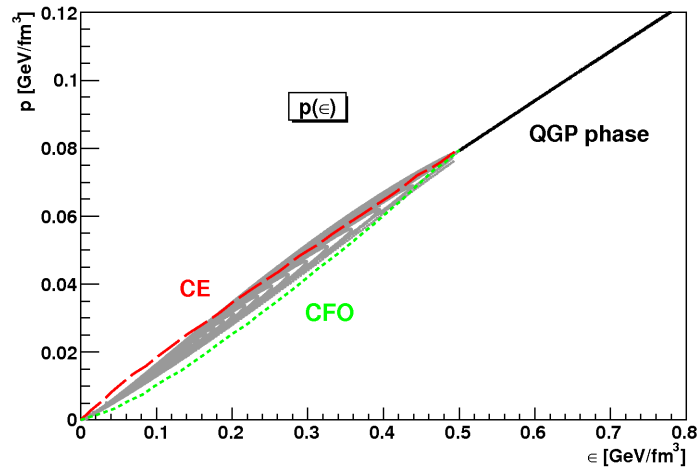


Figure 5.4: Equation of state $p(\epsilon)$ used in the HKM calculations. The solid black line is related to the chemically equilibrated phase, taken from lattice QCD results as described in Sec. IIIA, while grey region consists of set of the points corresponding to the different hadron gas compositions at each ϵ occurring during the late non-equilibrium stage of the evolution. The dashed line denotes EoS for the chemically equilibrated hadron gas and dotted line for the chemically frozen one, they are shown for a comparison.

like $p = p(\epsilon, \mu_B)$, in our calculations the pressure in this domain depends on 360 variables: energy density and particle concentrations. In Fig. 5.4 we demonstrate the "effective" EoS at the temperatures around and below T_{ch} . The points related to the latter region characterize all the range of the pressure gained at each energy density when the system evolves with the Glauber IC fixed above. We see that the pressure is different from the "limited" cases: the chemically equilibrated and completely chemically frozen evolution (when the numbers of *all* (quasi) stable particles and resonances are conserved). At relatively large energy densities the non-equilibrium EoS in a dominant space-time region is harder than even in the chemically equilibrated case. This could reduce the out- to side- ratio for transverse interferometry radii.

The results of the HKM for the pion and kaon spectra, interferometry radii and R_{out}/R_{side} ratio are presented in Fig. 5.5. Since the temperature and baryonic chemical potential at chemical freeze-out, which are taken from the analysis of the particle number ratios [223], are more suitable for the STAR experiment, the HKM results for kaon spectra are good for the STAR data but not so much for the PHENIX ones. Note also that, in spite of other studies (e.g., [191]), we compare our results for the interferometry radii within the whole measured interval of p_T covered at the top RHIC energy. Finally, one can conclude from Fig. 5.5 that the description of pion and kaon spectra and space-time scales is quite good for both IC, the Glauber and CGC. It is worth noting, however, that the two fitting parameters α and ϵ_0 vary by 10-20% for different IC, as it is described above.

The special attention acquires a good description of the pion and kaon longitudinal radii altogether with R_{out}/R_{side} ratio, practically, within the experimental errors. Such an achievement means that the HKM catches the main features of the matter evolution in A+A collisions and correctly reproduces the homogeneity lengths in the different parts of the system which are directly related to the interferometry radii at the different momenta of the pairs [9, 205]. In this connection it is valuable to show the structure of the emission function for pions and kaons.

In Fig. 5.6 we demonstrate the space-time structure of the particle emission at the Glauber IC for different transverse momenta of particles, longitudinal momenta is close to zero. The space-time picture of particle liberation is quite different for different transverse momenta: for the soft particles the maximal emission occurs close to the central part and happens at relatively later times, while the most of the hard particles are emitted from the periphery of the system at early times. In fact (see also [202, 233]), the temperatures in the regions of the maximal emission are quite different for different p_T , they are for pions: $T \approx 75 - 110$ MeV for $p_T = 0.2$ GeV/c and $T \approx 130 - 135$ MeV for $p_T = 1.2$ GeV/c. So, if one uses the generalized Cooper-Frye prescription [202, 233] applied to the *hypersurfaces of the maximal emission*, these hypersurfaces will be different for the different particle momenta

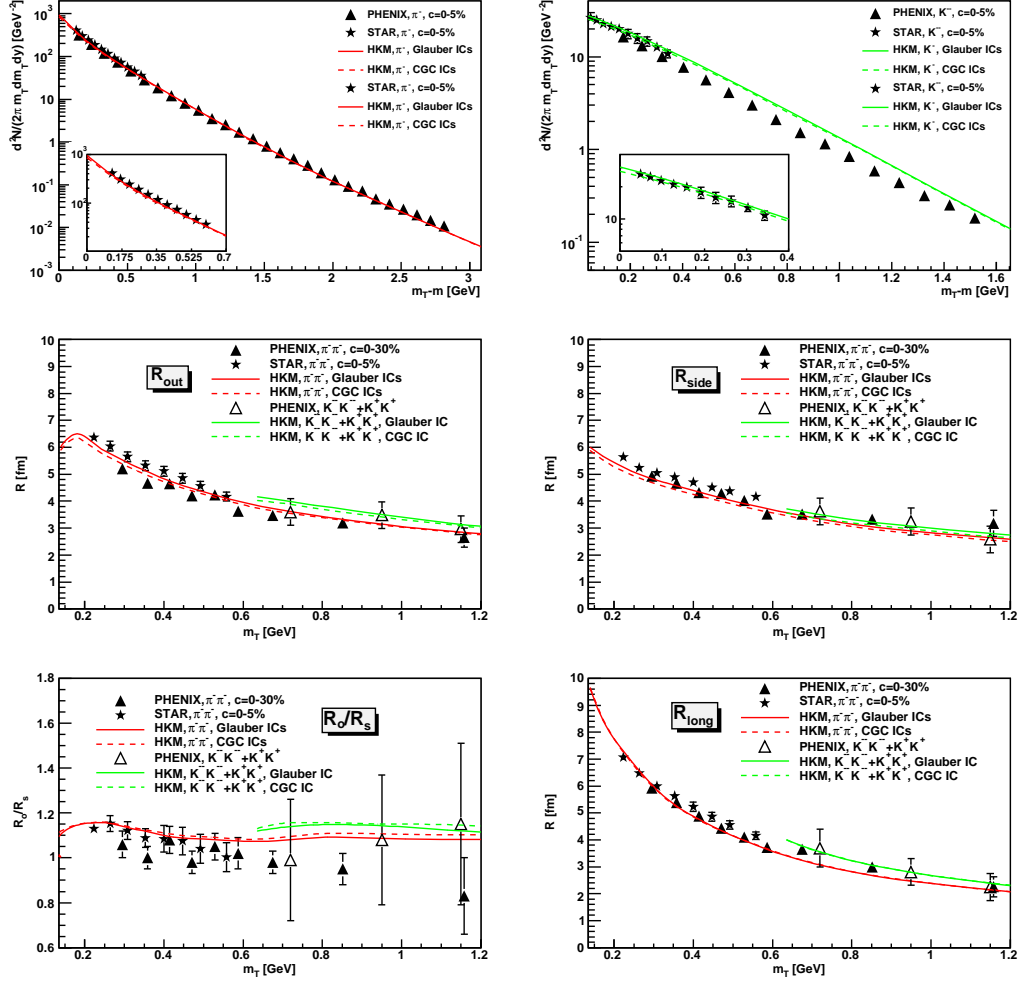


Figure 5.5: The transverse momentum spectra of negative pions and negative kaons, all calculated in the HKM model. The comparison only with the STAR data are presented in the separate small plots. (Top). The interferometry radii and R_{out}/R_{side} ratio for $\pi^- \pi^-$ pairs and mixture of $K^- K^-$ and $K^+ K^+$ pairs. (Middle and bottom). The experimental data are taken from the STAR [95, 77] and PHENIX [72, 235, 236] Collaborations.

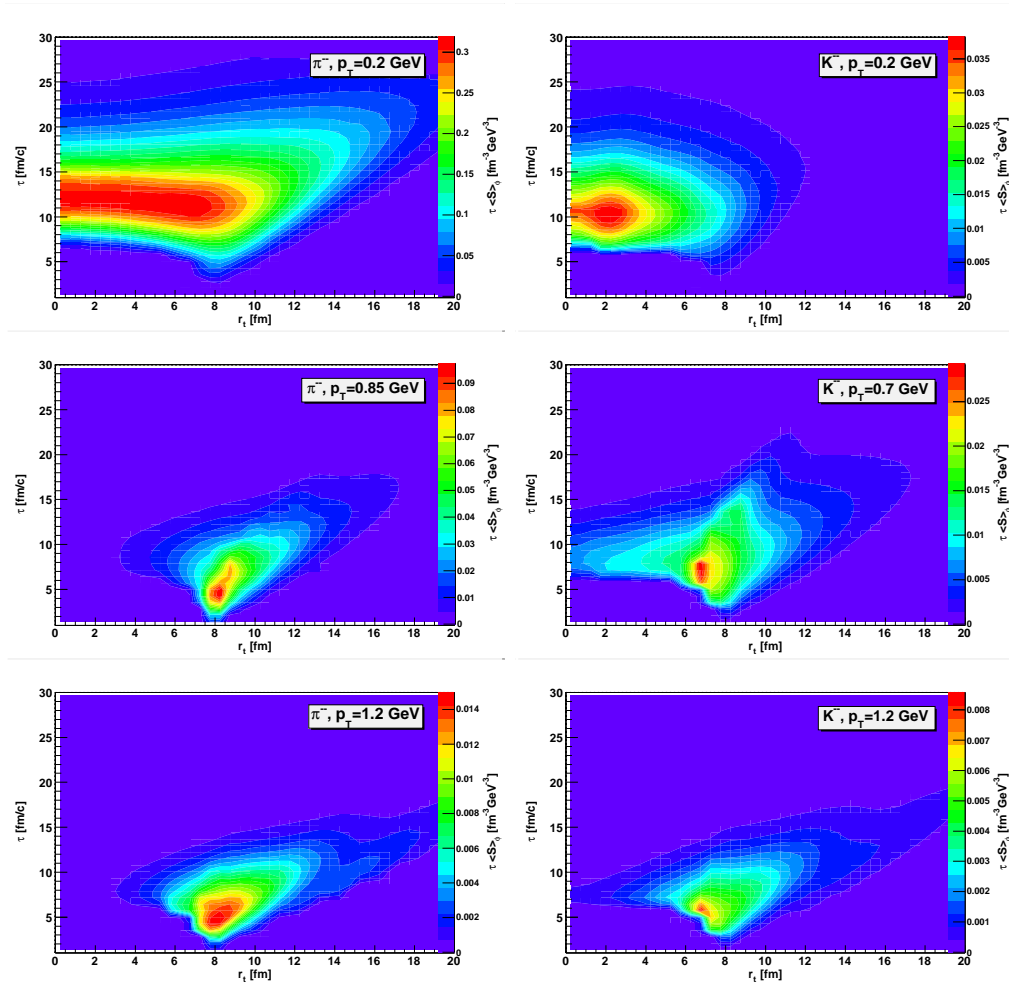


Figure 5.6: The ϕ_p -integrated emission functions of negative pions and negative kaons with different momenta at the Glauber IC. The values of p_T in the middle row correspond to the same transverse mass for pions and kaons $m_T = 0.86$ GeV.

and does not correspond to common isotherm [202, 233].

One can see in Fig. 5.6, the top plots, that at *equal* transverse momentum p_T the maximal emission of kaons happens earlier than pions as one can expect since the kaons interact weaker. At the same time the kaon interferometry radii in Fig. 5.5 follow approximately the pion radii, demonstrating the approximate m_T -scaling [234] with deviations to the slightly bigger values than pion radii have. The explanations can be gained from the middle row in Fig. 5.6 where the comparison is done for the same transverse mass of pions and kaons. Then the maxima of pion and kaon emissions become closer and the majority of kaons leave system even somewhat later than pions at the same m_T , opposite to the comparison at the same p_T . Since in simplest situations the homogeneity lengths for bosons depend on m_T [234], one could say that the approximate m_T -scaling could indicate the similarity of the freeze-out picture for kaons and pions. However, probably, such a conclusion is very approximate since the real structure of the emission processes in A+A collisions is quite complicated as one can see from the details in Fig. 5.6.

5.9 Results: space-time scales for SPS, RHIC, LHC

The above formulated model is then applied to the description of particle spectra and space-time scales observed at SPS and RHIC experiments.

The pion emission function per unit (central) rapidity, integrated over azimuthal angle and transverse momenta, is presented in Fig. 5.7 for the top SPS, RHIC and LHC energies as a function of transverse radius r and proper time τ . The two fitting parameters ϵ_0 and $\langle v_T \rangle$ are fixed as discussed above and marked in figures. The pion transverse momentum spectrum, its slope as well as the absolute value, and the interferometry radii, including R_{out} to R_{side} ratio, are in a good agreement with the experimental data both for the top SPS and RHIC energies.

As one can see particle emission lasts all the lifetime of the fireballs; in the central part, $\mathbf{r} \approx 0$, the duration is half of the lifetime. Nevertheless, according to the results above in this chapter, the Landau/Cooper-Frye prescription of sudden freeze-out could be applied in a generalized form accounting for momentum dependence of the freeze-out hypersurface $\sigma_p(x)$; now $\sigma_p(x)$ corresponds to the *maximum of emission function* $S(t_\sigma(\mathbf{r}, p), \mathbf{r}, p)$ at fixed momentum \mathbf{p} in an appropriate region of \mathbf{r} . This finding gives one possibility to keep in mind the known results based on the Cooper-Frye formalism, applying them to a surface of the maximal emission for given p . Then the typical features of the energy dependence can be understood as follows. The inverse of the spectra slopes, T_{eff} , grows with energy, since as one sees from the emission functions, the duration of expansion increases with initial

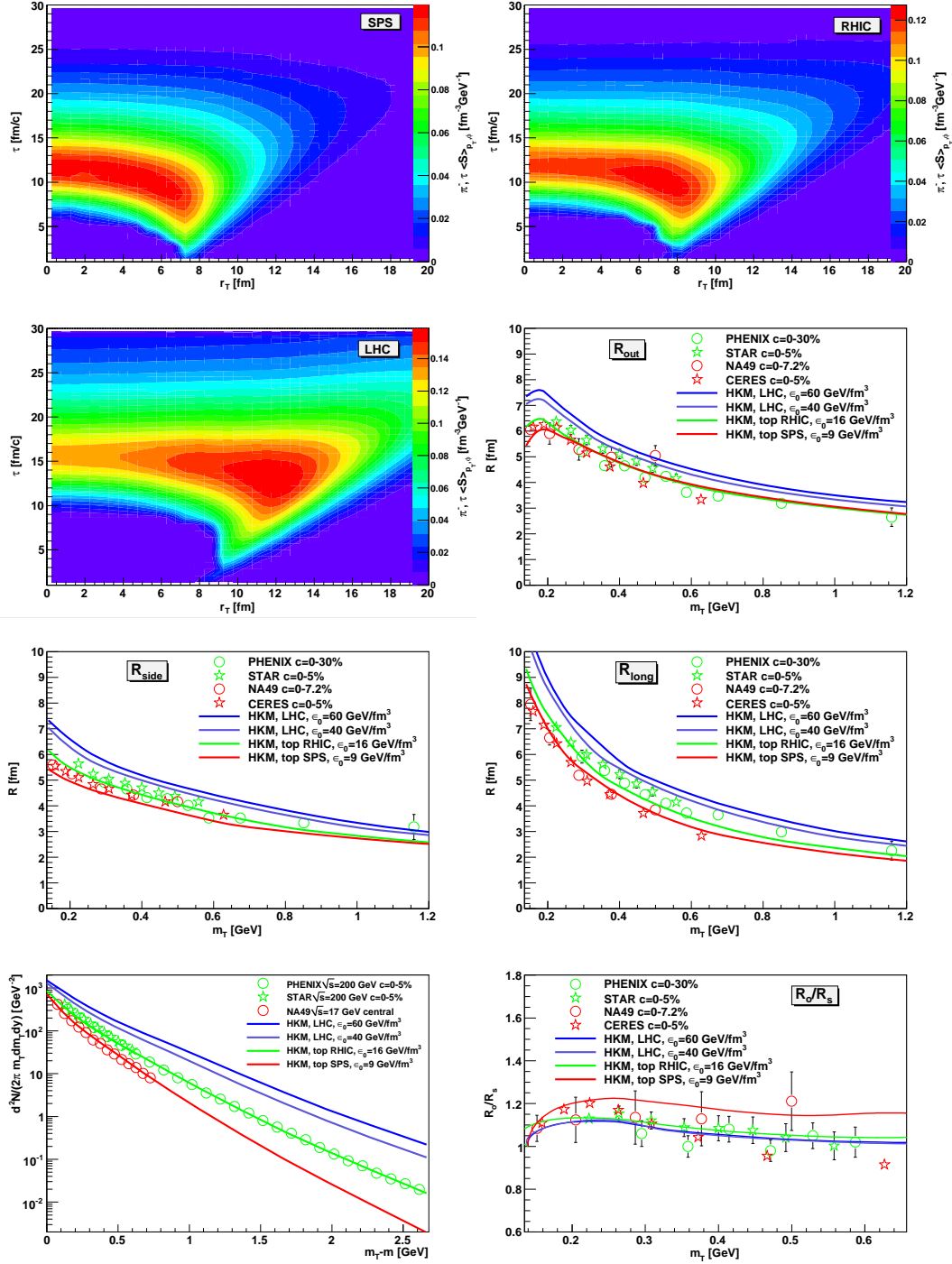


Figure 5.7: The p_T -integrated emission functions of negative pions for the top SPS, RHIC and LHC energies (top); the interferometry radii (middle) R_{out}/R_{side} ratio and transverse momentum spectra (bottom) of negative pions at different energy densities, all calculated in HKM model. The experimental data are taken from CERES [240] and NA-49 Collaborations [241, 242] (SPS CERN), STAR [95, 77] and PHENIX [72, 235] Collaborations (RHIC BNL)

energy density and, therefore, the fluid element get higher transverse collective velocities v_T when reaching a decoupling energy densities. Therefore the blue shift of the spectra becomes stronger. A rise of the transverse collective flow with energy leads to some compensation of an increase of R_{side} : qualitatively the homogeneity length at decoupling stage is $R_{side} = R_{Geom}/\sqrt{1 + \langle v_T^2 \rangle m_T/2T}$, (see, e.g., [237]). So, despite a significant increase of the transverse emission region, R_{Geom} , seen in Fig.1, a magnification of collective flow partially compensates this. As a result there is only a moderate increase of the R_{side} with energy. Since the temperatures in the regions of the maximal emission decrease very slowly when initial energy density grows (e.g., the temperatures for SPS, RHIC and LHC are correspondingly 0.105, 0.103 and 0.95 MeV for $p_T = 0.3$ GeV/c) the $R_{long} \sim \tau\sqrt{T/m_T}$ [234] grows proportionally to an increase of the proper time associated with the hypersurface $\sigma_{p_T}(x)$ of *maximal* emission. As we see from Fig. 5.5 this time grows quite moderately with the collision energy.

A non trivial result concerns the energy behavior of the R_{out}/R_{side} ratio. It slowly drops when energy grows and apparently is saturated at fairly high energies at the value close to unity (Fig.1). To clarify the physical reason of it let us make a simple semi-quantitative analysis. As one can see in Fig. 1, the hypersurface of the maximal emission can be approximated as consisting of two parts: the "volume" emission (V) at $\tau \approx const$ and "surface" emission (S). A similar picture within the Cooper-Frye prescription, which generalizes the blast-wave model by means of including the surface emission has been considered in Ref. [48]. If the hypersurface of maximal emission $\tilde{\tau}(r)$ is double-valued function, as in our case, then at some transverse momentum p_T the transverse spectra and HBT radii will be formed mostly by the two contributions from the different regions with the homogeneity lengths $\lambda_{i,V} = \sqrt{\langle (\Delta r_i)^2 \rangle}$ ($i = side, out$) at the V -hypersurface and with the homogeneity lengths $\lambda_{i,S}$ at the S -hypersurface. Similar to Ref.[237], one can apply at $m_T/T \gg 1$ the saddle point method when calculating the single and two particle spectra using the boost-invariant measures $\mu_V = d\sigma_\mu^V p^\mu = \tilde{\tau}(r)rdrd\phi d\eta(m_T \cosh(\eta - y) - p_T \frac{d\tilde{\tau}(r)}{dr} \cos(\phi - \alpha))$ and $\mu_S = d\sigma_\mu^S p^\mu = \tilde{\tau}(\tau)\tau d\tau d\phi d\eta(-m_T \cosh(\eta - y) \frac{d\tilde{\tau}(\tau)}{d\tau} + p_T \cos(\phi - \alpha))$ for V - and S - parts of freeze-out hypersurface correspondingly (here η and y are space-time and particle pair rapidities, the similar correspondence is for angles ϕ and α , also note that $\frac{p_T}{m_T} > \frac{d\tilde{\tau}(\tau)}{d\tau}$ [202, 233]). Then one can write, ignoring for simplicity the interference (cross-terms) between the surface and volume contributions,

$$R_{side}^2 = c_V^2 \lambda_{side,V}^2 + c_S^2 \lambda_{side,S}^2 \quad (5.81)$$

$$R_{out}^2 = c_V^2 \lambda_{out,V}^2 + c_S^2 \lambda_{out,S}^2 \left(1 - \frac{d\tilde{\tau}}{d\tau}\right)^2, \quad (5.82)$$

where the coefficients $c_V^2 + c_S^2 \leq 1$ and we take into account that at $p^0/T \gg 1$ for

pions $\beta_{out} = p_{out}/p^0 \approx 1$. All homogeneity lengths depend on mean transverse momentum of the pion pairs p_T . The slope $\frac{d\tilde{r}}{d\tau}$ in the region of homogeneity expresses the strength of $r - \tau$ correlations between the space and time points of particle emission at the S -hypersurface $\tilde{r}(\tau)$. The picture of emission in Fig. 1 shows that when the energy grows the correlations between the time and radial points of the emission becomes positive, $\frac{d\tilde{r}}{d\tau} > 0$, and they increase with energy density. The positivity is caused by the initial radial flows [212] $u^r(\tau_0)$, which are developed at the pre-thermal stage, and the strengthening of the $r - \tau$ correlations happens because the non-central i th fluid elements, which produce after their expansion the surface emission, need more time $\tau_i(\epsilon_0)$ to reach the decoupling density if they initially have higher energy density ϵ_0 . (Let us characterize this effect by the parameter $\kappa = \frac{d\tau_i(\epsilon_0)}{d\epsilon_0} > 0$). Then the fluid elements before their decays run up to larger radial freeze-out position r_i : if a is the average Lorentz-invariant acceleration of those fluid elements during the system expansion, then roughly for i th fluid elements which decays at time τ_i we have at $a\tau_i \gg 1$: $r_i(\tau_i) \approx r_i(\tau_0) + \tau_i + (u_i^r(\tau_0) - 1)/a$. Then the level of $r - \tau$ correlations within the homogeneous freeze-out "surface" region, which is formed by the expanding matter that initially at τ_0 occupies the region between the transversal radii $r_1(\tau_0)$ and $r_2(\tau_0) > r_1(\tau_0)$, is

$$\frac{d\tilde{r}}{d\tau} \approx \frac{r_1(\tau_1) - r_2(\tau_2)}{\tau_1 - \tau_2} \approx 1 - \frac{R}{\epsilon_0 \kappa} \quad (5.83)$$

and, therefore, the strength of $r - \tau$ correlations grows with energy: $\frac{d\tilde{r}}{d\tau} \rightarrow 1$. Note that here we account for $\tau_2 - \tau_1 \approx \kappa(\epsilon_0(r_2(\tau_0)) - \epsilon_0(r_1(\tau_0)))$ and that $\frac{d\epsilon_0(r)}{dr} \approx -\frac{\epsilon_0}{R}$ where $\epsilon_0 \equiv \epsilon_0(r = 0)$ and R is radius of nucleus. As a result the second S-term in Eq. (5.82) tends to zero at large ϵ_0 , reducing, therefore, the R_{out}/R_{side} ratio. In particular, if $\lambda_{side,V}^2 \gg \lambda_{side,S}^2$ then, accounting for a similarity of the volume emission in our approximation and in the blast wave model, where as known $\lambda_{side,V} \approx \lambda_{out,V}$, one can get: $\frac{R_{out}}{R_{side}} \approx 1 + const \cdot \frac{R}{\epsilon_0 \kappa} \rightarrow 1$ at $\epsilon_0 \rightarrow \infty$. It is worthy to note that also measure μ_S tends to zero when $\frac{d\tilde{r}}{d\tau} \rightarrow 1$ that again reduces the surface contribution to *side*- and *out*- radii at large p_T .

The presented qualitative, in fact, analysis demonstrates the main mechanisms leading to the non-trivial behavior of R_{out} to R_{side} ratio exposed in detailed HKM calculations, see Fig.1 (bottom, right).

5.10 Conclusions

The hydrokinetic approach to A+A collisions is developed. It allows one to describe the continuous particle emission from a hot and dense finite system, expanding hydrodynamically into vacuum, in the way which is consistent with Boltzmann equations and conservation laws, and accounts also for the opacity effects.

The analysis and numerical calculations show that the widely used phenomenological Landau/ Cooper-Frye prescription for calculation of pion (or other particle) spectrum is too rough if the freeze-out hypersurface is considered as common for all momenta of pions. The Cooper-Frye formula, however, could be applied in generalized form accounting for direct momentum dependence of the freeze-out hypersurface $\sigma(p)$; the latter corresponds to the maximum of emission function $S(t_\sigma(\mathbf{r}, p), \mathbf{r}, p)$ at fixed momentum \mathbf{p} in an appropriate region of \mathbf{r} .

The hydro-kinetic model is then developed for a detailed study of the matter evolution and space-time picture of hadronic emission from rapidly expanding fireballs in $A+A$ collisions. The model allows one to describe the evolution of the QGP as well as the gradually decoupling hadronic fluid - a chemically non-equilibrium matter, where the equation of state is defined at each space-time point and accounts for decays of resonances into the non-equilibrated medium.

The HKM is applied to restore the initial conditions and space-time picture of the matter evolution in central Au+Au collisions at the top RHIC energy. The analysis, which is based on a detailed reproduction of the pion and kaon momentum spectra and measured femtoscopic scales, demonstrates that basically the pictures of the matter evolution and particle emission are similar at both Glauber and CGC initial conditions (IC) with, however, the different initial maximal energy densities: it is about 20% more for the CGC initial conditions. The initial pre-thermal flow is slightly less for the CGC IC. The main factors allowing one to describe well simultaneously the spectra and femtoscopic scales are: a relatively hard EoS (crossover transition and chemically non-equilibrium composition of hadronic matter), pre-thermal transverse flows developed prior to thermalization time, an account for an “additional portion” of the transverse flows due to the shear viscosity effect and fluctuation of initial conditions, a correct description of a gradual decay of the non-equilibrium fluid at the late stage of expansion. Then one does not require the too early thermalization time, $\tau_i < 1$ fm/c, to describe the data well. All these factors are included in the present version of the HKM and it allows one to describe observables with only the two parameters.

An analysis of the emission function at the top RHIC energies demonstrates that the process of decoupling of the fireballs created in Au+Au collision lasts from about 8 to 20 fm/c, more than the half of fireball’s total lifetime. The temperatures in the regions of the maximal emission are different at the different transverse momenta of emitting pions: $T \approx 75 - 110$ MeV for $p_T = 0.2$ GeV/c and $T \approx 130 - 135$ MeV for $p_T = 1.2$ GeV/c. A comparison of the pion and kaon emissions at the same transverse mass demonstrates the similarity of the positions of emission maxima, that could point to the reason for an approximate m_T scaling.

Finally, the model is applied for the description of behavior of interferometry radii as a function of collision energy. Then the main mechanisms that lead to the

paradoxical behavior of the interferometry scales find a natural explanation. In particular, a slow decrease and apparent saturation of R_{out}/R_{side} ratio around unity at high energy happens due to a strengthening of positive correlations between space and time positions of pions emitted at the radial periphery of the system. Such an effect is a consequence of the two factors accompanying an increase of collision energy: a developing of the pre-thermal collective transverse flows and an increase of initial energy density in the fireball.

Further developments of the hydrokinetic approach and an analysis of the data in non-central A+A collisions will be the subject of a follow-up work.

Conclusions

In Chapter 2, a new class of analytic solutions for 3D relativistic expansion with anisotropic flows is found. The ellipsoidal generalization of the spherically symmetric Hubble flow is considered within this class. These solutions can also describe the relativistic expansion of the finite systems into vacuum. Specific equation of state makes the application to the whole hydrodynamic stage of evolution in heavy ion collisions to be problematic. However, the solutions can still be applicable during deconfinement phase transition and the final stage of evolution of hadron systems. Also, the solutions can serve as a test for numerical codes describing 3D asymmetric flows in the relativistic hydrodynamics.

A fast MC event generator (FASTMC) based on Landau/Cooper-Frye freeze-out prescription is presented in Chapter 3. It accounts for the decays of unstable resonances and weak decays. FASTMC allows to describe both central and non-central heavy ion collisions. The description of the k_t -dependence of the correlation radii at $\sqrt{s} = 200 \text{ AGeV}$ RHIC collisions has been achieved within $\sim 10\%$ accuracy. The comparison of the RHIC v_2 measurements with the MC generation results shows that the scenario with two separated freeze-outs is more favorable for the description of the p_t -dependence of the elliptic flow.

The new hybrid dynamical model for matter evolution in ultrarelativistic heavy ion collisions is presented in Chapter 4. It has many improvements, as compared to existing ones: flux-tube initial conditions (EPOS), event-by-event treatment, use of an efficient (3+1)D hydro code including flavor conservation, employment of a realistic equation-of-state, use of a complete hadron resonance table, and a hadronic cascade procedure after an hadronization from thermal matter at an early time.

The model is able to describe simultaneously different soft observables: transverse spectra for pions, kaons, protons, lambdas, xis; v_2 -coefficients for pions, protons and kaons; interferometry (HBT)-radii for pions.

Finally, in Chapter 5, the hydrokinetic approach to A+A collisions is developed. It allows one to describe the continuous particle emission from a hot and dense finite system, expanding hydrodynamically into vacuum, in the way which is consistent with Boltzmann equations and conservation laws, and accounts also for the opacity effects. The conditions of applicability of generalized Cooper-Frye distribution are found and proved by numerical calculations.

The hydro-kinetic model is then developed for a detailed study of the matter evolution and space-time picture of hadronic emission from rapidly expanding fireballs in $A+A$ collisions. The model allows one to describe the evolution of the QGP as well as the gradually decoupling hadronic fluid - a chemically non-equilibrium matter, where the equation of state is defined at each space-time point and accounts for decays of resonances into the non-equilibrated medium.

The HKM is applied to restore the initial conditions and space-time picture of the matter evolution in central Au+Au collisions at the top RHIC energy. The model is able to reproduce pion and kaon spectra together with pion and kaon interferometry radii. The main factors, which allows one to describe well simultaneously the spectra and femtoscopic scales are: a relatively hard EoS (crossover transition and chemically non-equilibrium composition of hadronic matter), pre-thermal transverse flows developed to thermalization time, an account for an “additional portion” of the transverse flows due to the shear viscosity effect and fluctuation of initial conditions, a correct description of a gradual decay of the non-equilibrium fluid at the late stage of expansion. Then one does not require the too early thermalization time, $\tau_i < 1$ fm/c, to describe the data well. All these factors are included in the presented version of the HKM and it allows one to describe observables with only the two parameters.

One can note the presence of the same factors (crossover EoS, pre-thermal transverse flows) in both hybrid and hydrokinetic model, being important for the simultaneous reproduction of particle spectra and femtoscopic scales. This stresses the importance and solidity of the results obtained.

An analysis of the emission function at the top RHIC energies demonstrates that the process of decoupling of the fireballs created in Au+Au collision lasts from about 8 to 20 fm/c, more than the half of fireball’s total lifetime.

A comparison of the pion and kaon emissions at the same transverse mass demonstrates the similarity of the positions of emission maxima, that could point out to the reason for an approximate m_T scaling.

Finally, the hydro-kinetic model is applied for the description of behavior of interferometry radii as a function of collision energy. Then the main mechanisms that lead to the paradoxical behavior of the interferometry scales find a natural explanation. In particular, a slow decrease and apparent saturation of R_{out}/R_{side} ratio around unity at high energy happens due to a strengthening of positive cor-

relations between space and time positions of pions emitted at the radial periphery of the system. Such an effect is a consequence of the two factors accompanying an increase of collision energy: a development of the pre-thermal collective transverse flows and an increase of initial energy density in the fireball.

Further elaboration of the hydrokinetic approach and an analysis of the data in non- central A+A collisions will be the subject of a follow-up work.

Glossary

BNL – Brookhaven National Laboratory

CERN – Conseil Européen pour la Recherche Nucléaire

SPS – Super Proton Synchrotron

RHIC – Relativistic Heavy Ion Collider

LHC – Large Hadron Collider

HBT – Hanburry-Brown-Twiss

BIBLIOGRAPHY

- [1] L.D. Landau, *Izv. Akad. Nauk SSSR* **17** (1953) 51; S.Z. Belenkij and L.D. Landau, *Usp. Fiz. Nauk* **56** (1955) 309;
- [2] E. Fermi, *Prog. Theor. Phys.* **5** (1950) 57
- [3] P. Carruthers, *Annals N.Y. Acad. Sci.* **229** (1974) 91.
- [4] E. V. Shuryak and O. V. Zhironov, *Phys.Lett.* B89 (1979) 253.
- [5] Yu.M. Sinyukov, S.V. Akkelin, N. Xu, *Phys.Rev.* **C59** (1999) 3437.
- [6] Yu.M. Sinyukov, A.N. Nazarenko, Iu.A. Karpenko, *Acta Phys.Polon.* **B40** (2009), 1109.
- [7] W. Broniowski, M. Chojnacki, W. Florkowski, A. Kisiel, *Phys.Rev.Lett.*101 (2008), 022301.
- [8] W.A. Zajc, *Two Pion Correlations in Heavy Ion Collisions*. PhD thesis, University of California, 1982 (available as LBL-14864).
- [9] Sinyukov Yu. In *Hot Hadronic Matter: Theory and Experiment*, ed. J. Rafelski. New York: Plenum, NATO ASI Series B 346:309 (1995)
- [10] M.G. Bowler, *Phys. Lett. B* 270, 69 (1991); Yu.M. Sinyukov et al., *Phys. Lett. B* 432, 249 (1998).
- [11] E. Schnedermann, J. Sollfank, U. Heinz, *Phys. Rev.* **C48** (1993), 2462 (nucl-th/93070200).
- [12] W.A. Zajc et al., *Phys. Rev. C* **29** (1984) 2173.
- [13] U. Heinz, *J. Phys. G: Nucl. Part. Phys.* **31**, S717 (2005); arXiv:nucl-th/0512051; P. Huovinen, P.V. Ruuskanen, *Annu. Rev. Nucl. Part. Sci.* **56**, 163 (2006); T. Hirano, *Nucl. Phys. A* **774**, 531 (2006).

- [14] Y. Hama, T. Kodama, O. Socolowski Jr., *Braz. J. Phys.* **35**, 24 (2005).
- [15] C. Nonaka, *J. Phys. G: Nucl. Part. Phys.* **34**, S313 (2007); T. Hirano, arXiv:0704.1699 [nucl-th].
- [16] E.V. Shuryak, *Prog. Part. Nucl. Phys.* **53**, 273 (2004); arXiv:hep-ph/0703208; arXiv:0709.2175 [hep-ph]; arXiv:0804.1373 [hep-ph].
- [17] E.V. Shuryak, *Nucl. Phys. A* **750** (2005) 64-83; arXiv:hep-ph/0405066.
- [18] W. Broniowski, W. Florkowski, M. Chojnacki, A. Kisiel, *Acta Phys. Polon.* **B40**:979-986, 2009.
- [19] I.M. Khalatnikov, *Sov. JETF*, **26** (1954) 529.
- [20] R.C. Hwa, *Phys. Rev.* **D10** (1974) 2260; F. Cooper, G. Frye, E. Schonberg, *Phys. Rev.* **D11** (1975) 192.
- [21] M.I. Gorenstein, Yu.M. Sinyukov, V.I. Zhdanov: *Phys. Lett.* **B71** (1977) 199, and *Zh. Eksp. Theor. Fiz.- ZETF (USSR)* **74** (1978), 833.
- [22] J. D. Bjorken, *Phys. Rev.* **D27** (1983) 140.
- [23] C.B. Chiu, E.C.G. Sudarshan, Kuo-Hsiang Wang, *Phys. Rev.* **D12** (1975) 902.
- [24] T. Csörgő, *Heavy Ion Phys.* **A21** (2004) 73-84.
- [25] T. S. Biro, *Phys. Lett.* **B474** (2000) 21-26, T. S. Biro, *Phys. Lett.* **B487** (2000) 133-139.
- [26] W. Broniowski, W. Florkowski, *Nucl. Phys A* **715**, 875c (2003); W. Broniowski, W. Florkowski, B. Hiller, *Phys. Rev. C* **68**, 034911 (2003).
- [27] S.V. Akkelin, P. Braun-Munzinger, Yu.M. Sinyukov. *Nucl. Phys.* **A710** (2002) 439.
- [28] W. Busza, *Acta Physica Polonica* **B35** (2004) 2873.
- [29] L.D. Landau, E.M. Lifshitz "Fluid Mechanics", Addison-Westley, Reading, Mass., 1959.
- [30] S.V. Akkelin, T. Csörgő, B. Lukács, Yu.M. Sinyukov and M. Weiner, *Phys. Lett.* **B505** (2001) 64.
- [31] Proc. of the Conference "Quark Matter 2005", *Nucl. Phys. A* **774** (2006).

-
- [32] I.P. Lokhtin and A.M. Snigirev, Phys. Lett. **B 378**, 247 (1996).
- [33] N.A. Kruglov, I.P. Lokhtin, L.I. Sarycheva and A.M. Snigirev, Z. Phys. **C 76**, 99 (1997).
- [34] I.P. Lokhtin and A.M. Snigirev, Preprint SINP MSU 2004-14/753, hep-ph/0312204.
- [35] I.P. Lokhtin and A.M. Snigirev, Eur. Phys. J. **C 45**, 211 (2006).
- [36] R. Brun and F. Rademakers, Nucl. Instrum. Meth. **A 389**, 81 (1997), (<http://root.cern.ch>).
- [37] F. Retiere and M. Lisa, Phys. Rev. **C 70**, 044907 (2004).
- [38] W. Florkowski and W. Broniowski, Acta. Phys. Pol. **35**, 2855 (2004).
- [39] S.R. de Groot, W.A. van Leeuwen, Ch.G. van Weert, Relativistic kinetic theory. Principles and Applications, North-Holland Publishing Company, Amsterdam-New York-Oxford, 1980.
- [40] Yu.M. Sinyukov, S.V. Akkelin and A.Yu. Tolstykh, Nukleonika **43**, 369 (1998).
- [41] S.V. Akkelin and Yu.M. Sinyukov, Phys. Rev. **C 70**, 064901 (2004).
- [42] S.V. Akkelin and Yu.M. Sinyukov, Phys. Rev. **C 73**, 034908 (2006).
- [43] J. Cleymans, H. Oeschler, K. Redlich and S. Wheaton, Phys. Rev. **C 73**, 034905 (2006).
- [44] F. Cooper and G. Frye, Phys. Rev. **D 10**, 186 (1974).
- [45] M.I. Gorenstein and Yu.M. Sinyukov, Phys. Lett. **B 142**, (1985) 425.
- [46] Yu.M. Sinyukov, Z. Phys. **C 43**, 401 (1989).
- [47] K.A. Bugaev, Nucl. Phys. **A 606**, 559 (1996); Cs. Anderlik *et al.*, Phys. Rev. **C 59**, 3309 (1999).
- [48] M.S. Borysova, Yu.M. Sinyukov, S.V. Akkelin, B. Erasmus and Iu.A. Karpenko, Phys. Rev. **C 73**, 024903 (2006).
- [49] J.D. Bjorken, Phys. Rev. **D 27**, 140 (1983).
- [50] R. Morita, S. Muroya, H. Nakamura and C. Nonaka, Phys. Rev. **C 61**, 034904 (2000).

-
- [51] T. Csörgö and B. Lörstad, Phys. Rev. **C 54**, 1390 (1996).
- [52] Particle Data Group, K. Hagiwara *et al.*, Phys. Rev. **D 66**, 010001 (2002).
- [53] N.S. Amelin, R. Lednicky, L.V. Malinina, T.A. Pocheptsov and Y.M. Sinyukov, Phys. Rev. **C 73**, 044909 (2006).
- [54] G. Yen, M.I. Gorenstein, W. Greiner and S.N. Yang, Phys. Rev. **C 56**, 2210 (1997).
- [55] J. Rafelski, Phys. Lett. **B 262**, 333 (1981).
- [56] F. Becattini, J. Mannien, M. Gazdzicki, Phys. Rev. **C 73**, 044905 (2006).
- [57] U.A. Wiedemann and U. Heinz, Phys. Rept. **319**, 145 (1999).
- [58] S. Wheaton and J. Clemans, arXiv:hep-ph/0407174.
- [59] P. Braun-Munzinger *et al.*, Phys. Lett. **B 344**, 43 (1995), *ibid.* **B 365**, 1 (1996), *ibid.* **B 465**, 15 (1999).
- [60] W. Florkowski and W. Broniowski, AIP Conf. Proc. **660**, 177 (2003); nucl-th/0212052 v1.
- [61] B.B. Back *et al.*, PHOBOS Collaboration, Phys. Rev. Lett. **87**, 102301 (2001).
- [62] I.G. Bearden *et al.*, BRAHMS Collaboration, Nucl. Phys. **A 698**, 667c (2002).
- [63] J. Harris *et al.*, STAR Collaboration, Nucl. Phys. **A 698**, 64c (2002).
- [64] H. Ohnishi *et al.*, PHENIX Collaboration, Nucl. Phys. **A 698**, 659c (2002).
- [65] H. Caines *et al.*, STAR Collaboration, Nucl. Phys **A 698**, 112c (2002).
- [66] J. Adams *et al.*, STAR Collaboration, Phys.Lett. **B 567**, 167 (2003).
- [67] C. Adler *et al.*, STAR Collaboration, Phys. Rev. **C 65**, 041901 (2002).
- [68] C. Adler *et al.*, STAR Collaboration, Phys. Rev. Lett. **89**, 092301 (2002).
- [69] C. Adler *et al.*, STAR Collaboration, Phys. Rev. Lett. **87**, 262302 (2001).
- [70] J. Castillo *et al.*, STAR Collaboration, nucl-ex/0210032.
- [71] B.B. Back *et al.*, PHOBOS Collaboration, Nucl.Phys. **A 757**, 28 (2005).

- [72] S.S. Adler *et al.*, PHENIX Collaboration, Phys.Rev. **C 69**, 034909 (2004).
- [73] R. Lednicky, Proc. of the Conference "Quark Matter 2005", Nucl. Phys. **A 774**, 189 (2006).
- [74] M.I. Podgoretskii, Sov. J. Nucl. Phys. **37**, 272 (1983).
- [75] S. Pratt, Phys. Rev. Lett. **53**, 1219 (1984).
- [76] T. Csörgö and S. Pratt, Proc. of the Workshop on Heavy Ion Physics, KFKI-1991-28/A, 75.
- [77] J. Adams *et al.*, STAR Collaboration, Phys. Rev. **C 71**, 044906 (2005).
- [78] M. Bystersky, STAR Collaboration, AIP Conf. Proc. **828**, 533 (2006); nucl-ex/0511053.
- [79] N.S. Amelin, R. Lednicky, T.A. Pocheptsov, I.P. Lokhtin, L.V. Malinina, A.M. Snigirev, Iu.A. Karpenko, and Yu.M. Sinyukov, Phys. Rev. **C 74**, 064901 (2006).
- [80] N. S. Amelin, R. Lednicky, I. P. Lokhtin, L. V. Malinina, A. M. Snigirev, Iu. A. Karpenko, Yu. M. Sinyukov, I. Arsene, and L. Bravina, Phys. Rev. **C 77**, 014903 (2008).
- [81] C. Adler *et al.* (STAR Collaboration), Phys. Rev. Lett. **87**, 182301 (2001).
- [82] P.F. Kolb, J. Sollfrank, and U.W. Heinz, Phys. Lett. **B459**, 667 (1999).
- [83] D. Hardtke and S.A. Voloshin, Phys. Rev. C **61**, 024905 (2000).
- [84] R.J.M. Snellings, A.M.Poskanzer, and S.A. Voloshin, nucl-ex/9904003.
- [85] M. Bleicher and H. Stoecker, Phys. Lett. **B526**, 309 (2002).
- [86] B. Zhang, C.M. Ko, B.A. Li, and Z.W. Lin, Phys. Rev. C **61**, 067901 (2000); Z.W. Lin, S. Pal, C.M. Ko, B.A. Li, and B. Zhang, Phys. Rev. C **64**, 011902 (2001).
- [87] A. Kisiel, T. Taluc, W. Broniowski, and W. Florkowski, Comput. Phys. Commun. **174**, 669 (2006).
- [88] W. Florkowski, W. Broniowski, A. Kisiel, and J. Pluta, Acta Phys. Polon. **B37**, 3381 (2006).
- [89] M. Csanad, T. Csörgö and B. Lörstad, Nucl. Phys. **A 742**, 80 (2004).

- [90] P. Huovinen, P.F. Kolb, U. Heinz, P.V. Ruuskanen, and S.A. Voloshin, Phys. Lett. **B503**, 58 (2001).
- [91] U.A. Wiedemann, Phys. Rev. C **57**, 266 (1998).
- [92] U.W. Heinz and S.M.H. Wong, Phys. Rev. C **66**, 014907 (2002).
- [93] L.V. Bravina et al., Nucl. Phys. A **698**, 383 (2002).
- [94] G. Torrieri et al., nucl-th/0404083 (2004).
- [95] J. Adams *et al.* (STAR Collaboration), Phys. Rev. Lett. **92**, 112301 (2004).
- [96] S. Voloshin and Y. Zang, Z. Phys. C **70**, 665 (1996).
- [97] A.M. Poskanzer and S.A. Voloshin, Phys. Rev. C **58**, 1671 (1998).
- [98] J. Adams *et al.* (STAR Collaboration), Phys. Rev. C **72**, 014904 (2005).
- [99] R. Lednicky, V. Lyuboshitz, K. Mikhailov, Yu. Sinyukov, A. Stavinsky and B. Erasmus, Phys. Rev. C **61** 034901 (2000).
- [100] J. Adams *et al.* (STAR Collaboration), Phys. Rev. Lett. **93**, 012301 (2004).
- [101] M. Bleicher, F. M. Liu, A. Kernen, J. Aichelin, S.A. Bass, F. Becattini, K. Redlich, and K. Werner, Phys.Rev.Lett.88, 202501, 2002.
- [102] K. Werner, Iu. Karpenko, T. Pierog, M. Bleicher, K. Mikhailov, arXiv:1004.0805.
- [103] STAR Collaboration: J. Adams, et al, Nucl. Phys. A757:102, 2005.
- [104] PHENIX Collaboration, K. Adcox, et al, Nucl. Phys. A757:184-283, 2005.
- [105] BRAHMS Collaboration, I. Arsene et al., Nucl. Phys. A757:1-27, 2005.
- [106] P. Huovinen, in Quark-Gluon Plasma 3, eds. R. C. Hwa and X. N. Wang (World Scientific, Singapore, 2004).
- [107] P. F. Kolb and U. Heinz, in Quark-Gluon Plasma 3, eds. R. C. Hwa and X. N. Wang (World Scientific, Singapore, 2004).
- [108] P. Braun-Munzinger, K. Redlich, J. Stachel, arXiv:nucl-th/0304013, in Quark Gluon Plasma 3, eds. R. C. Hwa and Xin-Nian Wang, World Scientific Publishing.
- [109] A. Andronic, P. Braun-Munzinger, J. Stachel, Phys.Lett.B673:142,2009.

-
- [110] A. Andronic, P. Braun-Munzinger, J. Stachel, arXiv:0901.2909, Acta Phys.Polon.B40:1005-1012,2009.
- [111] F. Becattini, R. Fries, arXiv:0907.1031, accepted for publication in Landolt-Boernstein Volume 1-23A
- [112] Giorgio Torrieri, Johann Rafelski, arXiv:nucl-th/0212091, Phys.Rev. C68 (2003) 034912
- [113] J. Cleymans, B. Kampfer, S. Wheaton, Phys. Rev. C65:027901, 2002
- [114] T. Hirano and K. Tsuda, Phys. Rev. C 66 (2002) 054905T.
- [115] T. Hirano, U.W.Heinz, D. Kharzeev, R. Lacey and Y. Nara, Phys. Lett. B 636 (2006) 299
- [116] T. Hirano, U. Heinz, D. Kharzeev, R. Lacey, Y. Nara, Phys.Rev.C77: 044909,2008,
- [117] D. Teaney, J. Lauret and E. V. Shuryak, Phys. Rev. Lett.86, 4783 (2001)
- [118] C. Nonaka and S. A. Bass, Nucl. Phys. A 774, 873 (2006); and Phys. Rev. C 75, 014902 (2007)
- [119] H. J. Drescher, M. Hladik, S. Ostapchenko, T. Pierog and K. Werner, Phys. Rept. 350, 93, 2001
- [120] H. J. Drescher, S. Ostapchenko, T. Pierog, and K.Werner, Phys.Rev.C65:054902, 2002, arXiv:hep-ph/0011219
- [121] (Mini)symposium on Proton-Proton Interactions, February 14 - 17 2010, Frankfurt am Main, Germany. Results to be published
- [122] T. Pierog, Klaus Werner. Phys. Rev. Lett. 101, 171101 (2008), arXiv:astro-ph/0611311
- [123] P. Romatschke, U. Romatschke, Phys. Rev. Lett. 99 172301, 2007
- [124] H. Song and U. Heinz, Phys. Lett. B 658 279, 2008
- [125] K. Dusling and D. Teaney, Phys. Rev. C 77 034905, 2008
- [126] M. Luzum and P. Romatschke, Phys. Rev. C 78 034915, 2008
- [127] D. Molnar and P. Huovinen, J. Phys. G: Nucl.Part.Phys. 35, 1041, (2008)
- [128] Huichao Song, Ulrich W. Heinz, J. Phys. G36:064033, 2009

- [129] B. Andersson, G. Gustafson, G. Ingelman, and T. Sjostrand, Phys. Rept. 97, 31, 1983
- [130] K. Werner, Phys. Rep. 232, 87, 1993
- [131] A. Capella, U. Sukhatme, C.-I. Tan, and J. {Tran Thanh Van}, Phys. Rept. 236, 225, 1994
- [132] L.D. McLerran, R. Venugopalan, Phys. Rev. D 49, 2233 (1994). *ibid.* D49, 3352 (1994); D 50, 2225 (1994)
- [133] Yu.V. Kovchegov, Phys. Rev. D 54, 5463 (1996)
- [134] E. Iancu, R. Venugopalan, Quark Gluon Plasma 3, Eds. R.C. Hwa, X.N.Wang, World Scientific, hep-ph/0303204
- [135] A. Kovner, L.D. McLerran, H. Weigert, Phys. Rev. D 52, 3809 (1995); *ibid.*, D 52, 6231 (1995).
- [136] F. Gelis, E. Iancu, J. Jalilian-Marian, R. Venugopalan, arXiv:1002.0333, submitted to the Annual Review of Nuclear and Particle Sciences
- [137] Adrian Dumitru, Francois Gelis, Larry McLerran, Raju Venugopalan, arXiv:0804.3858, Nucl.Phys.A810:91,2008
- [138] BRAHMS collaboration, I. G. Bearden, Phys Rev Lett 94, 162301 (2005)
- [139] BRAHMS collaboration, I. Arsene, Phys. Rev. C 72, 014908 (2005)
- [140] STAR Collaboration, J.Adams, et al, Phys. Rev. Lett. 98 (2007) 62301, nucl-ex/0606014
- [141] Klaus Werner, Fu-Ming Liu, Tanguy Pierog, Phys. Rev. C 74, 044902 (2006), arXiv: hep-ph/0506232
- [142] F.M. Liu, J.Aichelin, M.Bleicher, H.J. Drescher, S. Ostapchenko, T. Pierog, and K. Werner, Phys. Rev. D67, 034011, 2003
- [143] Y. Nambu, Proc. Intl. Conf. on Symmetries and Quark Models, Wayne State Univ., 1969
- [144] J. Scherk, Rev. Mod. Phys. 47, 123 (1975)
- [145] C. Rebbi, Phys. Rep. 12 (1974) 1
- [146] X. Artru and G. Mennessier, Nucl. Phys. B70, 93 (1974)

- [147] X. Artru, Phys. Rep. 97, 147 (1983)
- [148] D. A. Morris, Nucl. Phys. B288, 717, 1987
- [149] K. Werner, Phys. Rev. Lett. 98, 152301 (2007)
- [150] J. Aichelin, K. Werner, Phys.Rev.C79:064907, 2009
- [151] F. Becattini, J. Manninen, Phys.Lett.B673:19-23, 2009
- [152] T. Kodama, private communication
- [153] S. Pratt, Nucl. Phys. A830:51C-57C, 2009, arXiv:0907.1094
- [154] Y. Aoki, Z. Fodor, S.D. Katz, K.K. Szabo, JHEP 0601:089, 2006
- [155] M. Bleicher et al., J. Phys. G25 (1999) 1859
- [156] H. Petersen, J. Steinheimer, G. Burau, M. Bleicher and H. Stocker, Phys. Rev. C78 (2008) 044901
- [157] J. Takahashi et al. Phys. Rev.Lett. 103 (2009) 242301
- [158] R.P.G. Andrade, F. Grassi, Y. Hama, W.L. Qian, arXiv:0912.0703
- [159] STAR Collaboration, B. Abelev et al., Phys. Rev. C 80 (2009) 64192
- [160] J.-Y. Ollitrault, Nucl. Phys. A 638 (1998) 195c
- [161] PHOBOS Collaboration, B. Alver, et al, Phys. Rev. Lett. 98, 242302 (2007), nucl-ex/0610037
- [162] J. Aichelin, K. Werner, to be published in the proceedings of SQM 2009
- [163] K. Werner, T. Hirano, Iu. Karpenko, T. Pierog, S. Porteboeuf, M. Bleicher, S. Haussler, J. Phys. G: Nucl. Part. Phys. 36 (2009) 064030, arXiv:0907.5529
- [164] Pasi Huovinen, Nucl.Phys.A761:296-312,2005, nucl-th/0505036
- [165] R.S. Bhalerao, J.-P. Blaizot, N. Borghini, J.-Y. Ollitrault, Phys. Lett. B627:49-54, 2005
- [166] PHOBOS Collaboration, Phys.Rev. C72 (2005) 051901, and Phys.Rev.Lett. 94 (2005) 122303
- [167] STAR Collaboration, J. Adams et al, Phys. Rev. Lett. 92 (2004) 052302, nucl-ex/0306007

-
- [168] PHENIX Collaboration, S.S. Adler et al, Phys.Rev.Lett. 91 (2003) 182301, nucl-ex/0305013
- [169] PHENIX Collaboration, S. Afanasiev et al, Phys. Rev. Lett. 99 (2007) 052301, nucl-ex/0703024
- [170] A. Adil, H. J. Drescher, A. Dumitru, A. Hayashigaki and Y. Nara, Phys. Rev. C 74, 044905 (2006).
- [171] H.-J. Drescher , Adrian Dumitru, Arata Hayashigaki, Yasushi Nara, Phys.Rev.C74:044905,2006
- [172] Tables of curves kindly provided by T. Hirano
- [173] BRAHMS Collaboration, I. G. Bearden et al., Phys. Rev. Lett. 93, 102301 (2004); PhD thesis, Djamel Ouerdane, Univ. of Copenhagen, 2003; Phys. Rev. Lett. 94, 162301 (2005).
- [174] PHOBOS Collaboration, B.B.Back et al, Phys.Rev. C70 (2004) 021902, nucl-ex/0405027
- [175] G. I. Kopylov and M. I. Podgoretsky, Sov. J. Nucl. Phys. 15, 219 (1972)
- [176] G. I. Kopylov and M. I. Podgoretsky, Sov. J. Nucl. Phys. 18, 336 (1974).
- [177] M. A. Lisa, Scott Pratt , Ron Soltz, Urs Wiedemann, Ann. Rev. Nucl. Part.Sci.55:357-402, 2005, nucl-ex/0505014
- [178] A. Kisiel, W. Florkowski, W. Broniowski, Phys.Rev.C73:064902,2006, nucl-th/0602039
- [179] R. Lednicky, Physics of Particles and Nuclei 40 (2009) 307
- [180] G. F. Bertsch, M. Gong, and M. Tohyama, Phys. Rev. C 37, 1896 (1988)
- [181] S. Pratt, Phys. Rev. D 33, 1314 (1986)
- [182] S. Chapman, P. Scotto, and U. W. Heinz, Phys. Rev. Lett. 74, 4400 (1995).
- [183] M. Lisa, private communication, 26.3.2010
- [184] G. Verde et al. Phys. Rev. C65:054609, 2002
- [185] S. Y. Panitkin et al. Phys. Rev. Lett. 87:112304, 2001
- [186] D. A. Brown and P. Danielewicz. Phys. Rev. C64:014902, 2001

- [187] David A. Brown, Fu-qiang Wang, and Pawel Danielewicz. Phys. Lett. B470:33-38, 1999
- [188] D.A. Brown and P. Danielewicz. Phys. Lett. B398:252-258, 1997
- [189] P. Chung et al. Phys. Rev. Lett. 91:162301, 2003
- [190] W. Florkowski , W. Broniowski , M. Chojnacki , A. Kisiel, Acta Phys.Polon.B40:1093-1098, 2009
- [191] W. Florkowski , W. Broniowski, M. Chojnacki, A. Kisiel, Nucl.Phys.A830:821c-824c, 2009
- [192] M. Holt, "Numerical methods in fluid dynamics", Springer Series in Comput. Physics (Springer, Berlin, 1977).
- [193] R. Courant, K. Friedrichs and H. Lewy, "On the partial difference equations of mathematical physics", IBM Journal, March 1967, pp. 215-234.
- [194] V. Schneider et al., J. Comput. Phys. 105 (1993) 92.
- [195] G. Colangelo, J. Gasser, H. Leutwyler, Nucl. Phys. B603 (2001) 125
- [196] G.A. Miller, J.G. Cramer, J. Phys. G: Nucl. Part. Phys. **34**, 703 (2007).
- [197] S. Pratt, Phys. Rev. C **73**, 024901 (2006).
- [198] K.A. Bugaev, Phys. Rev. Lett. **90**, 252301 (2003).
- [199] Yu.M. Sinyukov, S.V. Akkelin, Y. Hama, Phys. Rev. Lett. **89**, 052301 (2002).
- [200] F. Grassi, Y. Hama, T. Kodama, Phys. Lett. B**355**, 9 (1995); Z. Phys. C**73**, 153 (1996).
- [201] S.A. Bass, A. Dumitru, Phys. Rev. C**61**, 064909 (2000); D. Teaney, J. Lauret, E.V. Shuryak, Phys. Rev. Lett. **86**, 4783 (2001); arXiv: nucl-th/0110037; C. Nonaka, S.A. Bass, Phys. Rev. C**75**, 014902 (2007).
- [202] S.V. Akkelin, Y. Hama, Iu.A. Karpenko, and Yu.M. Sinyukov, Phys. Rev. C**78**, 034906 (2008).
- [203] S.V. Akkelin, M.S. Borysova, Yu.M. Sinyukov, Acta Phys. Hung. A: Heavy Ion Physics **22**, 165 (2005).

- [204] J. Bondorf, S. Garpman, J. Zimanyi, Nucl. Phys. A**296**, 320 (1978); K.S. Lee, U. Heinz, E. Schnedermann, Z. Phys. C**48**, 525 (1990); F.S. Navarra, M.C. Nemes, U. Ornik, and S. Paiva, Phys. Rev. C**45**, R2552 (1992); E. Schnedermann, U. Heinz, Phys. Rev. C**47**, 1738 (1993)
- [205] Yu.M. Sinyukov, Nucl.Phys. A**566**, 589c (1994).
- [206] Yu.M. Sinyukov, S.V. Akkelin, Iu.A. Karpenko. Physics of Atomic Nuclei **71**, 1619 (2008).
- [207] Yu.M. Sinyukov, Iu.A. Karpenko, Nonlinear Phenomena in Complex Systems, **12**, 496 (2009) [arXiv:0911.4439].
- [208] D. Teaney, Phys. Rev. C **68**, 034913 (2003).
- [209] Z. Xu, L. Cheng, A. El, K. Gallmeister, C. Greiner, J. Phys. G: Nucl. Part.Phys. **36**, 064035 (2009) [arXiv:0812.3839].
- [210] Yu.M. Sinyukov, Acta Phys. Polon. B **37**, 4333 (2006); M. Gyulassy, Iu.A. Karpenko, A.V. Nazarenko, Yu.M. Sinyukov, Braz. J. Phys. **37**, 1031 (2007).
- [211] T. Lappi, L. McLerran, Nucl. Phys. A **772**, 200 (2006) [arXiv:hep-ph/0602189].
- [212] J. Vredevogd, S. Pratt, arXiv:0810.4325; S. Pratt, arXiv:0903.1469; W. Broniowski, W. Florkowski, M. Chojnacki, A. Kisiel, Phys.Rev.C **80**, 034902 (2009).
- [213] Yu.M. Sinyukov, Iu.A. Karpenko, A.V. Nazarenko, J. Phys. G: Nucl. Part. Phys. **35**, 104071 (2008).
- [214] P. F. Kolb, J. Sollfrank, and U. W. Heinz, Phys. Lett.B **459** (1999) 667; U. W. Heinz and H. Song, J. Phys. G **35** 104126 (2008).
- [215] T. Lappi, Phys. Lett. B **643**, 11 (2006) [arXiv:hep-ph/0606207].
- [216] A. Krasnitz, R. Venugopalan, Phys. Rev. Lett. **84**, 4309 (2000).
- [217] A. Krasnitz, Y. Nara, R. Venugopalan, Nucl. Phys. A**717**, 268 (2003).
- [218] A.Krasnitz *et al.*, Nucl. Phys. A**727**, 427 (2003).
- [219] A. Kovner, L. McLerran, H. Weigert, Phys. Rev. **D52**, 6231 (1995).
- [220] A. El, Z. Xu, C. Greiner, Nucl. Phys. A **806**, 287 (2008) [arXiv:0712.3734]

- [221] E. Wigner, Phys. Rev. **40**, 749 (1932).
- [222] M. Hillery, R.F. O'Connell, M.O. Scully, and E.P. Wigner, Phys. Rep. **106**, 121 (1984); H.-W. Lee, Phys. Rep. **259**, 147 (1995); W.P. Schleich, *Quantum Optics in phase space* (Wiley-VCH, 2001).
- [223] F. Becattini, J. Manninen J. Phys. G **35**, 104013 (2008); J. Manninen, F. Becattini, Phys. Rev. C **78**, 054901 (2008);
- [224] A. Andronic, P. Braun-Munzinger, J. Stachel, Acta Phys.Polon. B **40**, 1005 (2009).
- [225] M. Laine, Y. Schroder Phys. Rev. D **73**, 085009 (2006).
- [226] F. Karsch, PoS CPOD07:026, 2007.
- [227] N.S. Amelin *et al.*, Phys. Rev. C **77**, 014903 (2008).
- [228] Iu.A. Karpenko, Yu.M. Sinyukov, Phys. Lett. B in press (2010), [arXiv:0912.3457].
- [229] S. Mrowczynski, Ann.Phys. **169**, 48 (1986).
- [230] M. Prakash, M. Prakash, R. Venugopalan, and G. Welke, Phys. Rep. **227**, 321 (1993).
- [231] S.A. Bass *et al.*, Prog. Part. Nucl. Phys. **41**, 225 (1998).
- [232] R.P.G. Andrade, F. Grassi, Y. Hama, T. Kodama, and W.L. Qian, Phys.Rev.Lett.101:112301 (2008).
- [233] Yu.M. Sinyukov, S.V. Akkelin, Iu.A. Karpenko, Y. Hama, Acta Phys.Polon. B **40**, 1025 (2009).
- [234] V.A. Averchenkov, A.N. Makhlin, Yu.M. Sinyukov, Sov. J. Nucl. Phys. **46**, 905 (1987); A. N. Makhlin, Yu. M. Sinyukov, Z. Phys. C **39**, 69 (1988); Yu. M. Sinyukov, Nucl. Phys. A **498**, 151 (1989).
- [235] S.S. Adler et al, PHENIX Collaboration, Phys. Rev. Lett. **93**, 152302 (2004).
- [236] S. Afanasiev et al., PHENIX Collaboration, Phys. Rev. Lett. **103**, 142301 (2009).
- [237] S.V. Akkelin, Yu.M. Sinyukov, Phys. Lett. B **356** (1995) 525; S.V. Akkelin, Yu.M. Sinyukov, Z. Phys. C **72** (1996) 501.

- [238] U. Heinz, Nucl. Phys. A **721** (2003) 30; S. Pratt, Nucl. Phys. A **715** (2003) 389c; S. Soff, S. Bass, D. Hardtke, S. Panitkin, Nucl. Phys. A **715** (2003) 801c.
- [239] G. Bertsch, Phys. Rev. C **40** (1989) 1830; D.H. Rischke, M. Gyulassy, Nucl. Phys. A **608** (1996) 479.
- [240] Dariusz Antończyk, Acta Phys. Polon. B **40** (2009), 1137.
- [241] S. V. Afanasiev et al, NA49 Collaboration, Phys. Rev. C **66** (2002), 054902.
- [242] C. Alt et al, NA49 Collaboration, Phys. Rev. C **77** (2008), 064908.

Development of hydrodynamic and hydrokinetic approaches to ultrarelativistic nucleus-nucleus collisions

Iurii KARPENKO

Resumé :

La motivation principale pour étudier la physique des collisions d'ions lourds à des énergies ultrarelativistes est de recréer les conditions physiques semblables à celles qui existaient dans l'Univers quelques microsecondes après le Big Bang. On pense que la nouvelle forme fondamentale de la matière, le plasma de quarks et de gluons a été créé dans ces collisions. L'analyse des données expérimentales fournies du collisionneur RHIC suggère que les systèmes quasi-macroscopiques (boules de feu), créés en collisions noyau-noyau montrent un comportement hydrodynamique à un certain moment de leur évolution.

L'objectif du travail présenté dans cette thèse est de construire le modèle dynamique de collisions noyau-noyau, compatible avec les échelles d'espace-temps qui sont mesurés dans les expériences. Enfin, deux modèles sont présentés. Le premier est ce qu'on appelle un modèle hybride, qui combine l'approche hydrodynamique pour les systèmes denses de quark-gluon et d'hadrons, constitué en collisions noyau-noyau, et l'approche cinétique pour traiter le gaz raréfié d'hadrons formé à un stade tardif de collision. L'utilisation de plusieurs améliorations (équation d'état crossover, les conditions initiales de l'approche EPOS, simulation événement-par-événement) est soulignée et conduit à une bonne description de l'ensemble des données expérimentales "mous" pour les collisions noyau-noyau auprès de RHIC.

Le deuxième modèle est basé sur l'approche hydro-cinétique, qui intègre une expansion hydrodynamique de systèmes constitués en collisions noyau-noyau et de leur découplage dynamique décrite par les probabilités de libération. Le modèle est étendu pour inclure les caractéristiques réalistes de collisions d'ions lourds et appliquée pour décrire les spectres transversales pour la plupart des hadrons et des rayons HBT dans collisions noyau-noyau auprès de RHIC.

Mots clés : Collisions noyau-noyau, hadrons, hydrodynamique, interférométrie, cinétique, générateur d'événement.

Abstract :

The primary physics motivation of studying heavy ion collisions at ultrarelativistic energies is to recreate the physical conditions similar to those which existed in early universe just several microseconds after the beginning of the Big Bang. The new, fundamental form of matter, quark-gluon plasma is believed to be created in these collisions. The analysis of experimental data from RHIC collider suggests that the quasi-macroscopical systems (fireballs) created in A+A collisions show hydrodynamical behavior at certain stage of their evolution.

The goal of the work presented in this thesis is to construct the dynamical model of A+A collision, consistent with space-time scales measured in the experiments. Finally, two models are presented. The first one is so-called hybrid model, which combines hydrodynamic approach for dense quark-gluon and hadron systems, formed in A+A collisions, and kinetic approach to treat rarefied hadron gas formed at late stages of collision. The use of several improvements (crossover equation of state, initial conditions from EPOS approach, event-by-event simulation) is stressed and lead to good description of wide range of soft sector experimental data for 200A GeV RHIC Au+Au collisions.

The second model is based on hydro-kinetic approach, which incorporates a hydrodynamical expansion of the systems formed in A+A collisions and their dynamical decoupling described by escape probabilities. The model is extended to include realistic features of heavy ion collisions and applied as well to describe transverse spectra for most abundant hadrons and HBT radii in 200A GeV RHIC Au+Au collisions.

Keywords : Heavy ion collisions, hadrons, hydrodynamics, interferometry, kinetics, event generator.